

BETTII: A pathfinder for high angular resolution observations of star-forming  
regions in the far-infrared

by

Maxime J. Rizzo

Dissertation submitted to the Faculty of the Graduate School of the  
University of Maryland, College Park in partial fulfillment  
of the requirements for the degree of  
Doctor of Philosophy  
2016

Advisory Committee:

Professor Lee G. Mundy, Chair/Advisor (UMD)  
Dr. Stephen A. Rinehart, Co-Advisor (NASA GSFC)  
Professor Andrew Harris (UMD)  
Dr. Mark Wolfire (UMD)  
Dr. Alison Nordt (Lockheed Martin)  
Professor Eun-Suk Seo, Dean's representative (UMD)



*To Michelle, my parents, and my brother.*



## *Acknowledgements*

The acknowledgments and the people to thank go here, don't forget to include your project advisor...



# Contents

<b>Acknowledgements</b>	<b>iii</b>
<b>Contents</b>	<b>v</b>
<b>List of Tables</b>	<b>vii</b>
<b>List of Figures</b>	<b>ix</b>
<b>I Star formation in clustered environments</b>	<b>5</b>
I.1 Molecular Clouds . . . . .	5
I.2 Star formation . . . . .	7
I.2.1 Standard models . . . . .	7
I.2.1.1 Gravitational collapse . . . . .	7
I.2.1.2 YSO classification and characteristics . . . . .	11
I.2.2 Mass accretion in clusters . . . . .	15
I.3 Dust as a tracer of star formation . . . . .	16
I.3.1 Dust populations and properties . . . . .	17
I.3.2 Basics of dust extinction . . . . .	19
I.3.3 Radiative transfer modeling . . . . .	21
I.3.4 Observing star formation . . . . .	23
<b>II Star Formation in Clustered environments with SOFIA FORCAST</b>	<b>25</b>
II.1 Introduction . . . . .	25
II.2 Sample description and scientific goals . . . . .	27
II.3 Observations . . . . .	28
II.4 FORCAST characterization . . . . .	31
II.4.1 PSF size . . . . .	31
II.4.2 Aperture correction factor . . . . .	33
II.4.3 Instrument response and overall uncertainty . . . . .	34
II.5 Data reduction and photometry . . . . .	35
II.5.1 Pre-treatment . . . . .	36
II.5.2 Source flux extraction . . . . .	37
II.5.3 Image sensitivity . . . . .	39
II.5.4 Other photometry . . . . .	40
II.6 Data products . . . . .	42
II.6.1 Mosaics . . . . .	42
II.6.2 Photometry and SEDs . . . . .	43
II.6.3 Fitted physical parameters . . . . .	46

II.7	SED fitting . . . . .	46
II.7.1	A custom grid of models . . . . .	49
II.7.2	Fitting method . . . . .	53
II.7.3	Overview of derived parameters . . . . .	55
II.7.4	Estimating parameter uncertainty . . . . .	60
II.7.5	Discussion . . . . .	61
II.8	Application to two clusters . . . . .	63
II.8.1	IRAS 20050+2720 . . . . .	66
II.8.1.1	Context . . . . .	66
II.8.1.2	Observations and discussion . . . . .	67
II.8.2	NGC 2071 . . . . .	76
II.8.2.1	Context . . . . .	76
II.8.2.2	Observations and discussion . . . . .	78
II.9	Conclusion and future work . . . . .	80

# List of Tables

II.1	List of desired sensitivities for different distances . . . . .	29
II.3	List of targets . . . . .	30
II.5	SOFIA photometry comparison . . . . .	38
II.7	FORCAST Sensitivities . . . . .	39
II.9	Spitzer photometry comparison . . . . .	41
II.11	NGC1333 photometry . . . . .	45
II.13	SED model grid . . . . .	51
II.15	Hyperion simulation parameters . . . . .	52
II.17	Fitted parameters . . . . .	59
II.19	Source fluxes in IRAS 20050+2720's dense core . . . . .	67
II.21	Clustered sources in IRAS 20050+2720's dense core . . . . .	75
II.23	Fitted parameters in IRAS 20050+2720 . . . . .	75
II.25	Sources in NGC2071's dense core . . . . .	80
II.27	Fitted parameters in NGC2071 . . . . .	80



# List of Figures

I.1	Protostar . . . . .	10
I.2	Early evolution of YSOs . . . . .	12
I.3	Late evolution of YSOs . . . . .	13
I.4	Scenarios of clustered star formation . . . . .	17
II.1	Saturation and confusion . . . . .	26
II.2	PSF size . . . . .	32
II.3	PSF size of calibrators . . . . .	34
II.4	aperture correction . . . . .	35
II.5	Instrumental response . . . . .	36
II.6	RGB images of select sample of sources . . . . .	43
II.7	NGC1333 SEDs . . . . .	47
II.8	Ophiuchus SEDs . . . . .	48
II.9	Spectral Index distribution of point sources . . . . .	49
II.10	Fitted envelope mass and luminosity distribution . . . . .	55
II.11	Distribution of $R$ . . . . .	56
II.12	Estimated mass vs calculated mass . . . . .	57
II.13	Mass versus spectral index . . . . .	60
II.14	Inclination versus mass . . . . .	63
II.15	Luminosity versus spectral index. . . . .	64
II.16	NGC 2071 and IRAS 20050+2720 . . . . .	65
II.17	IRAS 20050+2720 core . . . . .	68
II.18	Multi-wavelength view of the IRAS 20050+2720 core . . . . .	71
II.19	IRAS20050+2720 SEDs . . . . .	73
II.20	Multi-wavelength view of the NGC 2071 core . . . . .	79
II.21	NGC2071 SEDs . . . . .	81



# Introduction

*In order to improve the mind, we ought less to learn, than to contemplate.*

R. Descartes

The work presented in this thesis is centered around the design, development, and testing of an astronomical balloon-borne telescope called BETTII: the Balloon Experimental Twin Telescope for Infrared Interferometry. Developed at NASA Goddard Space Flight Center, this instrument is exploring a relatively new observation technique called "Double-Fourier" interferometry, which could lead to future space-borne telescopes with high angular resolution in the far-infrared regime. Various fields in astronomy would benefit from such enhanced capability, as demonstrated by the success of far-infrared single-aperture telescopes such as *WISE*, *Spitzer* and *Herschel*.

More than just a pathfinder, BETTII is a scientific instrument in its own right. For its first flights, it will study regions of clustered star formation in unprecedented details, providing almost an order of magnitude better spatial resolution than any existing or past far-IR facility.

This work describes some aspects of my involvement with BETTII as well as my contributions to the scientific field of clustered star formation using another far-IR facility, the Stratospheric Observatory for Infrared Astronomy (SOFIA). The thesis is organized as follows:

- Chapter I describes the framework and current understanding of how stars are forming in clusters, and lays out the key tools that we use to study these regions.
- Chapter II is a study of nearby star-forming clusters using new data that we obtained with the SOFIA observatory. SOFIA offers moderately high angular resolution, which we use to improve the study of the brightest, densest regions of star formation. This work is to be submitted for publication shortly after the conclusion of this dissertation.
- Chapter ?? describes the physical principles of interferometry which drive the design of the balloon instrument. We predict the sensitivity of the BETTII instrument and identify scientific targets and calibrators that are suitable for our first flights.
- Chapter ?? is a standalone, refereed paper that was published in 2015 on the spectral sensitivity of double-Fourier interferometers in general. It proposes a mathematical framework to analyze the sensitivity of such instruments to various types of noise sources. We apply those findings to the case of BETTII.
- Chapter ?? discusses the design of the control system for BETTII, which presents unique challenges compared to any other balloon-borne instrument. We also discuss the controls algorithm that is used in flight to properly estimate the orientation of the payload, a key requirement to achieve successful interferometry.
- Chapter ?? shows results of the implementation of the control system on BETTII. This consists of laboratory and on-sky testing of BETTII at GSFC.
- Chapter ?? summarizes our findings and discusses the path forward for the BETTII project.

BETTII will be shipping out to Fort Sumner, New Mexico, for its first balloon flight in early August. The flight window is from mid to late September. The technical work in chapters III to VI plays a key role in the success of this first flight.



# Chapter I

## Star formation in clustered environments

This chapter is an introduction to some of the concepts which play a role in the formation of stars. First, we discuss properties of the molecular clouds which are the sites of star formation. Second, we elaborate on the physics of the star-forming processes and their various stages. Third, we discuss the properties of the dust, which is the main observable which is relevant for the rest of this thesis. This chapter is not meant to be an exhaustive review of the field, but instead introduces the relevant scales, contexts, and metrics associated with the star formation phenomenon, which are important to understand when designing an observatory to study it.

### I.1 Molecular Clouds

Molecular clouds are the dense regions of the interstellar medium (ISM) where stars are forming. They contain about half the mass of the ISM in  $< 2\%$  of its volume (see Kennicutt et al., 2012, and references therein). High densities ( $n \gtrsim 1000 \text{ cm}^{-3}$ ) of mostly molecular hydrogen and low temperatures ( $< 20 \text{ K}$ ) distinguish molecular clouds from the other major

components of the ISM in galaxies: the Hot Ionized Medium, the Warm Neutral Medium, the Warm Ionized Medium, and the other cold phase of the ISM, the Cold Neutral Medium, which is thought to be the parent region in which molecular clouds are formed. In addition to molecular hydrogen, molecular clouds also contain Helium (cosmic abundance of 10% by number), dust ( $\sim 1\%$  by mass), CO ( $\sim 1 \times 10^{-4}$  by number), and traces of many other molecules.

Observations reveal that molecular clouds are highly structured with often a filamentary structure on a range of spatial scales (**Heyer:2015ee**; **Andre:2010ka**; **Andre:2014et**; Williams et al., 2000). We are particularly interested in the star formation process in these regions so our focus is on the youngest systems,  $\lesssim 2$  Myr, where stars are often still embedded and may not have accreted the majority of their final mass.

Approximately 60% of all stars are thought to form in embedded, young stellar clusters with 100 or more stars (Porras et al., 2003; Allen et al., 2007). These  $>100$  star clusters have characteristic sizes of 2-4 parsecs (pc) with peak surface densities of  $>10$  stars per square parsec and a typical median distance between nearest neighbor young stellar objects (YSOs)  $<0.06$  pc (Gutermuth et al., 2009).

Because star-forming clusters are surrounded by interstellar matter from the parent molecular cloud, they usually cannot be studied at optical wavelengths, due to the large obscuration from dust grains along the line of sight. Infrared observations can be used to probe these structures since the dust can acquire sufficient temperature to emit thermally from the mid-infrared through millimeter wavelengths.

The high density of YSOs within clusters, combined with their typical separations of few hundredths of parsecs requires a high angular resolution in order to capture the relevant spatial scales to identify individual sources and probe their physical characteristics.

## I.2 Star formation

### I.2.1 Standard models

A considerable amount of literature exists on star formation and the various physical processes involved in forming stars (**Evans:1999gz; PortegiesZwart:2010kc; Hennebelle:2012dk**; e.g. McKee et al., 2007; Kennicutt et al., 2012, and references therein). In this section, we review some of the most standard views that describe how stars are born and grow to acquire their final masses.

#### I.2.1.1 Gravitational collapse

The simplest way to derive characteristic quantities related to the formation of stars is to consider a pre-stellar core as a spherical clump of uniform, isothermal gas in hydrostatic equilibrium. For such a system, the Virial theorem applies, which describes the balance between the gravitational potential and the kinetic thermal energy within the gas. In other words, in hydrostatic equilibrium, the core's self-gravity is compensated by the internal pressure caused by the temperature of the gas. If the temperature then decreases, or if the core mass increases, the core will contract and become unstable. While simplistic, this treatment leads to a handy derivation of critical timescales, sizes, and masses that form a good starting point for more elaborate theories.

First, it is important to determine what are the characteristic timescales of star formation. In the core with a uniform density, the simplest timescale to define is called the free-fall time  $t_{\text{ff}}$ : this is the time it takes for the total gravitational collapse of a spherically-symmetric clump of uniform density  $\rho$  if only the force of gravity is considered:

$$t_{\text{ff}} \sim \left( \frac{3\pi}{32G\rho} \right)^{1/2} \sim 1 \times 10^6 \text{ yr} \left( \frac{n}{1000 \text{ cm}^{-3}} \right)^{-1/2} = 1 \times 10^6 \text{ yr} \left( \frac{\rho}{4 \times 10^{-21} \text{ g cm}^{-3}} \right)^{-1/2}, \quad (\text{I.1})$$

where we have substituted a typical value for the particle density in clusters  $n \equiv n_{H_2} \approx 1000 \text{ cm}^{-3}$ , and converted it as well into a mass density, using a mean molecular weight  $\mu = 2.33$  (corresponding to a Helium abundance of 10% in number as in McKee et al. (2007)). The free-fall time is usually a lower limit on the collapse timescale, since there can always be some physical mechanisms such as thermal and turbulent pressure or magnetic fields that will resist gravity and slow down the infall of gas into the potential well.

The other relevant quantity that involves time is the sound speed in the cloud,  $c_s = (kT/(\mu m_H))^{1/2}$ , where  $\mu \approx 2.33$  is the mean molecular weight of the gas and  $m_H$  the mass of hydrogen. For a given spatial scale  $R$ , the sound-crossing time is defined as  $t_s = R/c_s = 4.9 \times 10^5 \text{ yr} \left( \frac{R}{0.1 \text{ pc}} \right) \left( \frac{c_s}{0.2 \text{ km s}^{-1}} \right)^{-1}$ . This is the time it takes for a wave to cross the scale  $R$  while traveling at the sound speed. Intuitively, if the core has a size  $R$  such that  $t_{\text{ff}} < t_s$ , it tends to collapse faster than the gas in the cloud can react. This corresponds to a characteristic sizescale that is called the Jeans' length, and corresponds to the characteristic sizescale of gravitational instability within a cloud (McKee et al., 2007):

$$\lambda_J = c_s \times t_{\text{ff}} = 0.2 \text{ pc} \left( \frac{c_s}{0.2 \text{ km s}^{-1}} \right) \left( \frac{n}{1000 \text{ cm}^{-3}} \right)^{-1/2}. \quad (\text{I.2})$$

The Jeans mass is the amount of mass within a sphere of diameter  $\lambda_J$ , and corresponds intuitively to the minimum mass a core needs to gather in order to trigger a

gravitational collapse:

$$M_J = \frac{4\pi}{3}\rho \left(\frac{\lambda_J}{2}\right)^3, \quad (I.3)$$

$$= 0.3 M_{\odot} \left(\frac{c_s}{0.2 \text{ km s}^{-1}}\right)^3 \left(\frac{n}{1000 \text{ cm}^{-3}}\right)^{-1/2}. \quad (I.4)$$

Note that this formalism completely ignores the material that surrounds the core while it collapses. In practice, the cloud exerts an external pressure on the core that needs to be taken into account when calculating the critical masses. This case of a clump of self-gravitating gas that is immersed in a medium of external pressure  $P_{\text{ext}}$  is called a Bonnor-Ebert sphere. It can be shown (McKee et al., 2007) that the sizescale for a critical Bonnor-Ebert sphere is similar to the Jeans' length, and the mass scale is:

$$M_{\text{BE}} = 1.18 \frac{c_s}{G^{3/2} \rho^{1/2}}, \quad (I.5)$$

$$= 4.4 M_{\odot} \left(\frac{c_s}{0.2 \text{ km s}^{-1}}\right)^3 \left(\frac{n}{1000 \text{ cm}^{-3}}\right)^{-1/2}, \quad (I.6)$$

$$\sim 14 M_J. \quad (I.7)$$

The turbulent nature of the core can lead to local overdensities which can reach the Jean's or Bonnor-Ebert masses. The core can then fragment into multiple centers of collapse, each of which will lead to a star. Accretion from the turbulent surrounding core material happens throughout this phase. A simple, symmetric accretion model features an infalling envelope with density profile which follow power laws from  $r_{\text{env}}^{-1.5}$  to  $r_{\text{env}}^{-2}$ , an important observable that can be useful to test these theories. Some models of slowly-rotating infalling clouds suggest more complex density profiles for the envelopes (e.g. Ulrich, 1976; Terebey et al., 1984) than simple power laws, but are observationally difficult to

constrain due to the small differences with traditional power-law envelopes and the small scales at which those differences occur (a few 100's of astronomical units (au)).

Through conservation of angular momentum, some infalling material flattens into a circumstellar disk, while bipolar outflows carve out a cavity in the envelope along the axis of rotation of the star.

The object now has three characteristic components: the star itself; the flattened disk; and a diffuse envelope with an open cavity, which constitutes a mass reservoir for future accretion onto the star. A cartoon of the protostar is shown in Fig. I.1.

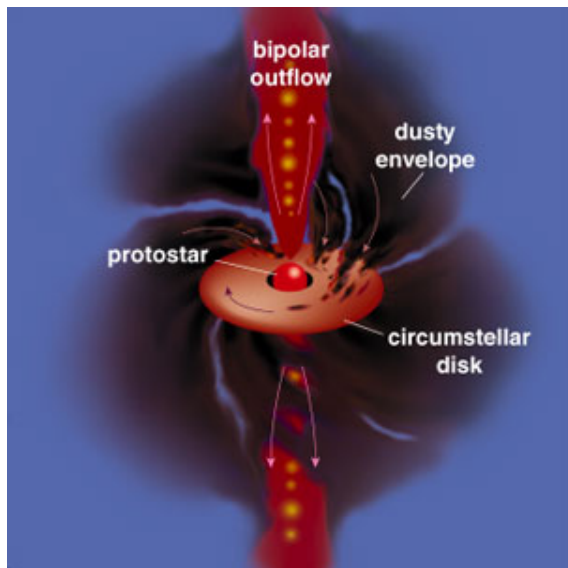


FIGURE I.1: Cartoon of a protostar ([Greene:2001dg](#)) with the envelope, a flattened circumstellar disk, the bipolar outflow/cavity, and the protostar at the center. A typical scale for the envelope of a young object is  $\sim 10\,000$  au.

Although most of the mass is contained in the H<sub>2</sub> gas, there is a small fraction of material in the form of dust grains of various sizes and populations. Despite their low mass, these grains play a very important role in determining the observable properties of YSOs, because of their tendency to absorb short wavelengths and radiate in the thermal infrared (see Section I.3).

### I.2.1.2 YSO classification and characteristics

YSOs are composed of a star, a disk, and an envelope. The star is believed to be fairly well understood as a young object in hydrostatic equilibrium on its way to the main sequence. Depending on many parameters, the spatial distribution of gas in the disk and the envelope can be predicted by simple models, but in all likelihood is very complex, inhomogeneous, and asymmetric. For clarity, we will discuss here the simple models that can be used to describe the YSOs in the multiple stages of their evolution.

In the most common model of the evolution of young stars, there are four stages in the lifetime of a YSO. The first stage consists of a dense core right after the YSO is born. The disk is almost nonexistent, the envelope still is dense and circularly symmetric. This is called Class 0. As the system evolves, the outflow increases the opening angle of the cavity, the density of the envelope decreases, and the size of the disk increases.

The various classes of YSO (from 0 to III) have distinct observational signatures, although can be dependent on the viewing angle. The most commonly used tool to classify YSOs based on their SEDs is to use the spectral index, which corresponds to the mid-IR slope  $\alpha$  in the log-log plots, with  $\alpha = d(\log \lambda F_\lambda)/d \log \lambda$  between 2 to 20  $\mu\text{m}$  (McKee et al., 2007). The four classes of YSOs are:

- Class 0: Most of short-wavelength ( $< 10 \mu\text{m}$ ) light is highly obscured by the dust in the massive envelope. Most of the emission is around  $100 \mu\text{m}$  and into the sub-millimeter/radio regimes. If there is a disk, it is very small. Some authors (Dunham et al., 2010) classify a source as Class 0 as long as the amount of the mass in the envelope is at least half the total mass.
- Class I: Light scatters at short wavelength off the dust grains to give us a hint at the

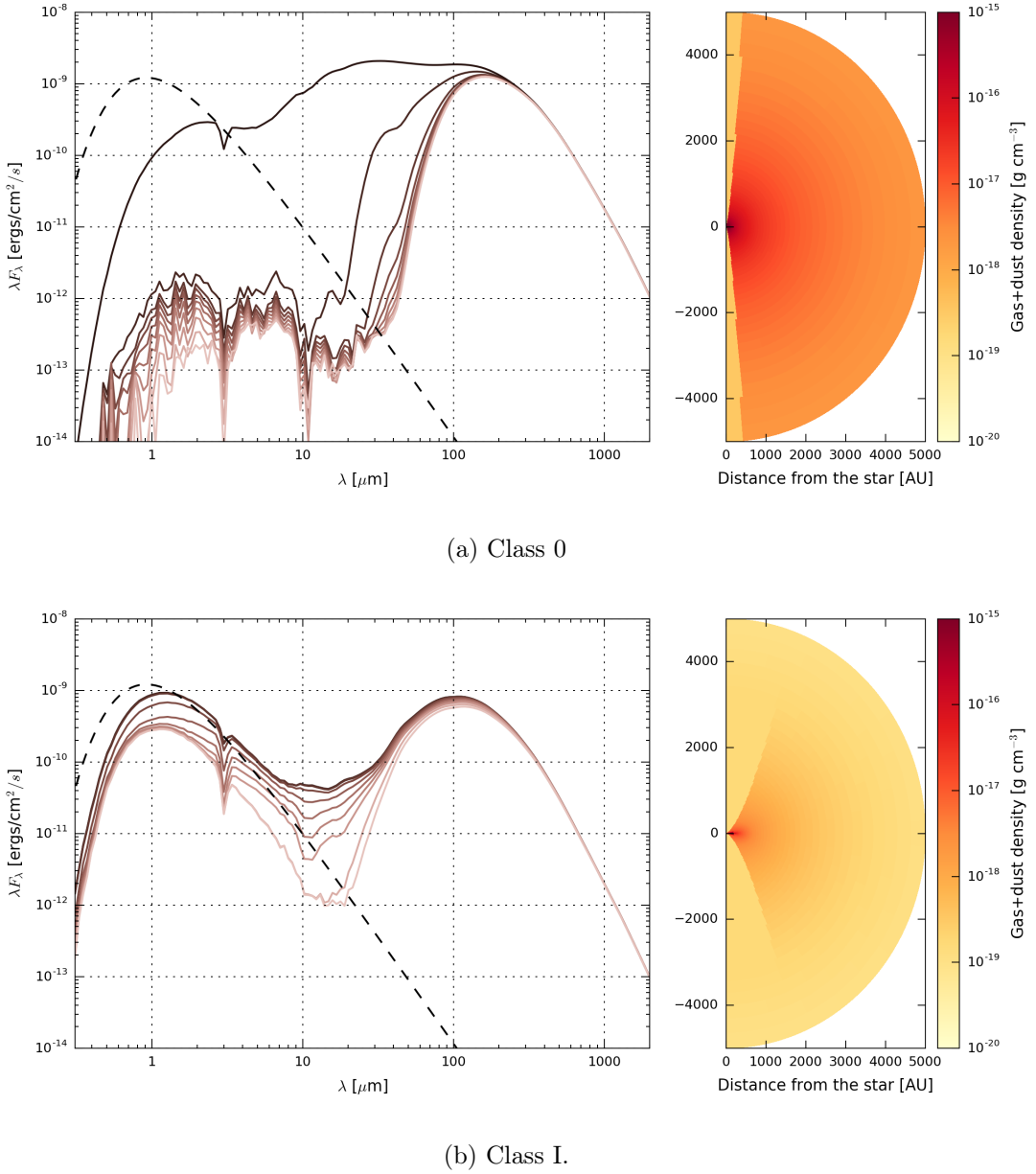


FIGURE I.2: Early evolution of YSOs. The left panel shows the spectral energy distribution (SED) of the object. Lines of different colors show different inclination angles. The dashed line corresponds to the SED of the central object only. The right panel shows a cross-section of the mass density (including both gas and dust) profile used in the modeling. Darker colors indicate higher densities. In this model, the cavity is in the up/down direction, coaligned with the circumstellar disk axis. The circumstellar disk is present in those models, although difficult to distinguish in the density maps because of its small scale.

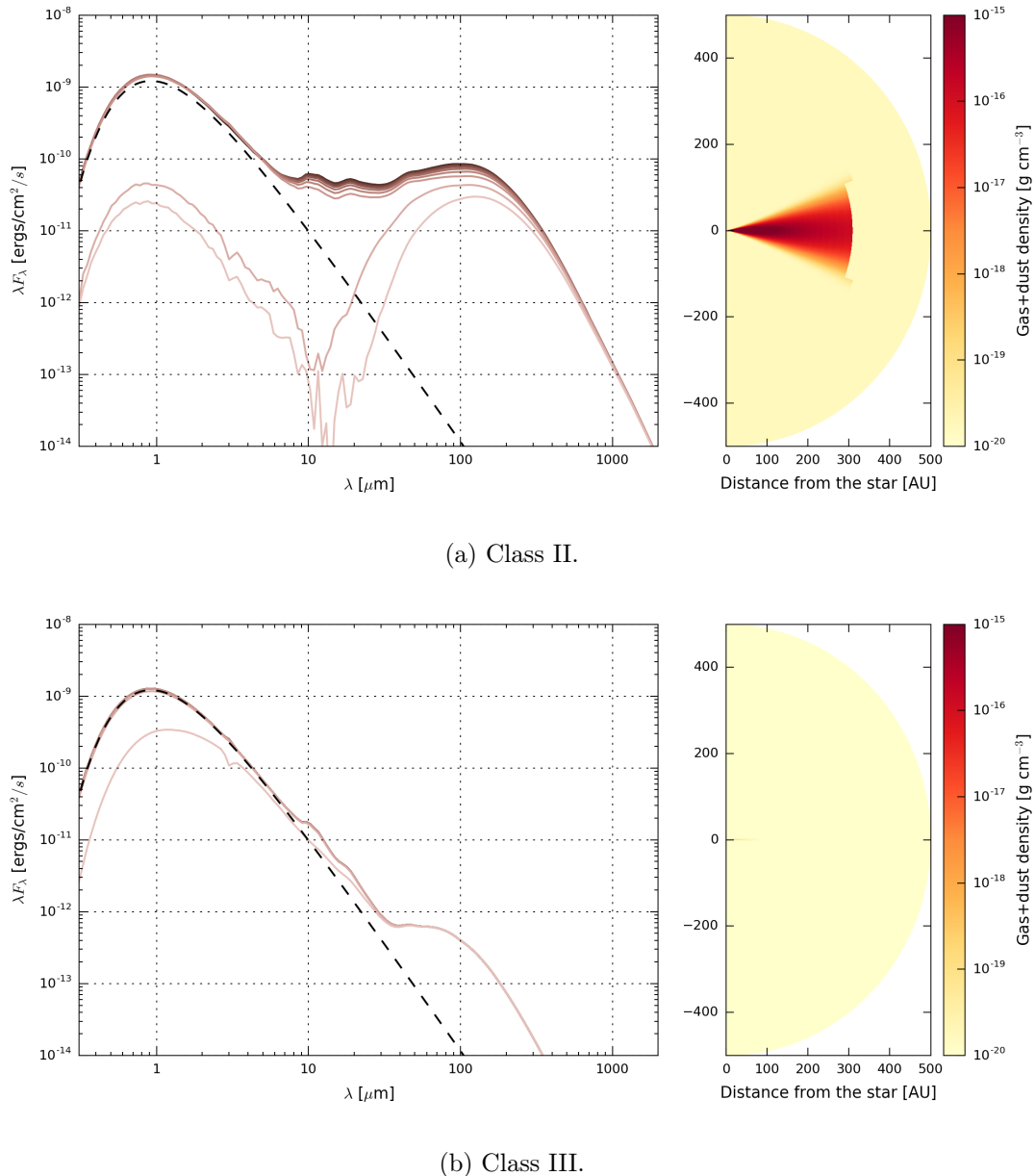


FIGURE I.3: Late evolution of YSOs.

embedded object, but it still very obscured. The envelope's mass is lower, and the disk extends to larger distances. The typical spectral index  $\alpha$  is positive.

- Class II: The YSO is now a pre-main sequence star, with a spectral index  $-1.5 < \alpha < 0$  and a significant circumstellar disk. This is traditionally referred to as a classical T-Tauri star.
- Class III: Still a pre-main sequence star, but most of the accretion has stopped, and  $\alpha < -1.5$ . The envelope has almost completely disappeared, and so has most or all of the disk, as traced by infrared excess emission.

An illustration of canonical spectral energy distributions (SED) and density structure is shown in Figs. I.2 and I.3 for the four main stages, with parameters taken in Whitney et al. (2003b). On the left of each picture, the SED is the measurable quantity when the YSO is unresolved at all wavelengths. The challenge is to estimate the density structure (to the right) by measuring the SED. The different lines plotted in the SEDs are different inclination angles, highlighting the enormous impact of the viewing angle on the potential interpretation of these SEDs. The dashed line corresponds to the Planck function from the central source. These models were run using the Hyperion software (Robitaille, 2011) with "OH5" dust (Ossenkopf et al., 1994), as discussed in more details in Section I.3.

These SEDs are often characterized and classified with standard observational metrics, such as the bolometric luminosity (Myers et al., 1993; Dunham et al., 2010):

$$L_{\text{bol}} = 4\pi d^2 \int_0^\infty S_\nu d\nu, \quad (\text{I.8})$$

$$(\text{I.9})$$

where  $S_\nu$  is the flux density in  $\text{W m}^{-2} \text{Hz}^{-1}$ . We will use this simple diagnostic later in our analysis of our SOFIA FORCAST data.

### I.2.2 Mass accretion in clusters

The discussion in the previous section represents a simplified view of how a single core collapses and forms a star. While it is convenient to assume that the original core forms a fixed reservoir of gas that will determine the star's final mass, it is likely too simplistic, since YSOs are preferentially forming inside of clusters close to multiple other YSOs and sharing a dense, often turbulent environment (Porras et al., 2003; Allen et al., 2007; Gutermuth et al., 2009).

The answer to how stars acquire their final mass is a key issue in star formation. Does dense gas fragment into isolated centers of collapse? Do young stars competitively accrete material from a surrounding common reservoir? Do gravitational interactions between forming young objects play a significant role in setting the final stellar mass function? Better observational understanding of these clusters is necessary to address these questions and to discriminate between the different models, as noted by Bonnell et al. (2006), Offner et al. (2011) and Myers (2011).

Given the typical stellar separations in clusters with fully formed YSOs and the typical densities of gas in these cores, several 1000s of au ( $1 \text{ pc} = 206\,265 \text{ au}$ ) is the size scale over which forming stars must draw material to become  $0.5\text{-}10 M_\odot$ . Once the material is inside a few 100s of au, it is strongly bound to the forming stellar system (which may be one or more stars) and its fate is determined. To give an idea of the possibilities for accreting material, Fig. I.4 sketches three scenarios for how stars could capture mass in the cluster environment: (a) core collapse, (b) competitive accretion, and (c) collisional merging. In

core collapse (CC) (Fig. I.4a, McKee et al., 2003; Myers, 2011), the cluster's gas fragments into cores which collapse individually to form single, binary, or small multiple star systems; the available mass is defined by the original fragment. In competitive accretion (CA) (Fig. I.4b, Bonnell et al., 1997), the initial core collapses but contains a small fraction of the star's final mass; additional mass is captured competitively with other forming stars from the surrounding dense core gas. In collisional merging (CM) (Fig. I.4c, Bonnell et al., 2002), the initial fragments interact gravitationally and form larger mass cores before and during the formation process.

Are all these processes observed at once in star forming clusters? What conditions favor one versus the other, and why? Are these processes observed at different stages in the cluster's history?

Recent studies by Offner et al. (2011) and Myers (2011) compared protostar luminosity distributions with predictions of models based on these ideas. Offner et al. (2011) suggest that both CC and CA could work if the star formation rate in the cluster increases with time; (Myers, 2011) finds that a CA-type model with additional Bondi accretion to produce massive stars works best. As highlighted at the end of the Offner et al. (2011) paper, larger cluster samples and better data on massive stars are needed to improve the observational constraints on models.

### I.3 Dust as a tracer of star formation

Despite being a small component by mass, interstellar dust is an important tracer of star formation activity and its absorption and emission of radiation is an important factor in the evolution and outcome of the star formation process. Dust grains are heated up by

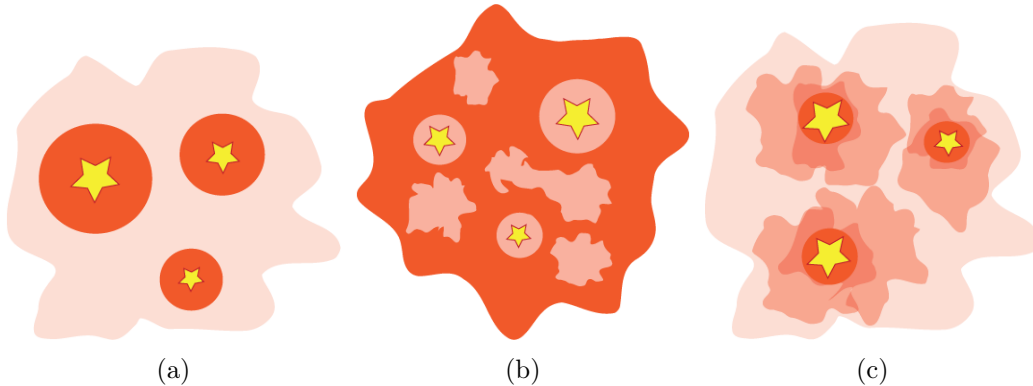


FIGURE I.4: Three scenarios of clustered star formation: (a) core collapse, (b) competitive accretion, and (c) collisional merging. Darker colors indicate higher densities.

absorbing the short wavelength emission from stars and re-radiate in the thermal infrared, accounting for  $\sim 30\%$  of the total luminosity of the galaxy (Mathis, 1990).

Observationally, dust plays perhaps the most important role when it comes to studying star formation. It usually is assumed that dust is well mixed with the gas, which makes it an excellent tracer of the gravitational well and mass distribution in YSOs. Because H<sub>2</sub> and He molecules have very few spectral signatures at temperatures below 100 K, they are difficult to observe and study directly. Dust grains block UV and visible star light and emit continuum far-IR radiation, opening a large region of the electromagnetic spectrum for astronomers to study the properties of star formation. Alternative tools to study star formation are dedicated to observing spectral lines of the molecular species of the ISM such as CO and other dense gas tracers, which reveal information about the dynamics of the gas in these regions.

### I.3.1 Dust populations and properties

One of the best early studies of the composition of dust grains in the ISM was done by Mathis et al. (1977), where they studied the absorption spectrum of the diffuse ISM, and

found that the measurements were appropriately fitted with a dust grain composition of silicates and small graphite particles (Stecher et al., 1965). They were able to fit the observed extinction curve with grain-size distribution, typically  $n(a) \propto a^{-3.5}$ , where  $a$  is the grain size (assuming spherical grains) and  $n(a)$  corresponds to the number of grains of size  $a$ . This distributions requires low and high cutoffs for the grain sizes, typically 50 Å and 0.25 μm, respectively (Weingartner et al., 2001).

This grain size distribution model was later on enhanced by Cardelli et al. (1989) to account for the difference in interstellar extinctions (hence grain size distributions) across different galactic lines of sight. These authors were able to successfully parameterize the size distribution using a single parameter,  $R_V$ , which is the ratio of the total extinction  $A(V)$  to selective extinction<sup>1</sup> (or color)  $E(B - V) = A(B) - A(V)$ . Smooth distributions of sizes of graphite and silicate grains vary between the low density regions of the ISM, where  $R_V = 3.1$ , and the high density regions, where  $R_V = 5.3$  (Kim et al., 1994).

Observations in the thermal infrared from space telescopes have detected strong absorption lines at 9.7 μm and 18 μm which are attributed to stretching mode of Si-O and bending mode of O-Si-O, confirming the presence of silicates in dust compositions (Weingartner et al., 2001). Other emission features at 3.3, 6.2, 7.7, 8.6, and 11.3 μm (Sellgren, 1994) were attributed to bending and stretching modes of polycyclic aromatic hydrocarbons (PAH, see Gillett et al., 1973; Allamandola et al., 1985), which are complex, planar organic molecules.

A consolidated model matching all-sky measurements by COBE, IRAS and *Planck* confirms the composition of amorphous silicates and carbonaceous grains with sizes ranging from large grains ( $\approx 1 \mu\text{m}$ ) down to tens of atoms (**Collaboration:2016kp**), where the

---

<sup>1</sup>Extinction and colors are expressed in magnitudes

larger carbonaceous grains have graphitic properties and the smaller population have PAH-like properties.

Knowing the dust composition and size distribution of grains is important to properly predict its observational behavior and relate it to the physical quantities of interest, since the goal of the exercise is to use dust as a tracer of star-forming mechanisms. A given dust model needs to provide several key quantities that can be used in radiative transfer modeling (see Section I.3.3), such as the albedo, the scattering function, and the opacity.

In the very cold regions surrounding a YSO, where the dust temperature typically never exceeds a few tens of K, it is expected that these dust grains are covered by a mantel of ices which can dramatically change their radiative properties, especially at short wavelengths (e.g Ossenkopf et al., 1994).

### I.3.2 Basics of dust extinction

Dust grains are responsible for the extinction within molecular clouds, inside of clusters, and also within each YSO; although these various extinctions could originate in different grain populations. The typical representation of this extinction uses the ratio of observed over expected flux, measured in V-band:  $A_V \equiv A(V) = 2.5 \log(F_\nu^{\text{obs}}/F_\nu)$ . The extinction,  $A(\lambda)$ , is a function of wavelength and is expressed in magnitudes. An alternative representation is to consider the extinction as being caused by an optical depth  $\tau_{\text{ext}}$  such that  $\exp(-\tau_{\text{ext}}) \equiv F_\nu^{\text{obs}}/F_\nu$ . The two definitions have the equivalence  $A(\lambda) = 1.086\tau_{\text{ext}}(\lambda)$ .

At sufficiently long wavelength, dust opacity models can usually be represented by a simple power-law,  $\kappa_\nu = \kappa_0(\nu/\nu_0)^\beta$ , with the index  $\beta$  depending on the specifics of the dust model (**Draine:2011tr**). The opacity  $\kappa_\nu$  is expressed in  $\text{cm}^2 \text{g}^{-1}$ , and can be interpreted as a extinction cross-section per unit mass. Most dust models assume a 1:100 dust-to-gas

ratio, and derive opacities per unit gas+dust mass, instead of just dust mass. From a radiative transfer perspective, the observed specific intensity from a thermal source  $B_\nu(T)$  at temperature  $T$  in the optically thin regime is  $I_\nu = \int B_\nu(T) d\tau_\nu$ , where the optical depth is  $\tau_\nu = \int \kappa_\nu \rho_{\text{dust}} dl$ . In this expression all quantities depend on the location  $l$  along the line of sight. If  $T$ ,  $\kappa_n u$ , and  $\rho_{\text{dust}}$  are constant along the line of sight, this simplifies to:

$$I_\nu = \tau_\nu B_\nu(T) = \kappa_n u \rho_{\text{dust}} L B_\nu(T) = \kappa_n u \sigma_{\text{dust}} B_\nu(T), \quad (\text{I.10})$$

where we define  $\sigma_{\text{dust}}$  as the mass surface density.

A measure of the intensity from a source can thus lead to an approximation of the total mass within a primary beam, for a given dust grain model. For a source with a measured sub-millimeter flux density  $S_\nu$ , in the optically thin regime we can write  $S_\nu = \kappa_\nu \sigma_{\text{dust}} B_\nu(T) \Omega$ , where  $\Omega$  is the solid angle of the source. We obtain a measure of the mass by writing  $M \approx \sigma_{\text{dust}} \Omega$ , to obtain (e.g Shirley et al., 2000):

$$M = \frac{S_\nu d^2}{B_\nu(T_{\text{dust}}) \kappa_\nu}, \quad (\text{I.11})$$

with a dust temperature is usually taken to be between 10 to 20 K for general regions of molecular clouds.

With only near- to mid-IR wavelengths observations (2-60  $\mu\text{m}$ ), however, it is more difficult to estimate the dust mass, because the system is usually not in the optically thin regime and cool dust at these temperatures emits weakly or not at all at these wavelengths. To use these observations, which are interesting because they naturally are at higher resolution than single-dish submillimeter data, detailed radiative transfer models are usually required (see Section I.3.3).

Dust grains can either scatter or absorb photons, and both of these processes have their own frequency-dependent efficiency. Large grains are usually considered in local thermal equilibrium (LTE). However, small grains ( $< 50 \text{ \AA}$ ) can be subject to stochastic heating, where single photons can heat up the grains to much higher temperatures for very short amounts of time, which can cause the apparent temperature of the dust to be higher. In all cases the emission is expected to, and assumed, to be isotropic.

Scattering mechanisms can be much more complicated to represent, as they usually involve a scattering phase function, describing the deflection angle of incident photons (which also depends on wavelength). Most models show that dust grains are preferentially forward-scattering (**Draine:2011tr**). The scattering properties of the dust model strongly influence the short-wavelength flux, while the absorption properties influence all wavelengths.

### I.3.3 Radiative transfer modeling

Several radiative transfer codes exist in the literature, and we have explored a few of them (DIRT, by **Wolfire:1986fw** HOCHUNK by Whitney et al. (2003a) and HOCHUNK3d by Whitney et al. (2013)). We opted for an open-source package called Hyperion (Robitaille, 2011), which has the advantage of having a Python interface and enjoys a relatively large community support. The code can accept different dust models and can generate various types of geometries and density grids. It contains the essential geometrical elements of a YSO: stars, disks, envelopes with cavities, which all have numerous parameters to describe their density structures. It can also accept user-generated, arbitrary density grids.

The radiative transfer code uses a Monte-Carlo technique to propagate packets through the density grid. This is an iterative process, as the dust both absorbs and

re-emits radiation. The code implements multiple different techniques and proxies to improve the computation speed and the accuracy of the simulation, as explained in great details in Robitaille (2011). Beyond the traditional benchmarks used in that paper, we validate our wrapper to the Hyperion code by reproducing SED behaviours from other authors (see Fig. I.2 an I.3 for examples of simulations using this code, which match the ones in Whitney et al. (2003b)).

The SEDs from models usually present a large amount of degeneracies, especially when the entire range of wavelengths is not covered, as often is the case for most observed sources. The reason for the ambiguity is a combination of limitations of astronomical instrumentation and limitations on our knowledge of the physics in these regions. On the instrumentation side, observations are always associated with measurement errors and limitations. Systematic calibration uncertainties are typically 5-20% at all wavelengths, and different wavelengths usually probe different spatial scales which can complicate matching to the model. On the physics side, averaged dust grain properties are most often used, as the detailed physical distribution of grain sizes, types, and physical state is not known. In addition, geometrical effects such as viewing angles can dramatically change the SED shape, as it is illustrated in Fig. I.2 an I.3.

Others (e.g., Robitaille et al., 2006) have used similar codes to produce standardized grids of pre-computed models which randomly sample a very large number of source geometry parameters. These grids of models are routinely used by the community to fit a set of unresolved SED measurements at discrete wavelengths. However, most often the scatter in the parameters for the few best fit models prevents from drawing meaningful conclusions on the observations. In Chapter II, we discuss this problem and offer an alternative method to determine the best-fitting models.

One of the key challenges of using this code is to determine which dust models to use. For this work, we choose to use exclusively OH5 dust (Ossenkopf et al., 1994), which represents grains with an ice mantle which are the result of a coagulation phase of an initial distribution of grain sizes following  $n \propto a^{-3/2}$ . This model was found to accurately represent some grain distribution in the ISM (see e.g. Dunham et al., 2010).

### I.3.4 Observing star formation

In the past decade, space-based infrared observatories such as *Spitzer* and *Herschel* have really allowed the beginning of the detailed study of dust around forming stars, by sampling the SEDs in key spectral regions, such as the PAH region (with the IRAC instrument on *Spitzer*), the mid-infrared (with the MIPS instrument, especially its 24 μm channel), and the far-IR (with the PACS and SPIRE instruments on *Herschel*). These single-aperture observatories have been excellent at changing our understanding of star formation on its largest scale.

However, these observatories lack the required angular resolution to observe the key physics of star formation in dense clusters in the key wavelength region between 30 μm and 200 μm. For a diffraction-limited single aperture telescope, the angular resolution and spatial resolutions  $R_\theta$  and  $R_{\text{linear}}$  are:

$$R_\theta = 17.6'' \left( \frac{\lambda}{70 \mu\text{m}} \right) \left( \frac{D}{1 \text{m}} \right)^{-1}, \quad (\text{I.12})$$

$$R_{\text{linear}} = 0.04 \text{ pc} \left( \frac{d}{500 \text{ pc}} \right) \left( \frac{\lambda}{70 \mu\text{m}} \right) \left( \frac{D}{1 \text{m}} \right)^{-1}, \quad (\text{I.13})$$

which shows that even *Herschel* with its 3.5 m primary mirror and its 70 μm channel can barely resolve clustered YSOs (typical separations of a few hundredths of pc) for the closest

---

star-forming clusters, let alone study their structure in detail.

To further complicate the problem, most space observatories are tailored for very sensitive observations, so the brightest regions of clusters often cause saturation issues due to a lack of dynamic range to observe both the diffuse emission and the very clustered YSOs. These two issues have continually prevented scientists from gathering a good picture of the physics in these dense and important regions of stellar birth.

In the following chapter, we use SOFIA FORCAST to overcome both the lack of resolution of existing facilities, and the saturation effects from most observations towards the densest regions of star-forming regions. This is a first step towards a better understanding of these regions. This chapter is aimed at becoming a standalone publication in an astronomical journal, to be submitted shortly after the end of this thesis work.

## Chapter II

# Star Formation in Clustered environments with SOFIA FORCAST

### II.1 Introduction

Most stars in the Galaxy form in cluster environments of sizes 2-4 pc, often containing more than 100 young stellar objects (YSOs), with typical separations of  $<0.05$  pc between stars near their centers (Porras et al., 2003; Allen et al., 2007; Gutermuth et al., 2009). Previous studies have been effective in elucidating the young stellar content and distribution in clouds on large scales (parsec down to 0.05 pc) (Kennicutt et al., 2012), but young cluster cores, born in dense portions of molecular clouds, are more difficult to observe. They are obscured at optical through near-IR wavelengths. At mid-IR through far-IR wavelengths, the material surrounding YSOs and involved in the stellar birth process emits due to heating by the young stars, but the resolution to date has not been sufficient to isolate individual stars in the cores of most nearby young clusters.

*Spitzer* has tremendously helped our understanding of star formation, by providing sensitive observations in continuum bands from 3.6  $\mu\text{m}$  to 160  $\mu\text{m}$ . In particular, the MIPS 24  $\mu\text{m}$  channel provided a robust way to determine the spectral index of YSOs, hence leading to dramatic improvement of understanding of the YSO population in clusters (e.g., Gutermuth et al., 2009; Gutermuth et al., 2011).

However, the most dense regions of clusters presented a challenge for the MIPS instrument, as the YSOs are too bright and/or in too close proximity, which led to saturation and confusion, as exhibited in Fig. II.1. In this figure, we show the same region seen by the IRAC 3.6  $\mu\text{m}$  band, the MIPS 24  $\mu\text{m}$  band, and the *Herschel* PACS 70  $\mu\text{m}$ , from left to right. While the IRAC instrument can clearly distinguish multiple objects within the region, the MIPS image is completely saturated, while the PACS image is confused and cannot properly resolve the individual objects due to the lower resolution of the telescope. Note that these objects are much closer from each other than it is typical to see in clusters (0.01 pc instead of a typical value of 0.04 pc), however this scale of projected separation is not unusual at the centers of clusters.

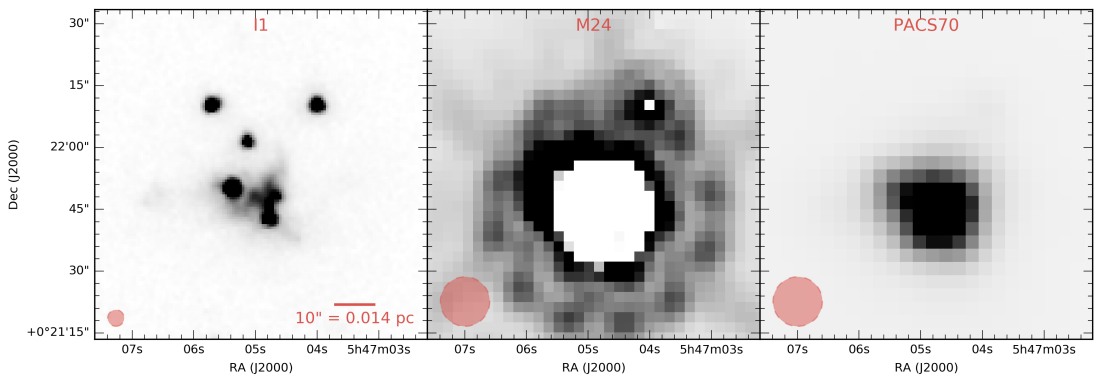


FIGURE II.1: Saturation and confusion in NGC2071.

Future instruments like BETTII will be able to tackle the confusion problem at wavelengths from 30 to 100  $\mu\text{m}$ , and be complementary to *Herschel* observations of star-forming

regions. In the meantime SOFIA, the Stratospheric Observatory For Infrared Astronomy, can already start studying these dense regions, providing 2-3.5'' resolution between 10 and 37  $\mu\text{m}$ , without the saturation problems present in more sensitive observatories. This corresponds to a factor of 2-3 improvement in angular resolution over *Spitzer* at 24  $\mu\text{m}$ .

## II.2 Sample description and scientific goals

This chapter reports the results of a survey of nearby star-forming cluster cores with the SOFIA FORCAST instrument (Herter et al., 2012). The clusters were selected from a list of dense young clusters within 1 kpc of the Sun derived from works by Porras et al. (2003) and Gutermuth et al. (2009). From their lists we selected clusters that were: (1) north of -25° declination so that they could be observed from a northern hemisphere SOFIA flight; (2) included membership of >50 YSOs; and (3) included bright 8-24  $\mu\text{m}$  sources within the dense cores based on *Spitzer* and/or WISE data.

We proposed to observe in four FORCAST science continuum bands: 11.1, 19.7, 31.5 and 37.1  $\mu\text{m}$ , which cover the wavelength range available for the instrument at the time of proposal (2012). This wavelength coverage is complementary to archival data from *Spitzer* and *Herschel*. Our focus on bright regions spread all across the sky is convenient for SOFIA, as our project could be observed as a gap-filler between the primary science flight legs of other projects.

The main objective of the survey is to gather statistics on the YSO content of the *Spitzer* saturated regions, and fill the SED gap between *Spitzer*'s bands and *Herschel*'s bands, when the latter are available. While most of our targets have valid *Spitzer* IRAC data, often the data from the MIPS instrument is unavailable due to saturation or confusion. *Herschel* photometry usually is not published in the literature for our sources, but

maps of our regions are sometimes available so we can still retrieve the far-infrared fluxes. For the targets without MIPS or *Herschel* data, these SOFIA observations are the best information available between the longest IRAC band at 8  $\mu\text{m}$  and the shortest submillimeter bands from ground-based telescopes. Thus our data provide important constraints the SED of very clustered YSOs in these regions to infer their physical properties.

The data analysis and scientific interpretation are presented in the next few sections. First, we describe our observations, as well as the archival datasets that we use to complement them. Second, we properly characterize the systematics of the FORCAST instrument and their variations over multiple science flights spanning multiple years. The data reduction process is then explained, followed by a snapshot of the data products themselves. We finally discuss our SED fitting strategy, and fit the SEDs of three of our clusters to derive the physical properties of their embedded YSOs.

### II.3 Observations

The FORCAST camera (Herter et al., 2012) has two separate  $256 \times 256$  pixel infrared arrays that can image multiple bands in the wavelength range from 5.5-37  $\mu\text{m}$  with  $0.768'' \times 0.768''$  pixels. The two arrays can observe simultaneously through a dichroic beam splitter that divides the wavelength range shortward and longward of 26  $\mu\text{m}$ . Alternatively, the long wavelength array can be used by itself with the dichroic removed from the light path, gaining a sensitivity factor of  $\sim 2.5$ . We observe the 11.1 and 37.1  $\mu\text{m}$  together (hereafter "mode 1") and the 19.7 and 31.5  $\mu\text{m}$  together (hereafter "mode 2"). We set the  $1\sigma$  sensitivity threshold to that of a moderately rising SED for a  $1.5 L_\odot$  source, which is scaled appropriately for the distance to the cluster (see Table II.1). This is an attempt at probing the same luminosities at all distances and obtain a consistent sample of YSOs.

TABLE II.1: List of desired sensitivities for different distances

Distance (pc)	1 $\sigma$ minimum detectable flux (Jy)				Corresponding minimum $L_\odot$
	11 $\mu\text{m}$	19 $\mu\text{m}$	31 $\mu\text{m}$	37 $\mu\text{m}$	
200.0	0.1	0.1	0.32	0.7	~0.5
400.0	0.1	0.1	0.32	0.6	~1.5
600.0	0.05	0.04	0.18	0.25	~1.5
800.0	0.02	0.02	0.1	0.12	~1.5
1,000.00	0.01	0.01	0.06	0.1	~1.5

However, for the most nearby clusters, the corresponding observing time was so short that the overhead from the observatory was very costly. Hence, we put a lower threshold to the integration time of 30 s. Similarly, the sensitivity of the 37  $\mu\text{m}$  band is such that in order to be consistent with our sensitivity target, this band was heavily driving the observing time using mode 1. Hence, we observe in this mode as long as is required to meet the sensitivity target for the 11  $\mu\text{m}$  band, and request more observations in the 37  $\mu\text{m}$  band on its own (hereafter "mode 3"). This allowed us to request less total observing time while keeping our sensitivity self-consistent. A summary of our target sensitivities for various distances is shown in Table II.1.

Various observing techniques are available to the FORCAST user to deal with background subtraction. The most robust techniques are very costly in terms of overhead for the observatory, so we decided to request the cheapest observing mode: the Chop-Nod mode (C2N), combined with 9 ditherings for each field, which dramatically helps when co-adding images together. Most of our data was processed by the SOFIA automated pipeline that provided calibrated Level 2 images, except for the data from the first few flights, for which we received the help of FORCAST's Principal Investigator, Dr. Joe Adams, who processed the raw data through his own instrument pipeline.

The data were acquired over 10 SOFIA flights spanning multiple years, with the last

batch dating from February 2015. The actual observing times for each band and cluster is shown in Table II.3. In that table, we have estimated the time for the 37  $\mu\text{m}$  band using a composite formula that levels the observing time from mode 3 to that of mode 1, considering their respective sensitivities. We obtained about 10 h of on-sky data, and 10 out of our 12 original target clusters were observed.

TABLE II.3: List of targets

Cluster	Coordinates (J2000)	SOFIA Flight IDs	$N_{\text{Fields}}$	$d$ (pc)	$T_{11}$ (s)	$T_{19}$ (s)	$T_{31}$ (s)	$T_{37}$ (s)
Cepheus A	22h56m10s +62d03m26s	F132 F109	2	730	206	234	235	490
Cepheus C	23h05m45s +62d30m05s	F132	1	730	150	121	121	286
IRAS20050	20h07m05s +27d28m51s	F166 F131	2	700	321	224	256	266
NGC1333	03h29m00s +31d17m20s	F129 F193 F190	9	240	530	558	467	446
NGC2071	05h47m06s +00d21m45s	F192	2	420	36	25	33	42
NGC2264	06h41m07s +09d33m35s	F156	4	913	495	300	331	587
NGC7129	21h43m07s +66d06m42s	F109	1	1000	383	214	214	709
Ophiuchus	16h27m05s -24d30m29s	F157	11	150	396	468	501	365
S140	22h19m23s +63d18m44s	F129	1	900	322	393	393	568
S171	00h04m01s +68d34m50s	F132	1	850	253	219	219	476

**Notes:** For each cluster, we list the SOFIA flights on which the data was taken, the number of individual fields within the cluster, the distance, and the total integration time for each of the 4 observation bands, including all fields. The 37  $\mu\text{m}$  time quoted is a composite time calculated by combining the exposure time of mode 1 with that of mode 3, as discussed in the text.

To complement our observations, we obtained publicly available WISE, *Spitzer*, and *Herschel* images. Most of our targets have already available *Spitzer* IRAC and/or MIPS photometry (mostly from Gutermuth et al., 2009; Megeath et al., 2012; Evans et al., 2009), which we use in the relevant cases. In the cases where no IRAC photometry was available, we applied our own photometry algorithms. We could not find published photometry for the targets with available *Herschel* images, hence we also used our own photometry pipeline to derive fluxes from archival images. In some cases, we find previously published

submillimeter continuum measurements to help constrain the long-wavelength behavior of the SEDs.

## II.4 FORCAST characterization

In addition to the science images, a number of calibrators were observed during each flight for different dichroic settings and wavelength bands. These calibrators are usually bright stars which are point sources for SOFIA’s angular resolution, and have known mid-IR fluxes, so they can be used both for flux and PSF calibration. We use them for two purposes: the first is to obtain a robust metric to determine whether sources are extended or not; the second is to determine the aperture correction factor which will be used for aperture photometry of science sources.

### II.4.1 PSF size

The size of the PSF can be defined in multiple ways. We adopt the approach of characterizing the PSF using its encircled energy distribution. Fig II.2 shows the average of the normalized encircled energy distribution of the PSF, measured on all the calibrators of our sample which use each filter settings. Each curve represents one of the five different combinations of bandpass filter and dichroic setting that we use for our observations. For each radius, the total energy is the sum of the pixels within the circular aperture of that radius, to which we subtract an estimate of the background in an annulus around the source (see Section II.5.2 for details on the background subtraction methods).

As expected, the PSF at 37.1  $\mu\text{m}$  is larger than the PSFs at shorter wavelengths, but by less than the traditional diffraction limit rule. This indicates that additional PSF

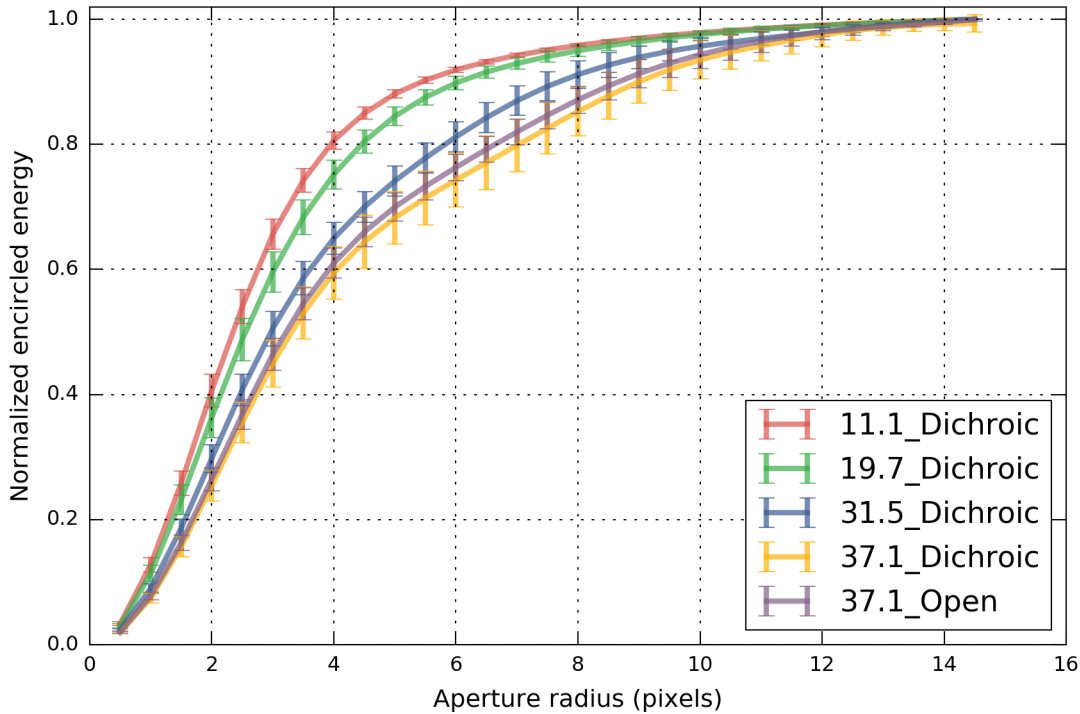


FIGURE II.2: Average PSF encircled energy distribution profile for all calibrator observations.

smearing is occurring at short wavelengths, likely due to telescope jitter and pointing errors, which is consistent with what other authors have found (e.g. Herter et al., 2013). Throughout all the flights, point source calibrators have the same encircled energy distribution shape within  $\sim 4\%$  rms.

To look at the behavior of the PSF in more detail, we can use the full width at half maximum of the encircled energy distribution, FWHM, as a proxy for PSF size. The variation of this quantity for the various flights, bandpass/dichroic setting, and calibrators used is showed in Fig. II.3. This shows the flight-to-flight differences and, for some calibrators, the in-flight variability. We find that the latter is usually small, except for the SOFIA flight on 05-02-2014, for which the spread is quite considerable and could have been caused by instrumental malfunction or abnormal levels of water vapor in the atmosphere.

The variation from flight to flight is larger than the variation within a given flight, which indicates variability in the observing conditions, systematics, or thermal radiation environment of the observatory between different flights. Even considering the flight-to-flight and calibrator-to-calibrator variations, the overall spread in FWHM for a given observation setting is almost always less than 10%, making this metric a useful reference to compare with scientific data. In our analysis we will compute FWHM for our sources and compare it to the FWHM from the current flight for the same filter setting, if the calibration file exists. If no calibration observation exists for a given setting, we use the mean FWHM for that setting from calibrators observations in other flights. The ratio  $\beta_{37} = \text{FWHM}_{\text{source}}/\text{FWHM}_{\text{cal}}$  helps quantify the extension of the source, to within  $\sim 10\%$  confidence level.

### II.4.2 Aperture correction factor

In Fig. II.2, we observe that the encircled energy does not vary much by an aperture radius of 12 pixels, so we consider this fiducial aperture as our "total flux" aperture. The goal of aperture photometry is to estimate the amount of flux in this large aperture, which we consider to be the total amount of flux from the source, by only measuring flux within a much smaller aperture. This has the advantage of reducing contamination from other sources, and increases the signal-to-noise ratio of the flux estimate since the pixels near the tail of the PSF usually contain more noise than signal. In Fig II.4, we plot the aperture correction factor that we compute from the ratio of the flux measured within an aperture of 3 pixels radius and this 12-pixel aperture. Not surprisingly, this graph follows very closely the plot of FWHM from Fig II.3, showing the close link between the aperture correction factor and the shape of the calibrator's PSF. We match each observation in our data to the mean of the aperture correction factors for the same observation setting and flight.

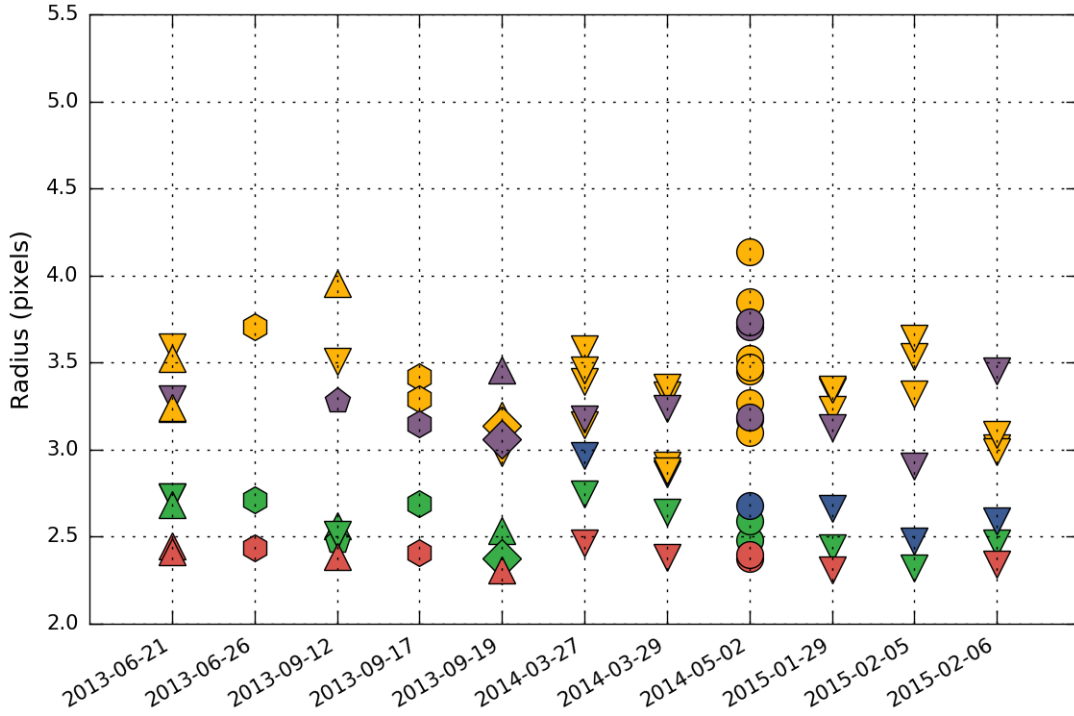


FIGURE II.3: Distribution of the radius at half maximum of the encircled energy (corresponding to half of FWHM) for all calibrators observations within each bandpass. Lower wavelengths have lower FWHM. In red: 11  $\mu\text{m}$  band, with dichroic; in green: 19  $\mu\text{m}$  band, with dichroic; in blue: 31  $\mu\text{m}$  band, with dichroic; in yellow: 37  $\mu\text{m}$  band, with dichroic; in purple: 37  $\mu\text{m}$  band, no dichroic. Down triangles:  $\alpha$  Boo; Pentagons:  $\alpha$  Cet; Diamonds:  $\alpha$  Tau; Up triangles:  $\beta$  And; Hexagons:  $\beta$  Peg; Circles:  $\beta$  UMi.

### II.4.3 Instrument response and overall uncertainty

To validate our approach, we take a look at the calibrator fluxes after normalization by the calibration factor, which is provided directly by the FORCAST pipeline. This calibration factors converts the pixel digital value a physical flux density unit, and presumably is determined using the flux from calibrator stars as well. Here we re-measure the flux from each calibrator for each observation setting and each flight, using our standard aperture photometry method and background subtraction. Ideally, we would always obtain the same flux for each setting and calibrator, independently of the flight, an assertion we find

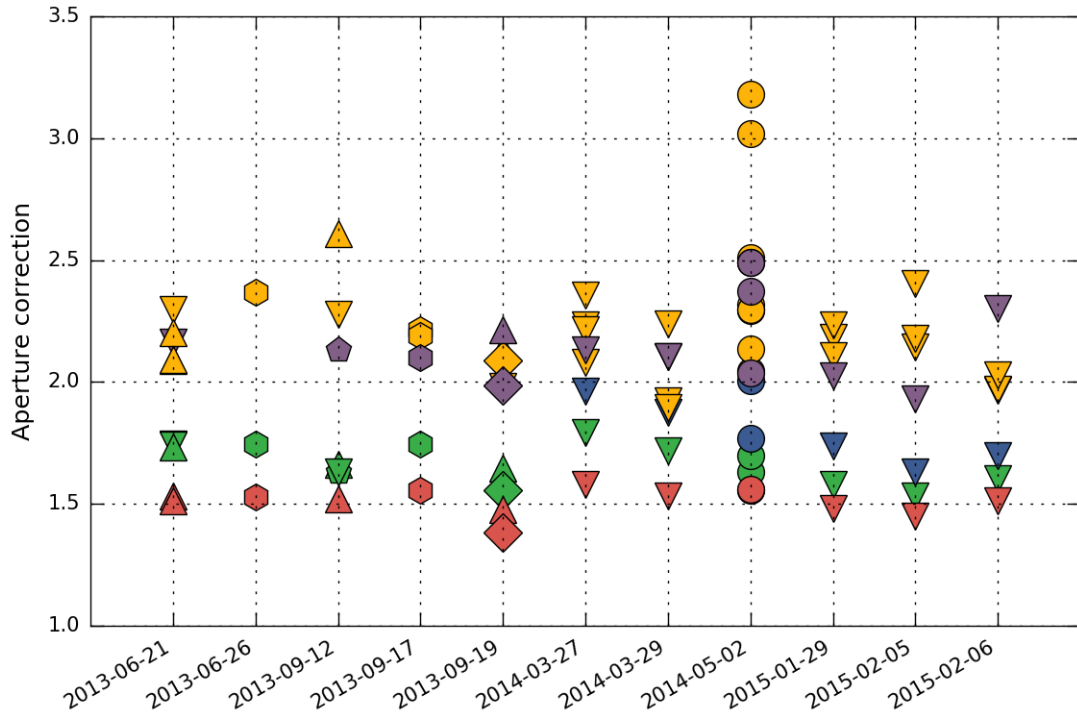


FIGURE II.4: Instrumental response and aperture correction. The color code and marker shape is the same as in Fig. II.3. Lower wavelengths usually have smaller aperture correction.

true to within  $\sim 5\%$  r.m.s (Fig II.5). The in-flight errors are typically lower than this. This validates our aperture photometry method, and we can trust that the instrument's systematics are well-behaved to within these levels.

This would suggest that we can adopt systematic  $1\sigma$  uncertainties of  $\sim 5\%$ , a value which is consistent with the published uncertainties of  $3\sigma \approx 20\%$  (De Buizer et al., 2012).

## II.5 Data reduction and photometry

The data were processed through various versions of the online pipeline to yield Level 2 data products available on the archive (Herter et al., 2013). We apply our own reduction procedure and photometry pipeline on those products to derive final images, source

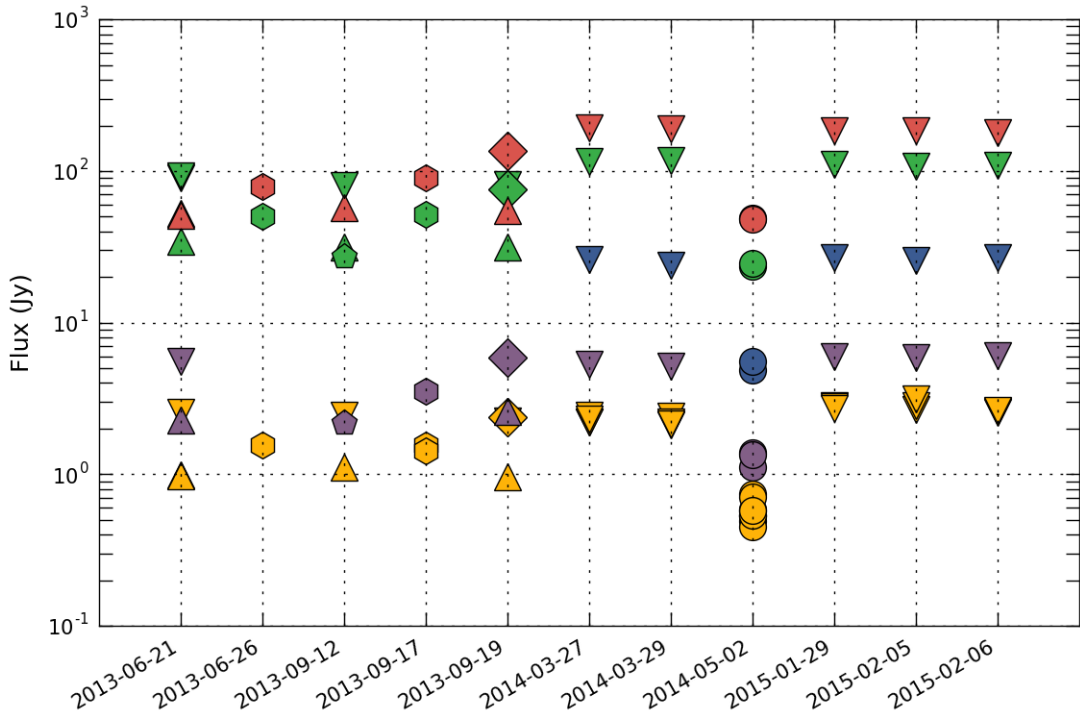


FIGURE II.5: Instrumental response, showing decreased calibrator fluxes with longer wavelengths, which is expected since all calibration targets are evolved stars. The color code and marker shape is the same as in Fig. II.3. In this plot, the variation across multiple flights for a given marker type of a given color is usually less than  $\sim 5\%$ . Note that for the bottom green triangles ( $\alpha$  Boo at  $19 \mu\text{m}$ ), there seems to be a systematic change between flights occurring before and after 2013-09-19.

positions, fluxes and sensitivities. Our software makes extensive use of the Python *astropy* package (Astropy Collaboration et al., 2013) and its associated modules *photutils* and *APLpy*.

### II.5.1 Pre-treatment

Some manual treatment of each image is necessary before it could be analyzed by our software. We followed this procedure: a) visually align the WCS coordinate system, often  $10\text{-}20''$  off, using point sources and archival data from other wavelengths and facilities such as IRAC  $8 \mu\text{m}$ ; b) cropping the images to clean off the nodded fields, and c) identify the

coordinates of each source, both point-like and extended.

After these manual steps, the Level 2 images are multiplied by the calibration factor provided by the online pipeline, which converts them to Jy/pixel. We do not proceed to any systematic color correction, but the effects on the fluxes are very small (Herter et al., 2013).

### II.5.2 Source flux extraction

We feed the adjusted files to our photometry pipeline. For each identified source, we determine its flux in all bands using aperture photometry with local background subtraction. The aperture correction factor we use is the one determined from the calibrators observed for the same observation setting during the same flight as the one when the data was taken. If a calibrator is not available during the flight, we use the average aperture correction factor taken over 9 of our 10 flights (we choose to exclude the flight on 05/02/2014 which seems to have abnormal behavior).

We distinguish between 3 types of sources after manual identification: *isolated*, which are point sources with no nearby objects; *clustered*, which are point sources with nearby objects; and *extended*, which are not consistent with being point sources.

For point sources that are isolated, we use our standard aperture of 3 pixels at all wavelengths. We consider an annulus surrounding the source extending from 12 to 20 pixels radius (24 to 40 for clustered sources): the local background is determined from the mode of the pixels in the annulus, while the sensitivity is calculated by measuring the standard deviation of the flux values within 3-pixel apertures spread over that annulus (Shimizu et al., 2016). We apply the aperture correction derived from the calibrator observations taken during that flight.

For extended sources, an elliptical aperture is determined manually from the 37  $\mu\text{m}$  images. The local background is determined from the mode of an elliptical annulus, with an inner boundary at the elliptical aperture and an outer boundary corresponding to an ellipse 20% larger. The sensitivity quoted is the point source sensitivity, and is determined following the same method as for point sources, using the standard deviation of apertures spread across the elliptical annulus.

The photometry from sources that were observed in different flights is then combined to increase the signal-to-noise ratio. This combination takes into account the sensitivity of each source by appropriately weighing each image.

The source sensitivity calculated is added in quadrature to the systematic uncertainty of the instrument, for which we follow the recommendation from (Herter et al., 2012) to adopt a 7%,  $1\sigma$  uncertainty.

TABLE II.5: SOFIA photometry comparison

SOFIA name	F11 Jy	F11L Jy	F19 Jy	F31 Jy	F31L Jy	F37 Jy	F37L Jy
S140.3	10.28	9.70	101.49	419.41	401.00	525.90	669.00
S140.4	3.80	4.00	88.95	337.22	368.00	352.07	485.00
S140.5	110.57	110.00	830.97	2065.13	1585.00	2278.61	2176.00
Sum of sources in cluster	124.65	123.70	1021.40	2821.76	2354.00	3156.58	3330.00
Total cluster emission	135.20	145.00	1194.57	4449.46	3780.00	5840.64	6730.00
Ratio	1.08	1.17	1.17	1.58	1.61	1.85	2.02

Comparison of SOFIA four-band photometry from Harvey et al. (2012) on S140 (columns with 'L'). All fluxes are in Janskies. The authors' "total emission" actually represents the total emission in the entire field of view, whereas our measurement corresponds to a manually-selected source region encompassing only the dense core. The total emission in the entire field of view is less representative, as it could include contribution from other sources as well as areas of negative flux from the chopping and nodding steps. In this cluster, there is a large amount of emission which is not clearly associated to the three identified sources.

To validate our flux extraction method, we compare our results with data from

Harvey et al. (2012) who observed one of the sources in our sample, S140. Their photometry (shown in their Table 1) of IRS 1, 2 and 3 (respectively corresponding to our targets S140.5, S140.4, and S140.3) is compared to our photometry in Table II.5. We find good agreement between our fluxes and theirs, although some differences are larger for longer wavelengths. We attribute this to differences in the exact centroid location of the sources, which could be due to a different aperture size. Centroid errors have more impact at longer wavelengths, where the flux is larger.

### II.5.3 Image sensitivity

TABLE II.7: FORCAST Sensitivities

Cluster	F11			F19			F31			F37			Sources
	$\sigma^{\text{man}}$	$\sigma^{\text{std}}$	$\sigma^{\text{th}}$										
CepA	0.07	0.04	0.05	0.11	0.05	0.05	0.19	0.07	0.16	0.26	0.09	0.34	4
CepC	0.03	0.03	0.04	0.10	0.05	0.04	0.19	0.06	0.16	0.16	0.09	0.30	4
IRAS20050	0.04	0.03	0.04	0.08	0.04	0.05	0.13	0.05	0.16	0.30	0.11	0.32	7
NGC1333	0.12	0.04	0.07	0.07	0.07	0.07	0.22	0.08	0.25	0.48	0.13	0.52	11
NGC2071	0.19	0.10	0.12	0.32	0.15	0.15	0.21	0.22	0.49	0.45	0.28	0.81	6
NGC2264	0.07	0.03	0.05	0.19	0.05	0.06	0.28	0.07	0.20	0.21	0.09	0.43	21
NGC7129	0.07	0.03	0.03	0.10	0.04	0.03	0.26	0.09	0.12	0.17	0.08	0.19	5
Ophiuchus	0.11	0.05	0.08	0.16	0.07	0.08	0.31	0.09	0.27	0.41	0.18	0.65	19
S140	0.04	0.03	0.03	0.16	0.03	0.03	0.21	0.07	0.09	0.35	0.11	0.21	7
S171	0.04	0.03	0.03	0.07	0.04	0.03	0.07	0.05	0.12	0.16	0.06	0.23	2

**Notes:** For each band F11, F19, F31 and F37, we measure the  $1\sigma$  sensitivity  $\sigma^{\text{man}}$  and  $\sigma^{\text{std}}$  in each field from the data using two different methods (see text), and present here the median of all fields. The theoretical sensitivity  $\sigma^{\text{th}}$  corresponds to the expected sensitivity for the actual integration time, using the SOFIA FORCAST observation planning tools and assuming moderate water vapor content. All sensitivity values are in Janskies.

In order to determine the absolute sensitivity in the image, we use two methods. First, we manually determine a region in each cluster that visually appears devoid of flux. We calculate the sensitivity as if this background region was a source, by patching apertures in an annulus around this background location and calculating the standard deviation of

the obtained fluxes. We call this sensitivity measurement  $\sigma^{\text{man}}$ . The main downside of this method is that it requires a manual operation to select the appropriate background field, and hence could have more variation depending on which field we select. Second, we use a routine that iteratively isolates the pixel values above  $2\sigma$  of the image, in order to remove the contamination from our actual sources. The standard deviation of the resulting image is then calculated, and is multiplied by the square root of the number of pixels in an aperture of 3 pixel radius. This corresponds to a floor sensitivity  $\sigma^{\text{std}}$ . We present our results in Table II.7, where we also compare this sensitivity with the expected sensitivity  $\sigma^{\text{th}}$  obtained using the online calculator with the actual exposure time of our images. We note that usually, the theoretical values are more in agreement with our first method for F31 and F37, while more in agreement with our second method for F11 and F19.

#### II.5.4 Other photometry

While SOFIA provides mid-IR photometry, we looked in the literature for published fluxes on our targets in order to reconstruct more complete SEDs. In addition to our four SOFIA bands, our table includes data from 2MASS, *Spitzer*, and other instruments. Photometry from these sources is published in online catalogs, which we programmatically cross-reference with the positions of our targets. The closest target that corresponds to a Vizier location query is selected to be the correct catalog match. For the 2MASS data, the location of the target needs to be less than  $2''$  away from our coordinates for point sources, and  $5''$  for extended sources. For the *Spitzer* data, the matching radius is  $3''$  for point sources and  $10''$  for extended sources. In addition to automated online catalog searches, we also add values for sources in NGC2071 from Kempen et al. (2012).

For our two most clustered cases, the cores of NGC 2071 and IRAS 20050+2720,

the published catalogs do not have all available fluxes. We assume that the sources are so clustered that the source extraction software from these authors do not register them as point sources, due to confusion or saturation effects. Hence we adapt our own photometry routines for these clustered environments and obtain the fluxes directly from the calibrated Level 3 images, which are all available on the archive. In Table II.9, we compare our photometry results with published fluxes from Megeath et al. (2012) and Gutermuth et al. (2009) for isolated sources elsewhere in these same fields of view. We use the *Spitzer* handbook recommendations for aperture photometry on *Spitzer* archival images ( $2.4''$  aperture with and an annulus that extends from  $12$  to  $20''$ ). We find that our results are within 10% of these other authors' results, which can reflect a simple difference in exact aperture centroiding position.

TABLE II.9: Spitzer photometry comparison

SOFIA name	i1	i2	i3	i4
	Jy	Jy	Jy	Jy
NGC2071.1	0.060	0.056	0.004	-0.021
NGC2071.3	0.018	-0.010	-0.004	-0.047
NGC2071.4	0.090	-0.054	0.036	-0.066
NGC2071.5	-0.130	-0.109	-0.144	-0.139
IRAS20050.1	0.020	0.039	0.017	0.131
IRAS20050.3	0.181	0.122	0.082	0.121
IRAS20050.6	-0.044	-0.046	-0.092	-0.056

**Note:** Fractional difference between our own aperture photometry on *Spitzer* archival images and published *Spitzer* photometry from Megeath et al. (2012) for NGC2071, and Gutermuth et al. (2009) for IRAS20050+2720. When values are negative, it means that their photometry is lower than ours.

In some cases, we also found archival Herschel images, although no published photometry was available for most our sources. We then apply our same aperture photometry routines for those calibrated Herschel images, using aperture and background subtraction parameters from (Shimizu et al., 2016) for the PACS and SPIRE. We find also very good

agreement between our photometry results for the PACS 70  $\mu\text{m}$  band and the published *Spitzer* MIPS 70  $\mu\text{m}$  for some of these sources.

## II.6 Data products

### II.6.1 Mosaics

The SOFIA FORCAST images consist of  $\sim 200$  individual images, each representing a field at a given wavelength. Some fields are revisited multiple times when the entire observation could not happen in a single flight leg. These individual fields are processed and mosaiced together to form one single map for each wavelength and each cluster.

Before mosaicing the fields, we did a 2D background subtraction. This method divides the images into sections of  $50 \times 50$  pixels, estimates the median in each cell, and fits a 2D function to these median values. This function is then used to construct a smooth background, which is then completely removed from the image. Each background-subtracted image is then calibrated (using the calibration factor that is supplied by the FORCAST pipeline), and weighed by its exposure time before it is co-added into a mosaic in the WCS coordinate frame. Note that although these maps are useful to take a quick glance at the flux distribution and spot artifacts, the actual photometry described in the previous sections uses each individual raw field, before the mosaicing and without background subtraction. If a source is present in multiple fields, the photometry from each of these fields is combined to provide a better flux estimate.

In Fig. II.6 we present a variety of maps from our cluster sample. Each map is a three-color image (red: 37  $\mu\text{m}$ , green: 31  $\mu\text{m}$  and blue: 19  $\mu\text{m}$ ), and the scale and stretch

of each color is adjusted to balance each color. The three bands have 6.4, 6 and 5  $\mu\text{m}$  FWHM for 37, 31 and 19  $\mu\text{m}$  respectively.

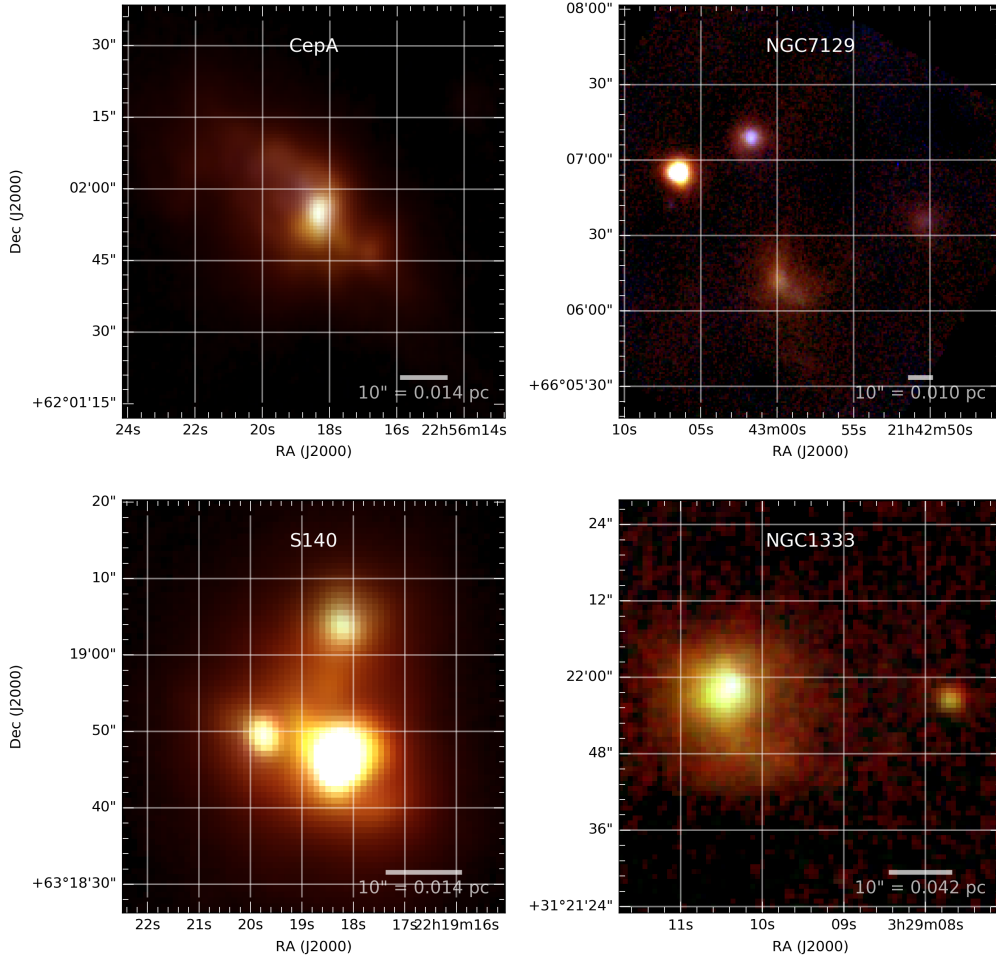


FIGURE II.6: RGB images of selected sample of sources (red: 37  $\mu\text{m}$ , green: 31  $\mu\text{m}$  and blue: 19  $\mu\text{m}$ ). In these images, the three bands have 6.4, 6 and 5 pixels FWHM for 37, 31 and 19  $\mu\text{m}$  respectively.

## II.6.2 Photometry and SEDs

The data produce a consolidated list of fluxes for most of our clusters, where we gather 2MASS, *Spitzer*, FORCAST, *Herschel*, SCUBA, and SMA data, when available, for  $\sim 90$

sources. Most sources are point sources for the SOFIA FORCAST 37  $\mu\text{m}$  band, but some sources present a certain spatial extension which was not known before.

A few other parameters are determined from the FORCAST data and shown in the data release: the  $R_{37}$ , which consists of the ratio of FWHM for the source and FWHM for the last observed calibrator; the spectral index and its uncertainty, computed from the 2.2  $\mu\text{m}$  - 37  $\mu\text{m}$  fluxes; and the bolometric luminosity for each source. An excerpt of the final table is shown in Table II.11.

TABLE II.11: Extract of NGC1333 photometry used for SED modeling.

SOFIA name	Coordinates	R37	Lbol	j	e_j	h	e_h	ks	e_ks	i1	e_i1	i2	e_i2	
NGC1333.1	03h29m07.7s +31d21m57.0s	0.746	8.385	0.0012	0.0001	0.0031	0.0003	0.0450	0.004	0.696	0.070	1.800	0.180	
NGC1333.2	03h29m10.3s +31d21m55.5s	2.232	27.832	0.2853	0.0285	0.6539	0.0654	0.9010	0.090	0.637	0.064	0.446	0.045	
NGC1333.3	03h29m01.5s +31d20m20.5s	0.904	8.104	0.0008	0.0001	0.0029	0.0003	0.0296	0.003	0.544	0.054	1.090	0.109	
NGC1333.4	03h29m11.1s +31d18m30.8s	1.103	3.056	0.0007	0.0007	0.0009	0.0009	0.0015	0.002	0.001	0.0007	0.004	0.0004	
NGC1333.5	03h29m10.6s +31d18m19.6s	1.623	2.786	0.0007	0.0007	0.0009	0.0009	0.0015	0.002	0.002	0.0002	0.007	0.001	
NGC1333.6	03h29m13.0s +31d18m13.8s	0.951	1.155	0.0007	0.0007	0.0009	0.0009	0.0015	0.0004	0.046	0.005	0.180	0.018	
		i3	e_i3	i4	e_i4	F11	e_F11	F19	e_F19	m1	e_m1	F31	e_F31	F37
NGC1333.1	03h29m07.7s +31d21m57.0s	3.060	0.306	2.550	0.255	0.225	0.169	1.502	0.208	—	0.260	6.886	0.640	10.994
NGC1333.2	03h29m10.3s +31d21m55.5s	0.448	0.080	0.913	0.128	8.414	0.596	36.517	2.562	—	—	106.490	7.457	135.723
NGC1333.3	03h29m01.5s +31d20m20.5s	1.690	0.211	3.060	0.306	1.681	0.131	6.902	0.493	—	0.069	9.256	0.656	9.406
NGC1333.4	03h29m11.1s +31d18m30.8s	0.005	0.001	0.004	0.0004	0.097	0.060	0.076	0.115	0.607	0.061	1.785	0.209	3.040
NGC1333.5	03h29m10.6s +31d18m19.6s	0.010	0.001	0.011	0.001	0.114	0.093	0.150	0.119	0.771	0.077	1.946	0.234	2.166
NGC1333.6	03h29m13.0s +31d18m13.8s	0.274	0.027	0.320	0.032	0.160	0.035	0.570	0.093	0.735	0.074	1.446	0.180	1.806
		e_F37	m2	e_m2	H70	e_H70	H160	e_H160	H70	e_H70	H160	e_H160	H250	e_H250
NGC1333.1	03h29m07.7s +31d21m57.0s	0.948	49.300	4.930	52.724	5.272	66.529	35.197	52.724	5.272	66.529	35.197	71.541	14.258
NGC1333.2	03h29m10.3s +31d21m55.5s	9.507	—	—	70.039	7.004	77.574	20.036	70.039	7.004	77.574	20.036	87.661	15.014
NGC1333.3	03h29m01.5s +31d20m20.5s	0.695	23.400	2.340	20.218	2.022	78.316	7.832	20.218	2.022	78.316	7.832	101.472	18.943
NGC1333.4	03h29m11.1s +31d18m30.8s	0.341	—	—	16.609	1.661	53.689	5.369	16.609	1.661	53.689	5.369	57.215	6.293
NGC1333.5	03h29m10.6s +31d18m19.6s	0.377	20.600	2.060	14.627	1.463	49.868	4.987	14.627	1.463	49.868	4.987	52.536	6.166
NGC1333.6	03h29m13.0s +31d18m13.8s	0.345	4.290	0.429	1.527	3.883	4.702	13.332	1.527	3.883	4.702	13.332	29.105	6.272
		H350	e_H350	H500	e_H500	S850	e_S850	F1100	e_F1100	S1300	e_S1300	α	e_α	
NGC1333.1	03h29m07.7s +31d21m57.0s	45.559	17.857	24.264	16.301	—	—	1.300	0.130	—	—	0.280	0.564	
NGC1333.2	03h29m10.3s +31d21m55.5s	51.506	16.114	24.742	13.062	—	—	—	—	—	—	1.243	—	
NGC1333.3	03h29m01.5s +31d20m20.5s	70.907	17.371	40.867	11.474	—	—	1.500	0.150	—	—	0.714	0.385	
NGC1333.4	03h29m11.1s +31d18m30.8s	38.449	6.033	18.594	4.666	—	—	2.000	0.200	—	—	1.864	0.458	
NGC1333.5	03h29m10.6s +31d18m19.6s	36.232	6.189	18.007	4.878	—	—	2.000	0.200	—	—	1.705	0.273	
NGC1333.6	03h29m13.0s +31d18m13.8s	34.781	8.007	21.255	6.628	—	—	0.630	0.063	—	—	1.001	0.501	

**Note:** The table contains the source name, coordinates in J2000, the ratio of R37 =  $\text{FWHM}_{\text{source}}/\text{FWHM}_{\text{cal}}$ , the bolometric luminosity determined by integrating the data points, followed by the photometry and its  $1\sigma$  error in the 2MASS bands (j, h, ks), IRAC bands (i1, i2, i3, i4 at 3.6, 4.5, 5.8 and 8  $\mu\text{m}$  respectively), the FORCAST bands (F11, F19, F31, F37), the *Spitzer* MIPS bands (m24 and m70), the Herschel PACS and SPIRE bands (H70, H160, H250, H350 and H500), the SCUBA band (S850), the BOLOCAM band (F1100) and the SMA continuum band (S1300). The complete version of this table is made available electronically.

### II.6.3 Fitted physical parameters

The spectral index ( $\alpha \equiv (d \log(\lambda F_\lambda) / d \log \lambda)$ ) distribution for the point sources in our sample is shown on the left of Fig. II.9. Most sources have positive spectral index, indicative of a rise in the SED and a large proportion of long-wavelength emission. These objects are more dusty, and believed to be younger than objects with negative spectral index. A closer inspection reveals that targets with negative index mostly lie in the Ophiuchus cluster, and can consist in late Class I objects which have already cleared most of their envelopes.

The data tables also include all of the physical parameters derived using the technique from Section II.7, as well as their uncertainties.

## II.7 SED fitting

SED fitting is prone to many degeneracies: usually many geometrical and physical parameters are used to construct detailed radiative transfer models, but only a handful of measurement points are available to fit, leading to a dramatically under-constrained problem. As our starting point of our investigation of the SEDs of these sources, we used the *sedfitter* tool from (Robitaille et al., 2006). These authors computed a large grid of tens of thousands of SED models using a radiative transfer code by (Whitney et al., 2003a), by varying 14 geometrical and physical parameters in the dust density grid such as the size of the disk, the accretion rates, the radius and mass of the envelope, etc. The models are then evaluated in the bands corresponding to our data, and a  $\chi^2$  metric is evaluated for each model. By exploring the distribution of  $\chi^2$ , we noticed, as expected, the very large correlations between the parameters which is indicative of many local minimas in

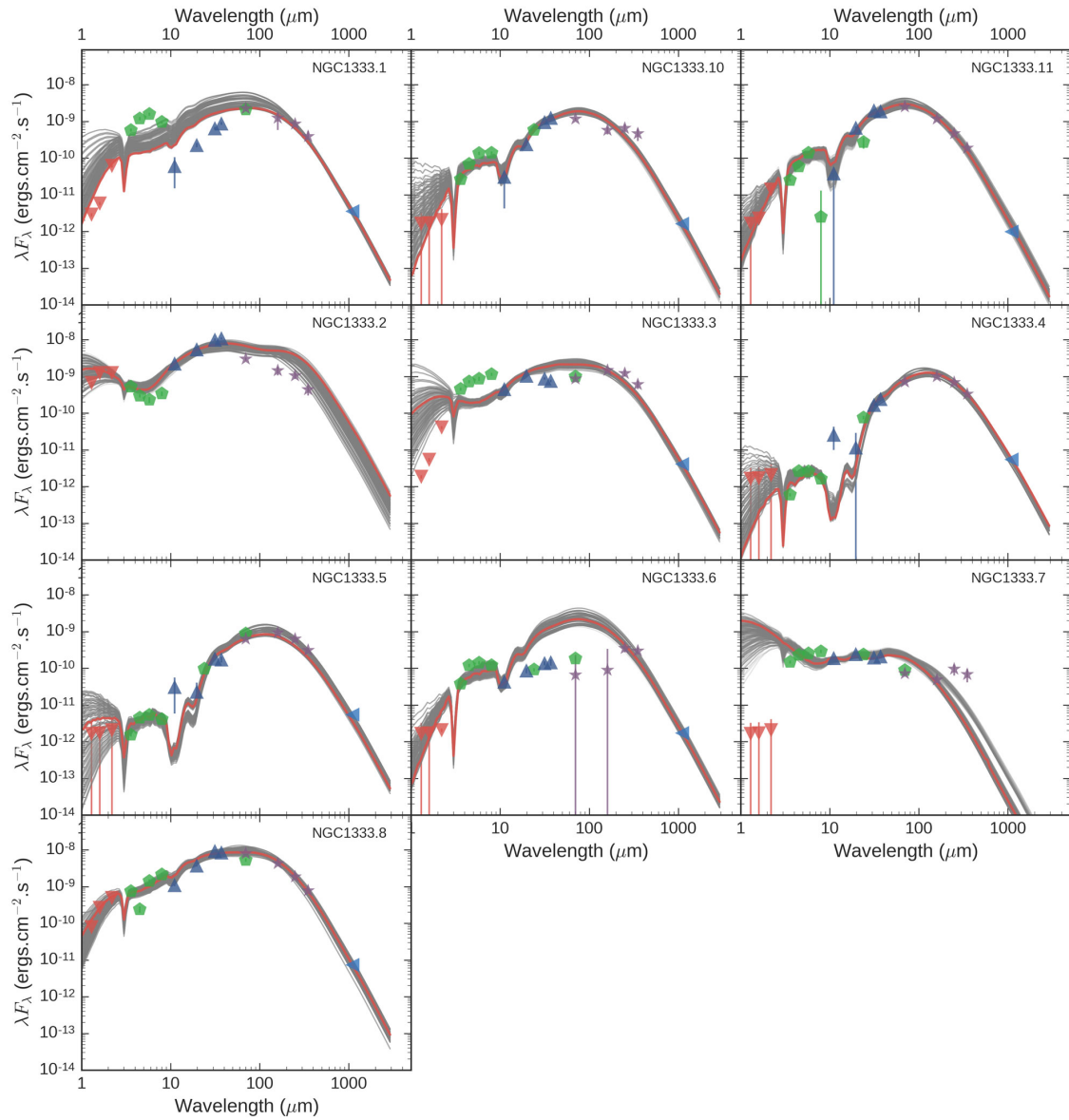


FIGURE II.7: SEDs of the point sources in NGC1333. The red curve represents the best fit. The grey curves represent all the fits with  $R$  within 0.5 of the best fit. Red triangles: 2MASS. Green diamonds: *Spitzer* (our photometry or data from existing catalogs). Dark blue triangles: FORCAST (our data). Purple stars: *Herschel* (our photometry). Green triangles: SCUBA 850  $\mu\text{m}$  and SMA 1.3 mm data from (Kempen et al., 2009) and (Kempen et al., 2012). Left-pointing blue triangles: 1.1 mm data from Enoch et al. (2009).

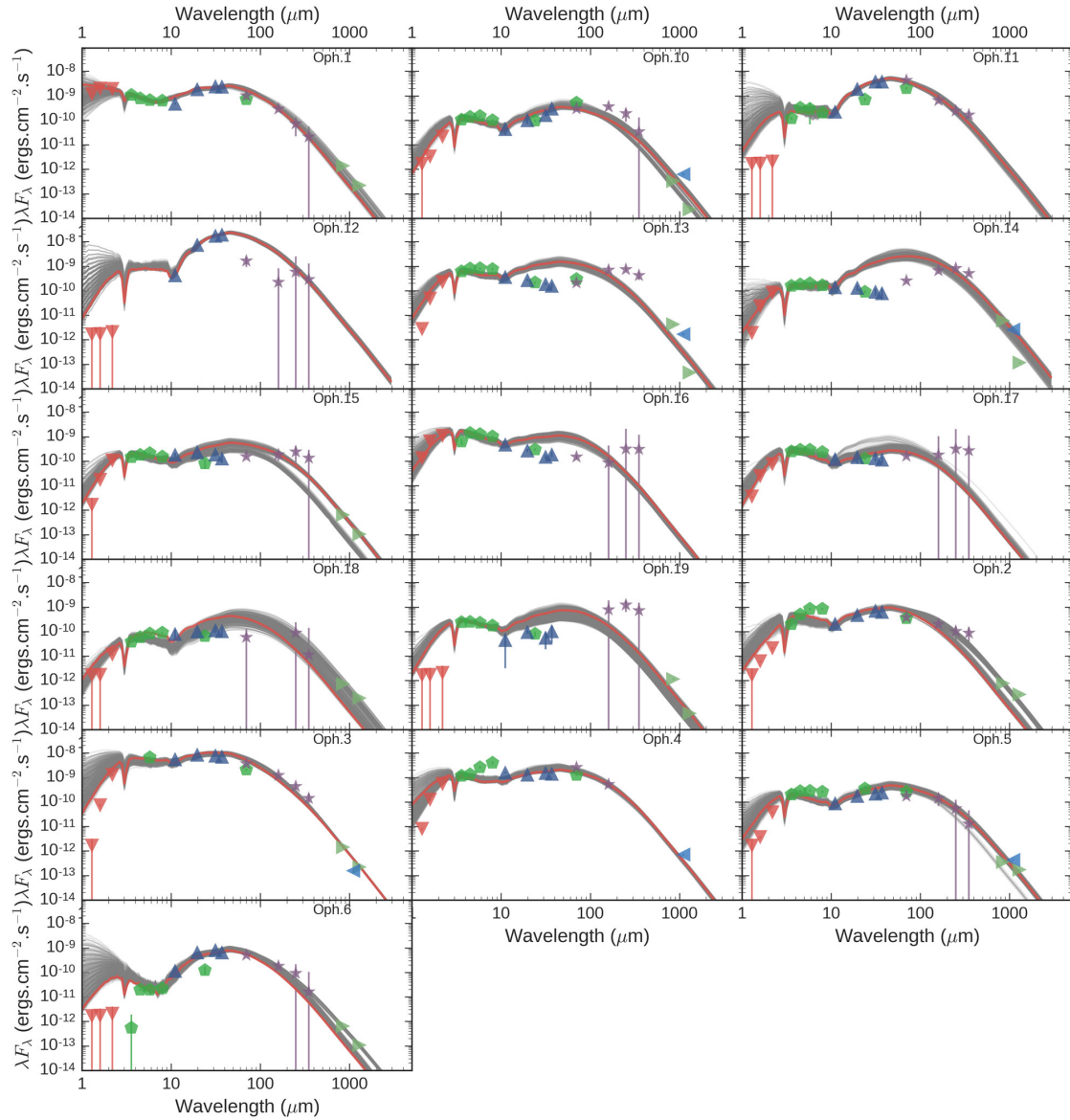


FIGURE II.8: SEDs of the point sources in the Ophiuchus cluster. Same legend as Fig. II.7

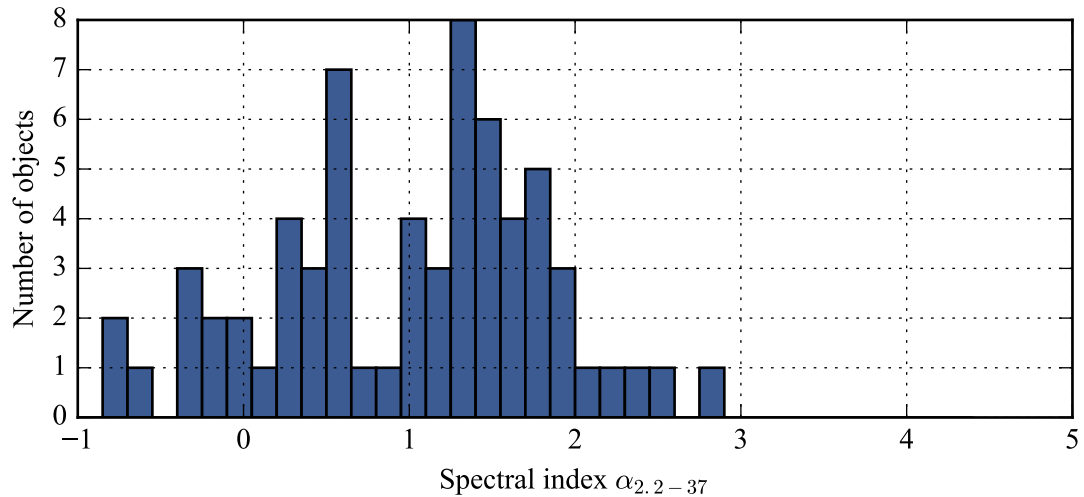


FIGURE II.9: Spectral Index distribution of point sources. *Left:* standard determination of the spectral index, using 2MASS and *Spitzer* from  $2\text{ }\mu\text{m}$  to  $24\text{ }\mu\text{m}$ , when data is available. *Right:* Determination of the spectral index using data from 2MASS, *Spitzer* and our FORCAST data up to  $37\text{ }\mu\text{m}$ . The distribution changes significantly when you account for the longer fluxes in these clustered regions.

the 14-dimensional grid. Hence, inferring geometrical and physical parameters from such a grid can be misleading.

### II.7.1 A custom grid of models

We use Hyperion (Robitaille, 2011, see also in Section I.3.3) to develop our own capability of calculating SEDs and understand the sensitivity of these parameters on the SED shape of our sources. Based on our investigation, the degeneracy between viewing angle and multiple geometrical parameters is considerable. The sensitivity of the SED to disk properties is minimal, as most of the SED properties are determined mostly by the envelope for younger objects like most of the ones we observed with SOFIA. Parameters of the central source such as the mass, radius and temperature are primarily important when they are combined into one single term, which is the central luminosity. Similarly, the luminosity created when simulating a disk accreting onto the central object can not be distinguished from a

more luminous central object and a non-accreting disk. Finally, we find that there is very little difference between Ulrich envelope models (Ulrich, 1976) and standard power-law envelopes (see for example Fig. 14 from Whitney et al. (2013)), except that the latter can more directly be related to physical parameters such as the envelope mass.

From these findings, we created a simplified grid of models by significantly reducing the number of parameters. Table II.13 introduces most of the geometric and physical parameters that are available in Hyperion, for the central source, the disk, the envelope and the bipolar cavity. Most parameters are set to constant values which we determined as average values using literature examples as well as our own investigations for the objects we try to study. The varied parameters are shown at the bottom of the table: the inclination angle, the central luminosity (irrespective of whether it is caused by the central star or by accretion), the envelope mass, the external extinction and the scaling factor (explained below). The only two physical parameters that we vary are the luminosity and the envelope mass. While others (e.g. Furlan et al., 2016) have also attempted to reduce the number of parameters for their fitting, they still include more parameters such as the disk radius, but generally conclude that they are not able to properly constrain all of their parameters.

Unlike most authors, who use multiple kinds of dust models for different regions of the SED (which add complexity and number of parameters), we simply use the same dust model (OH5) for both the envelope and the disk, and assume a 1:100 dust-to-gas ratio. By doing so, we tend to overestimate the short-wavelength emission from SEDs, because the OH5 model we use only features isotropic scattering whereas most dust grains appear to be forward-scattering (**Draine:2011tr**).

We constructed a wrapper program that can run the Hyperion software for the parameters in this grid. Because of time and resource limitations, a moderate number of

TABLE II.13: SED model grid.

Parameter	Description	Values	Units
<b>Constant parameters</b>			
Central source			
$M_*$	Stellar mass	1	$M_\odot$
$T_*$	Stellar temperature	4000	K
Disk			
Type	Flared or alpha disk	Flared	
$M_{\text{disk}}$	Disk mass	0.001	$M_\odot$
$R_{\text{disk}}^{\max}$	Disk outer radius	100	au
$R_{\text{disk}}^{\min}$	Disk inner radius	sublimation radius	au
$\beta$	Flaring parameter	1.25	
$p$	Disk surface density exponent	-1	
$r_0$	Reference distance for scale height	$R_{\text{disk}}^{\min}$	au
$h_0$	Disk scale height at $r_0$	$0.01 \times R_{\text{disk}}^{\min}$	au
$d$	Dust	OH5	
Envelope			
Type	Power-law or Ulrich	Power-law	
$R_{\text{env}}^{\min}$	Envelope inner radius	$R_{\text{disk}}^{\min}$	au
$R_{\text{env}}^{\max}$	Envelope outer radius	5000	au
$\alpha$	Power	-1.5	
$r_0^{\text{env}}$	Reference radius	$R_{\text{env}}^{\min}$	au
$d$	Dust	OH5	
Cavity			
$r_0^{\text{cav}}$	Cavity outer radius	$R_{\text{env}}^{\max}$	au
$\theta_0$	Opening angle at $r_0^{\text{cav}}$	10	degrees
	Flaring exponent	1.5	
$\rho_0$	Density at $r_0^{\text{cav}}$	0	$\text{g cm}^{-3}$
$\alpha_e$	Density profile exponent	0	
<b>Fitted parameters</b>			
$i$	Inclination angle	0 to 90 in 10 constant increments of $\cos i$	degrees
$L_*$	Central luminosity	$5 \times 1.5^p$ for $p = -4, -3, \dots, 10$ (from 0.99 to 288)	$L_\odot$
$M_{\text{env}}$	Envelope mass	$0.01 \times 1.5^p$ for $p = -2, -1, \dots, 19$ (from 0.001 to 22.17)	$M_\odot$
$A_V$	External extinction	0, 1, ..., 14	mag
$s$	Scaling	0.7, 0.85, 1, 1.5, 1.3	

photons was chosen, which can increase the noise at short wavelengths. The details of our modeling parameters, which will be familiar to the Hyperion user, are described in Table II.15. Note that models of more than  $1 M_{\odot}$  are actually run with  $1 \times 10^6$  photons for imaging, in order to obtain acceptable SNR at short wavelengths.

TABLE II.15: Hyperion simulation parameters.

Number of photons (initial)	$2 \times 10^5$
Number of photons (imaging)	$2 \times 10^5$
Number of photons (raytracing sources)	$1 \times 10^6$
Number of photons (raytracing dust)	$1 \times 10^6$
Lucy max iterations	6
Max photon interactions	$1 \times 10^5$
Geometrical grid parameters (radial, theta and azimuthal)	400, 199, 2
MRW	True

The grid is composed of  $\sim 418$  models which are modeled with Hyperion. For models with  $M_{\text{env}} > 0.5 M_{\odot}$ , we interpolate the grid in mass by increments of 20%, which allows for a finer sampling at higher masses, but increases the number of individual models to 958. Each model is sampled at 10 inclinations, 15 values for external extinction, and five different scaling factors, for a total of 718 500 grid models. Each model is evaluated at all relevant observing bands, from the 2MASS bands all the way to the 1.3 mm SMA bands. Given the sparsity of the grid, and the relatively simple model used, we do not apply color correction to the fluxes, nor do we convolve the model fluxes with the band transmission function: the resulting corrections fall well within our approximations, and do not affect significantly the outcome of the fitting.

The scaling factor is used to represent the uncertainty in the distance determination (e.g. Robitaille et al., 2006), but it can also be considered as a scaling to represent modestly different luminosities (Furlan et al., 2016). Indeed, Furlan et al. (2016) show that, to first order, changing luminosities by a small amount is approximately equivalent to scaling the

SED in flux. In their grid, they use a scaling factor that ranges from 0.5 to 2.0, which allows them to have factors of 2.0 between their luminosity steps. We choose a more conservative approach by actually running the grid at closer luminosity steps (factor of 1.5) and hence have a smaller range of scaling factors.

The extinction parameter is used to represent extinction by material along the line of sight that is *outside* of the core: foreground material. A discussion of this parameter is given in the following sections.

### II.7.2 Fitting method

In order to determine which model fits the data best, we adopt a metric defined by Fischer et al. (2012) and Furlan et al. (2016):

$$R = \frac{1}{N} \sum_i w_i |\log[F_{\text{obs}}(\lambda_i)] - \log[F_{\text{mod}}(\lambda_i)]|, \quad (\text{II.1})$$

where  $i$  are the indices of the valid data points, the weights  $w_i$  correspond to the inverse of the fractional uncertainty of each measurement,  $F_{\text{obs}}$  and  $F_{\text{mod}}$  are the observed and model fluxes respectively, and  $N$  is the number of valid measurements. For our models, we set the fractional uncertainty to a minimum of 10%, to avoid having a few points completely drive the fit. Early versions of the fitting routines, which used the published  $1\sigma$  uncertainties would completely skew the results by putting all the weight into a few flux measurements. This was most notable for the *Spitzer* IRAC points, which only have a few percent uncertainties. We chose to override these uncertainties.

Furlan et al. (2016) discuss in more detail the meaning of this metric, which differs from a standard  $\chi^2$  metric such as the one used by Robitaille et al. (2007).  $R$  represents a weighted average of the logarithmic deviations between the observations and the model.

It is important to note that, although it is normalized, it does not have a statistical interpretation like the standard  $\chi^2$  metric. In particular, models with fewer data points or large measurement uncertainties will tend to have smaller values of  $R$ , even if the fit is poor.

For each source, we calculate  $R$  for each model in our grid. The model with the smallest value for  $R$  is the best-fitting model by this metric, but given our sparse sampling and the errors of our observations, this is not necessarily the most likely model to best fit the data. We can consider two extremes: in the first, the best fit has a value of  $R$  which is much lower than other models. Then, it is clearly the best fit. In the second case, let's suppose that the 1000 best-fitting models lie very close to the best  $R$ . In this case, concluding that the model that best fits our observations (and from which will interpret physical quantities) is the one with the minimum  $R$  is too strict and does not account for the uncertainties that are present.

In practice, all of our models fall in that second case. After visual inspection of the fits, we conclude there is very little significant difference between values of  $R$  which are separated by  $\sim 0.5$ . They all can be considered equally good (or bad) fits. Hence, for a robust measure of the best-fitting model parameters, we choose the mode (the most likely value) of the parameters from models which are within  $R_{\min}$  and  $R_{\min} + 0.2$ . The error on the parameter estimate is then estimated using the models within  $R_{\min}$  and  $R_{\min} + 0.5$ , since these models all similarly fit, and is described in the next section.

Because we use exclusively the OH5 dust model, which we know overestimates the short-wavelength fluxes, we expect to overestimate the extinction required to match the observations. For this reason, we choose to ignore the 2MASS J and H band data points, which drive the extinction values up dramatically and sometimes leads the fit towards non

realistic solutions. However, we choose to keep the  $2\mu\text{m}$  data point.

### II.7.3 Overview of derived parameters

The distribution of the best fit solutions of the envelope mass and central luminosity is shown in Fig. II.10 for the clusters for which we have long-wavelength data (Ophiuchus and NGC1333). Our sample covers a broad range of masses, but is naturally biased towards high luminosities given our instrumental sensitivity and cluster selection.

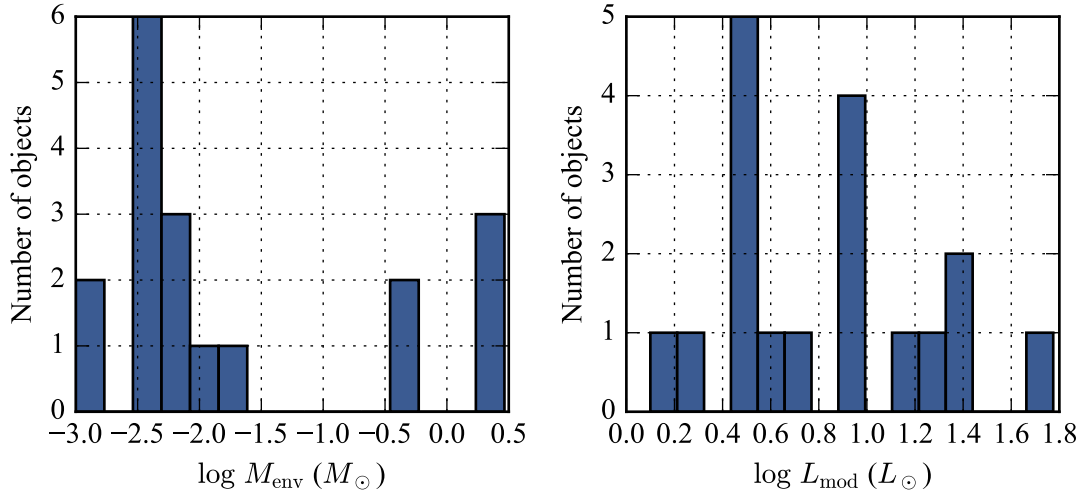


FIGURE II.10: Fitted envelope mass and luminosity distribution for all observed point sources in Ophiuchus and NGC1333, where long-wavelength data is available.

From visual inspection, data with  $R$  less or close to 1 appear to fit the data well. Larger  $R$  show less good fits. The distribution of  $R$  for all the isolated point sources is shown in Fig. II.11. Note that targets where less data points are available, or where data points are more noisy, usually have lower  $R$  than targets with a lot of available data points, even if the fits are not necessarily as good. This has also been observed by (Furlan et al., 2016) and is one of the drawbacks of using this  $R$  metric.

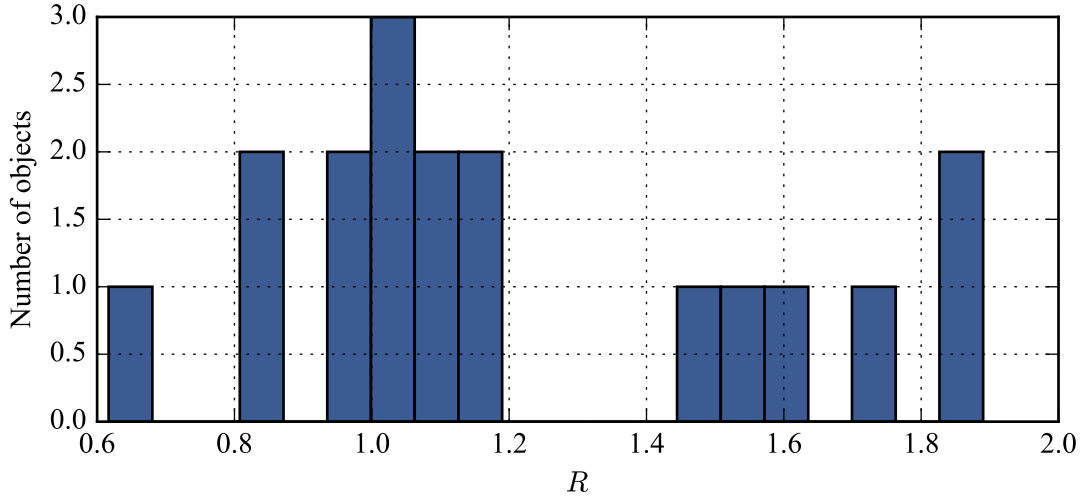


FIGURE II.11:  $R$  distribution across all observed point sources in Ophiuchus and NGC1333, where long-wavelength data is available.

We find that this is a major limitation and inconsistency to all known SED fitting methods. Furlan et al. (2016) fit for extinction more than we do: they allow the external extinction to go up to  $A_V = 40$  for some of their sources, and use all of the 2MASS bands in their fitting. It is not consistent to assume that so much dusty material is present along the line of sight and only affect the short wavelengths, while not also being observed at longer wavelengths. Since the dust is optically thin at longer wavelengths, the far-infrared and submillimiter observations should account for this material which is obscuring the shortest wavelengths.

Our exploration with the fitting routine shows that limiting the external extinction helps by forcing more inclined geometries, where the light from the central star passes through the disk before reaching us. However, we were not able to account for the entirety of the short wavelength extinction by doing this, as the mid-infrared wavelength (IRAC and FORCAST bands) are also affected dramatically by more inclined geometries, which can compromise the fits. This could indicate a fundamental limit to our geometrical

representation of YSOs.

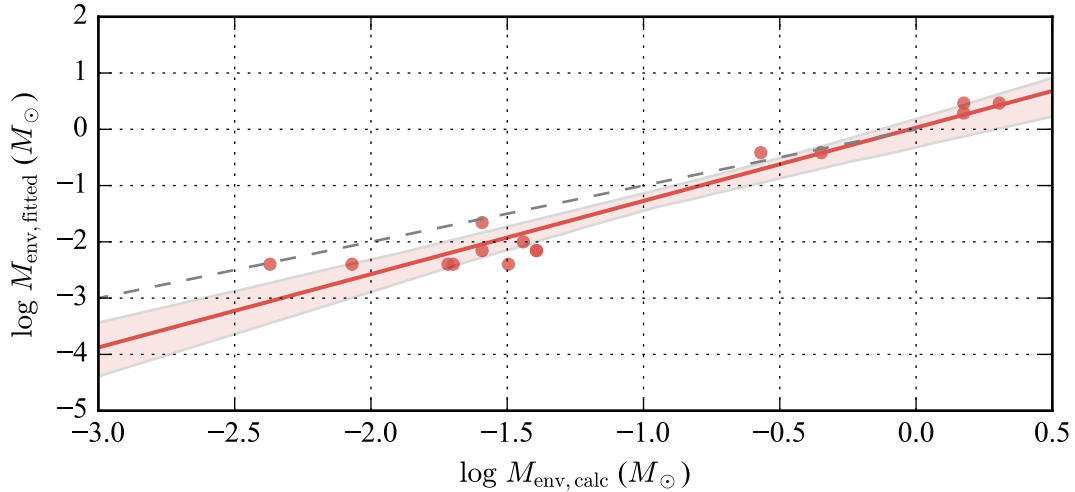


FIGURE II.12: Estimated mass vs calculated mass for the point sources which have sub-millimeter data.

For the clusters which do have submillimeter data points, we can use the traditional mass estimate described in Section I.3.2 with the 1.1 mm or 1.3 mm fluxes. For this calculation, we use an effective dust temperature of 20 K, assuming an opacity of  $0.0114 \text{ cm}^2 \text{ g}^{-1}$  and  $0.009 \text{ cm}^2 \text{ g}^{-1}$  for 1.1 mm and 1.3 mm, respectively. Note that this measurement is very sensitive on these assumptions; for example, lowering the dust temperature estimate to 10 K increases the mass estimate by a factor of 3.

We find that our fitted mass estimates agree with this traditional method of deriving masses, as shown in Fig II.12. For lower masses, however, our fits tend to underestimate the mass compared to the derived quantities. This could be explained since most of the lower-mass envelopes belong to more evolved objects, which can thus have higher dust temperatures due to less opacity: the derived mass, assuming a temperature of 20 K, would then overestimate the amount of material in the envelope.

A summary of our fit results for Ophiuchus and NGC1333 is shown in Table II.17.

Note that the luminosity that is used in this analysis is always the luminosity multiplied by the scaling factor  $s$ , under the assumption that the SED scales for small changes in luminosity. This scaling factor also represents a fundamental uncertainty in the distance measurement to our targets, as a distance error of 10% would cause a luminosity estimate that would differ by 20%.

We note that the fitted luminosity and bolometric luminosity are in agreement for low inclination angles, but  $L_{\text{mod}}$  tend to be higher than  $L_{\text{bol}}$  for more inclined geometries. This is expected since for high inclinations a large fraction of the emission is not directed towards the observer (see, e.g. Furlan et al., 2016, for a discussion).

TABLE II.17: Fitted parameters for the point sources in Ophiuchus and NGC1333 where long-wavelength photometry is available.

SOFIA Name	Coordinates (J2000)	FWHM/FWHM <sub>cal</sub>	$\alpha$	$R$	$M_{\text{env}}$ ( $M_{\odot}$ )	Calc. $M_{\text{env}}$ ( $M_{\odot}$ )	$L_{\text{mod}}$ ( $L_{\odot}$ )	$L_{\text{bol}}$ ( $L_{\odot}$ )	i ( $^{\circ}$ )	$A_V$ (mag)
NGC1333.1	03h29m08s +31d21m57s	0.75	0.28	3.40	$0.58 \pm 0.38$	0.97	$5.6 \pm 3.12$	8.38	0.0	12
NGC1333.10	03h28m57s +31d14m15s	0.80	1.83	1.12	$0.38 \pm 0.24$	0.45	$5.6 \pm 1.69$	4.82	18.7	14
NGC1333.11	03h28m37s +31d13m30s	1.02	1.69	0.99	$0.38 \pm 0.16$	0.27	$7.7 \pm 1.37$	7.47	18.7	12
NGC1333.3	03h29m02s +31d20m21s	0.90	0.71	3.29	$1.95 \pm 0.82$	1.12	$3.5 \pm 0.80$	8.10	0.0	14
NGC1333.4	03h29m11s +31d18m31s	1.10	1.86	0.83	$2.92 \pm 0.50$	1.50	$2.8 \pm 0.42$	3.06	18.7	14
NGC1333.5	03h29m11s +31d18m20s	1.62	1.70	1.05	$1.95 \pm 0.39$	1.50	$2.9 \pm 1.00$	2.79	18.7	9
NGC1333.6	03h29m13s +31d18m14s	0.95	1.00	2.28	$0.58 \pm 0.16$	0.47	$4.3 \pm 1.72$	1.16	18.7	14
NGC1333.7	03h28m43s +31d17m35s	1.19	1.08	1.88	$0.004 \pm 0.001$	–	$9.6 \pm 2.16$	1.36	50.8	0
NGC1333.8	03h29m04s +31d16m04s	0.77	1.14	1.03	$2.92 \pm 1.13$	2.02	$14.3 \pm 2.24$	35.11	0.0	12
NGC1333.9	03h28m56s +31d14m37s	0.80	2.79	2.63	$2.92 \pm 0.5367$	1.72	$19.5 \pm 3.67$	24.28	18.7	14
Oph.1	16h27m10s -24d19m13s	0.92	0.27	0.62	$0.007 \pm 0.002$	0.04	$9.6 \pm 1.80$	3.63	65.1	4
Oph.10	16h27m18s -24d28m55s	1.26	0.50	1.89	$0.004 \pm 0.003$	0.004	$1.9 \pm 0.38$	0.55	61.7	14
Oph.13	16h27m30s -24d27m43s	0.00	-0.37	3.46	$0.004 \pm 0.002$	0.01	$6.5 \pm 1.63$	1.49	65.1	14
Oph.14	16h27m28s -24d27m21s	1.89	-0.13	2.35	$0.076 \pm 0.040$	0.02	$2.9 \pm 0.78$	0.95	18.7	14
Oph.15	16h27m29s -24d39m17s	1.25	0.10	1.09	$0.004 \pm 0.002$	0.02	$2.8 \pm 0.59$	0.55	54.6	12
Oph.16	16h26m24s -24d24m48s	1.80	-0.76	1.49	$0.001 \pm 0.001$	–	$17.7 \pm 4.70$	1.66	74.7	9
Oph.17	16h26m24s -24d24m39s	0.96	-0.09	1.00	$0.001 \pm 0.002$	–	$4.3 \pm 0.88$	0.63	77.8	14
Oph.18	16h26m17s -24d23m45s	1.18	0.63	1.15	$0.010 \pm 0.004$	0.04	$1.3 \pm 0.21$	0.22	65.1	14
Oph.19	16h26m30s -24d23m00s	2.51	0.57	1.15	$0.004 \pm 0.002$	0.01	$3.5 \pm 0.74$	1.10	58.2	13
Oph.2	16h26m44s -24d34m48s	0.93	0.83	2.08	$0.004 \pm 0.002$	0.05	$5.0 \pm 0.97$	1.19	77.8	14
Oph.3	16h27m09s -24d37m18s	0.99	0.57	1.54	$0.007 \pm 0.002$	0.04	$59.5 \pm 11.99$	13.39	37.9	10
Oph.5	16h27m07s -24d38m15s	1.31	0.31	1.74	$0.004 \pm 0.002$	0.03	$2.9 \pm 0.66$	0.53	68.4	14
Oph.6	16h27m16s -24d38m46s	1.29	2.54	0.83	$0.004 \pm 0.003$	0.02	$9.6 \pm 3.41$	0.73	90.0	12
Oph.7	16h27m28s -24d39m34s	0.97	1.35	1.57	$0.022 \pm 0.004$	0.03	$26.6 \pm 4.90$	6.47	74.7	14
Oph.8	16h27m37s -24d30m35s	1.02	0.55	1.06	$0.007 \pm 0.002$	0.03	$26.6 \pm 5.15$	5.00	80.9	14
Oph.9	16h27m22s -24d29m54s	–	0.51	2.08	$0.001 \pm 0.001$	0.01	$11.8 \pm 2.71$	0.99	80.9	14

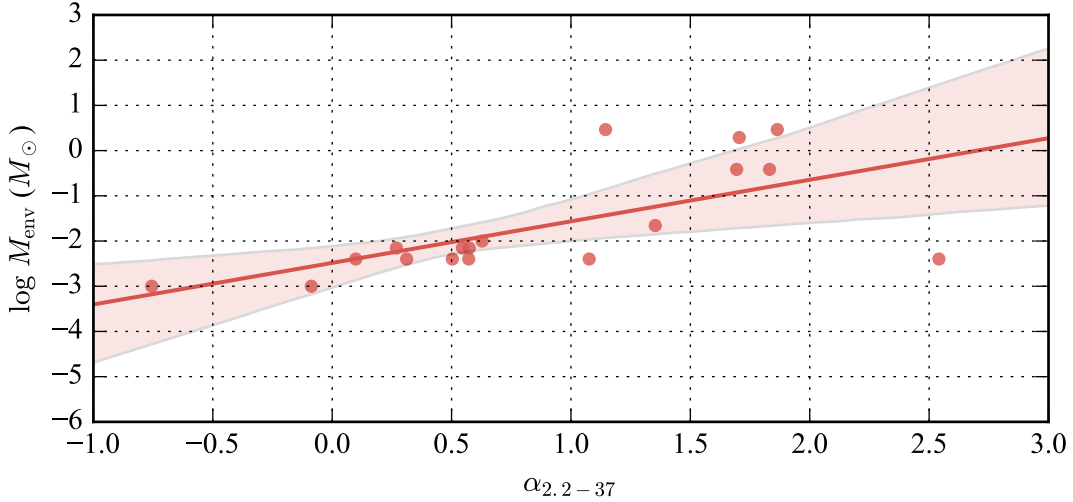


FIGURE II.13: Mass versus spectral index for the point sources which have sub-millimeter data, and for which the fits have  $R < 2$ .

By examining the envelope mass fitted values with respect to the measured spectral index  $\alpha$ , we note that there is a correlation (Fig. II.13). This correlation appears to be good for  $\alpha < 1$ , but much more loose for  $\alpha > 1$ .

#### II.7.4 Estimating parameter uncertainty

Parameter uncertainty estimation is important to quantify the confidence in a given fit, without which no meaningful conclusion can be drawn about the scientific meaning of the parameters. This estimation is also one of the most difficult aspect of this fitting process, since it really depends on the method used and the modeling strategy; it hard to compare it with the findings of different authors who might use a different strategy.

In this work, we propose a relatively model-independent methodology to derive the uncertainty on the best fit. First, we determine the best fit for a given parameter as the mode of the parameter values from the models that fit within  $[R_{\min}, R_{\min} + 0.2]$ . This is statistically more robust than picking simply the model with the lower  $R$ , since, given our

uncertainties and approximations, there is no statistically-significant difference between models that fit within that range.

Once this best fit value is determined for all parameters, the uncertainty is determined using all models that fit within  $[R_{\min}, R_{\min} + 0.5]$ . We determine three quantities from these models: the standard deviation from the best fit; the median absolute deviation from the best fit; and the skewness of the distribution. All of those parameters accompany the data table which is released with this work.

We admit that the choice of the  $R$  intervals are empirical, so they might not work as well for other authors. However, since the metric  $R$  is not model-dependent but instead is a type of *distance* between our models and our observations, we think that similar values will still lead to satisfying parameter and uncertainty estimates for other authors. One limitation could occur from the density of the grid: if the models are so sparse that there are only a handful of model within each interval used in the uncertainty estimation, this could lead to errors.

### II.7.5 Discussion

In this exercise, several factors have been omitted for simplicity. First, the models we use have an axisymmetric geometry which is unlikely to account for realistic mass distributions in the envelope and the disk. Second, we ignore the surrounding medium and consider it devoid of emission (hence of dust). In reality, the transition to the surrounding medium is likely much closer to a continuum. Third, we assume that the only heating source is located at the center of the YSO. The heating source consists of both the light from the star, and from the accretion luminosity, which can not be distinguished from our point of view. It is important to realize that external heating can also play a role in raising the

dust temperature and changing the SED signature. The impact of the interstellar heating is explored in Furlan et al. (2016), who show that it can have a substantial effect on the SED - but they nevertheless do not include this parameter in their grid, since it is too case-specific. The Hyperion radiative transfer code that is used to model our grid could accommodate for external radiation fields as well, and this could be a future addition to our model. Finally, the observations that form our SEDs were not taken simultaneously, so it is possible for the YSO to change over the period of years that the various wavelengths were observed. This phenomenon is known as YSO variability and is described for example in [ADD REFERENCE]

Given the relative simplicity of the model grid that we constructed, most of observations are fit well and parameters have acceptable uncertainties. This further confirms the degeneracies that exist when trying to put too much physics into very elaborate models: it is difficult to draw physical meaning just by looking at the SED. The difference in the various resolutions, sensitivity, and photometric techniques for each wavelength in the SED prevents a thorough analysis of the object's geometric details, especially when located in very clustered environment when extended emission and nearby sources can contaminate the measurements. We argue that more complex models would not help in estimating the physical parameters of YSOs - but instead, this work highlights the need for higher angular resolution at wavelengths longward of  $37\,\mu\text{m}$ . We note from our results that although the envelope mass appears to correlate with spectral index, the relationship is rather loose. In other words, sources with only data up to  $37\,\mu\text{m}$  are likely to have poorly constrained masses, suggesting that SEDs could have the same near- to mid-IR response while having substantially different long wavelength response (see Section II.8.1).

Similarly to Furlan et al. (2016), we find that the distribution of inclination angles for

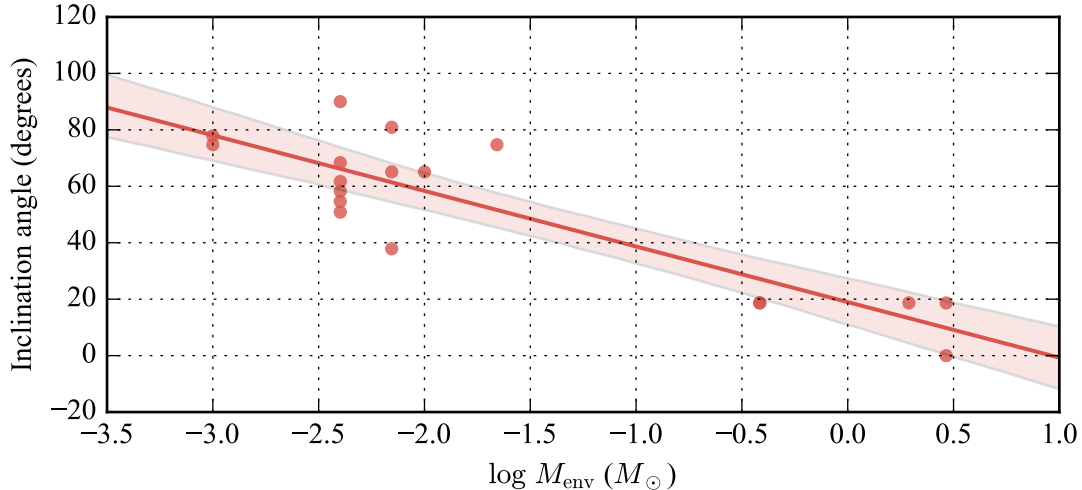


FIGURE II.14: The correlation between inclination angle and envelope mass might indicate a degeneracy of the modeling software.

the best fits is not uniform, which is not intuitive. There is no reason why protostars should have a selection effect in their inclination angle with respect to us. This is indicative of an artifact of the fitting process, and possibly a degeneracy between inclination angle and envelope mass (see Fig. II.14), which is much more prominent when no long-wavelength data is available.

Finally, we observe that there is no statistically significant relationship between the spectral index and the total luminosity of the object. This is perhaps not too surprising, as the total luminosity of the object is not expected to significantly change with its evolutionary stage. In addition, this also points out that there are no significant cross-correlation between the luminosity and envelope mass in our model.

## II.8 Application to two clusters

In our sample, we focus our attention on IRAS 20050+2720 and NGC 2071 that show very clustered sources which are resolved for the first time in the mid-IR with our observations

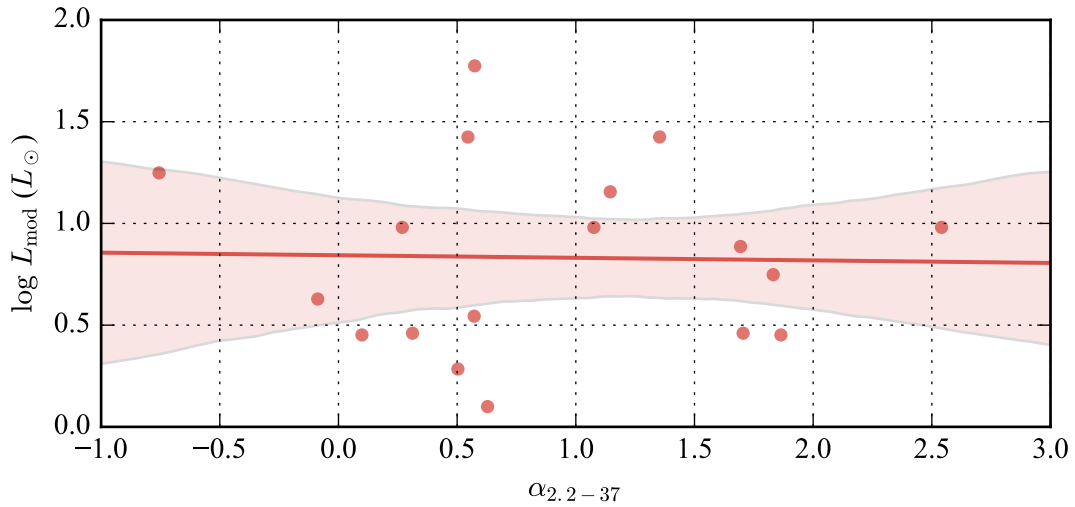


FIGURE II.15: There is no apparent correlation between fitted luminosity and spectral index.

with FORCAST. The fields that were observed are shown in Fig. II.16, superimposed with IRAC 3-color images to provide some context.

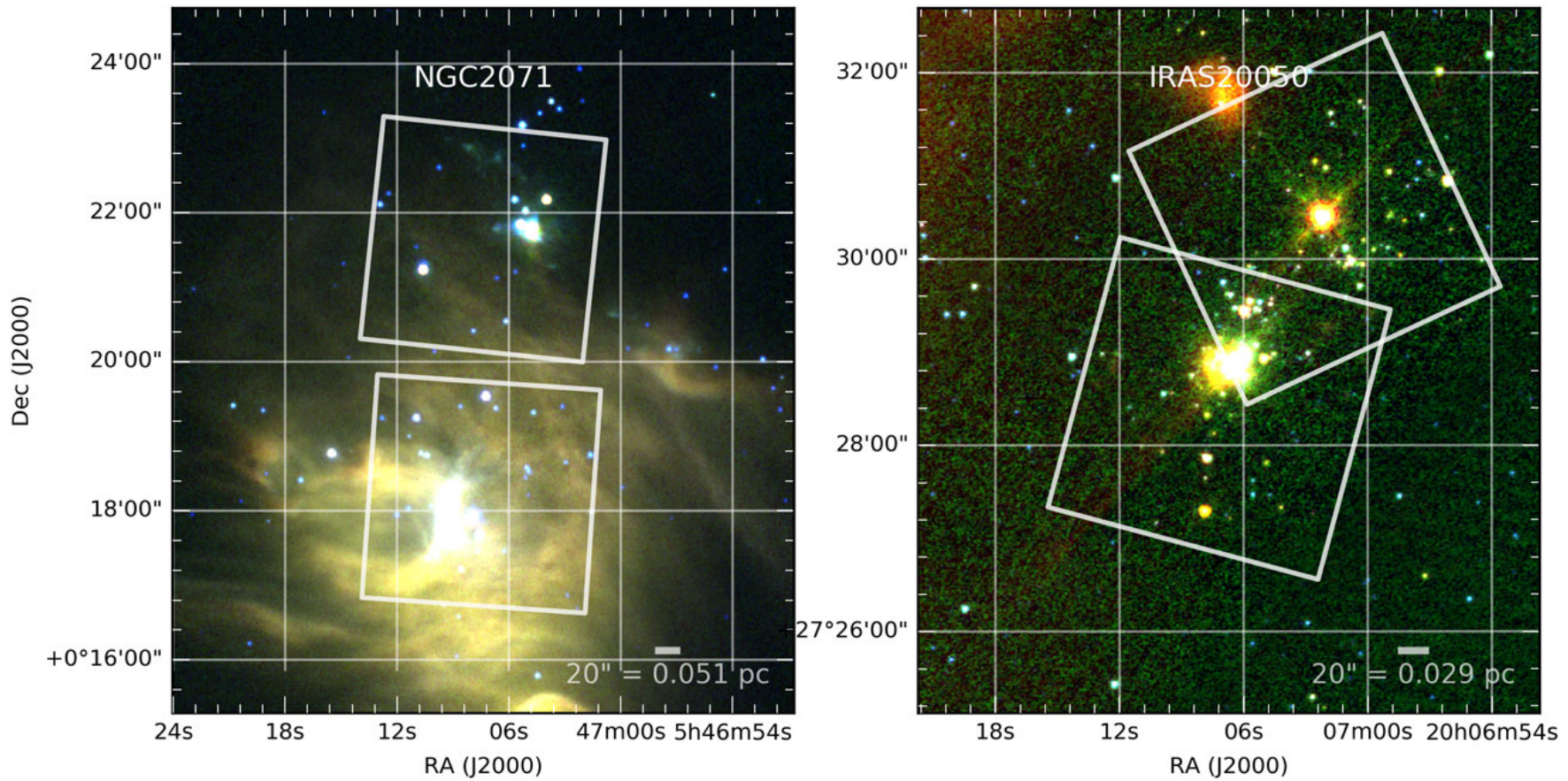


FIGURE II.16: IRAC 3-color images of NGC 2071 and IRAS 20050+2720.

## II.8.1 IRAS 20050+2720

### II.8.1.1 Context

IRAS 20050+2720 is part of an active site of intermediate-mass star formation in the Cygnus Rift located at 700 pc (Wilking et al., 1989), with the particularity that it doesn't seem to contain any massive stars (Günther et al., 2012). The main cluster core is associated with water and methanol masers (Palla et al., 1991; Fontani et al., 2010) and multipolar molecular outflows observed at millimeter wavelengths (Bachiller et al., 1995; Anglada et al., 1998; Beltrán et al., 2008), suggesting that the region might have experienced a recent episode of star formation in the past 0.1 Myr which contrasts with the average age of the cluster of 1 Myr (Chen et al., 1997; Gutermuth et al., 2005). Gutermuth et al., 2009 have identified  $> 170$  YSOs surrounding the core and measured their continuum fluxes up to  $8 \mu\text{m}$  with IRAC. While measurements at longer wavelengths were able to provide estimates of the total luminosity of the cluster (e.g. using IRAS, Molinari et al., 1996,  $388 L_\odot$ ), the measurements are confused in the densest region and it has not been possible to properly associate the far-IR emission with its short wavelength counterpart because of the small separation between IRAC-detected protostars. The IRAS point source was classified as a luminous class 0 protostar (Bachiller, 1996), and its emission associated with the bright millimeter source MMS1 to the northwest of the core (Chini et al., 2001). Beltrán et al. (2008) show strong evidence that this region has multiple generations of stars, and suggest that a group of low-mass stars first completed its main accretion phase, before setting the stage for the birth of new intermediate-mass stars at the core of this cluster.

### II.8.1.2 Observations and discussion

We have observed two fields within the cluster (see Fig. II.16), including the brightest core at  $20^h07^m06.70^s + 27^\circ28'54.5''$ . Multiple sources in the core can be distinguished in the IRAC maps, but the core appears extended in *Spitzer* MIPS at 24  $\mu\text{m}$ , and is identified as a single source with WISE. No high resolution far-infrared continuum data longward of 24  $\mu\text{m}$  was available for this source. To our knowledge, our observations are the only mid-IR observations available that can properly resolve the various components of the dense region.

TABLE II.19: Sources fluxes in IRAS 20050+2720.

SOFIA name	Coordinates J2000	ks	i1	i2	i3	i4	F11	F19	F31	F37
		Jy	Jy	Jy	Jy	Jy	Jy	Jy	Jy	Jy
IRAS20050.1	20h07m06.6s	0.214	0.489	0.57	0.731	0.858	0.64	1.93	4.50	6.32
	+27d28m48.0s	$\pm$ 0.021	$\pm$ 0.049	$\pm$ 0.057	$\pm$ 0.073	$\pm$ 0.086	$\pm$ 0.07	$\pm$ 0.20	$\pm$ 0.35	$\pm$ 0.59
IRAS20050.2	20h07m06.2s	0.002	0.041	0.142	0.264	0.308	0.06	1.45	9.31	11.96
	+27d28m49.1s	$\pm$ 0.002	$\pm$ 0.004	$\pm$ 0.014	$\pm$ 0.026	$\pm$ 0.031	$\pm$ 0.06	$\pm$ 0.19	$\pm$ 0.72	$\pm$ 1.19
IRAS20050.3	20h07m06.3s	0.028	0.09	0.218	0.339	0.429	0.18	2.58	12.53	19.34
	+27d28m56.6s	$\pm$ 0.003	$\pm$ 0.009	$\pm$ 0.022	$\pm$ 0.034	$\pm$ 0.043	$\pm$ 0.06	$\pm$ 0.27	$\pm$ 0.94	$\pm$ 1.41
IRAS20050.4	20h07m05.9s	0.002	0.023	0.039	0.053	0.055	0.06	0.25	8.54	12.85
	+27d28m59.2s	$\pm$ 0.002	$\pm$ 0.003	$\pm$ 0.004	$\pm$ 0.008	$\pm$ 0.008	$\pm$ 0.05	$\pm$ 0.20	$\pm$ 0.80	$\pm$ 1.25
IRAS20050.5	20h07m06.6s	0.042	0.118	0.176	0.235	0.32	0.19	1.03	2.97	5.65
	+27d28m53.1s	$\pm$ 0.004	$\pm$ 0.012	$\pm$ 0.018	$\pm$ 0.024	$\pm$ 0.032	$\pm$ 0.05	$\pm$ 0.21	$\pm$ 0.33	$\pm$ 0.65
IRAS20050.6	20h07m02.2s	0.155	0.537	0.771	1.113	1.805	1.81	2.29	1.64	1.22
	+27d30m26.0s	$\pm$ 0.016	$\pm$ 0.054	$\pm$ 0.077	$\pm$ 0.111	$\pm$ 0.181	$\pm$ 0.13	$\pm$ 0.17	$\pm$ 0.14	$\pm$ 0.38
IRAS20050.7	20h07m07.9s	0.002	0.004	0.024	0.06	0.072	0.06	0.11	1.15	2.09
	+27d27m15.8s	$\pm$ 0.002	$\pm$ 0.004	$\pm$ 0.002	$\pm$ 0.006	$\pm$ 0.007	$\pm$ 0.05	$\pm$ 0.06	$\pm$ 0.14	$\pm$ 0.31

We distinguish 5 sources which appear to share an envelope at 37  $\mu\text{m}$ . These sources are labeled in Fig. II.17, and their IRAC and FORCAST photometry is summarized in Table II.19. IRAS20050.4 is coincident with the source at the northwestern end of the

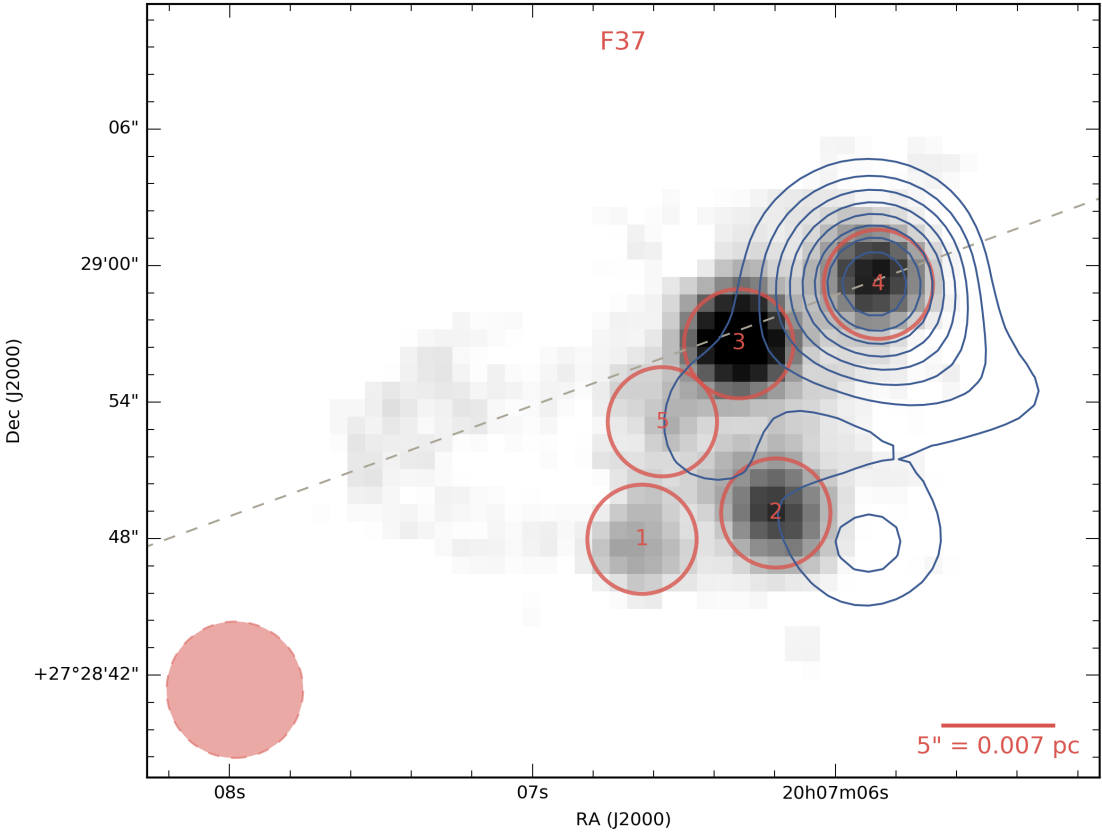


FIGURE II.17: 37  $\mu\text{m}$  observations of the IRAS 20050+2720 core, with the 5 identified objects. The blue contours are from a 2.7 mm continuum emission observed by the OVRO array (Beltrán et al., 2008) at levels from 10 to 46 mJy beam<sup>-1</sup> by increments of 4 mJy beam<sup>-1</sup>. The resolution of the 2.7 mm beam is  $\sim 4.8''$ , while the r.m.s noise is 1.5 mJy beam<sup>-1</sup>. The dashed line is the axis of a bipolar outflow identified by Bachiller et al. (1995). The beam shown at the bottom left represents the resolution of the FORCAST instrument.

region, which is named OVRO1 in Beltrán et al. (2008). Two more sources are identified with the blue contours from Beltrán et al. (2008), to the south and east of OVRO1, but they do not appear to correlate with our SOFIA sources. The outflow axis (Outflow "A", Bachiller et al., 1995) appears to be aligned with extended emission that is visible to the east of the 5 sources. This extended emission is visible in both IRAC and FORCAST, and coincides with CO velocity maps from Beltrán et al. (2008) showing blueshifted gas. The emission, totalling  $\sim 6$  Jy at  $37\text{ }\mu\text{m}$ , appears diffuse and not connected to any particular YSO: this requires a mechanism to keep the dust emitting at these wavelengths, since no viable heating source is available to heat this material at these distances (many thousands of au from the nearest YSO).

Since the emission appears associated with the outflow, one possible scenario is that the material was recently ejected from the central clump of YSOs by this powerful outflow. This could be material from the diffuse envelope which seem to surround the 5 sources, or material from one given YSO's gravitationally bound envelope. The gas and dust being ejected at high velocities (Bachiller et al., 1995), it might not yet have time to completely thermalize with the surrounding medium (at which point it would not emit at these wavelengths). This scenario could be confirmed with high sensitivity sub-millimeter maps of the region, with a focus on dense gas tracers that would follow the mass in these regions. The existing maps from Beltrán et al. (2008) do not have sufficient sensitivity or resolution to properly identify the velocity field from the gas associated with this continuum emission.

Another possible explanation for this emission is that the gas and dust ejected from the cluster is heated by colliding with cold material in the surrounding medium. This could explain the bullet-like shape of the emission, and makes sense given the very high

velocities from the outflow. The emission could arise from a supersonic shock layer that heats up the dust to a few hundreds of K, at which point its emission could become visible in the IRAC and SOFIA bands.

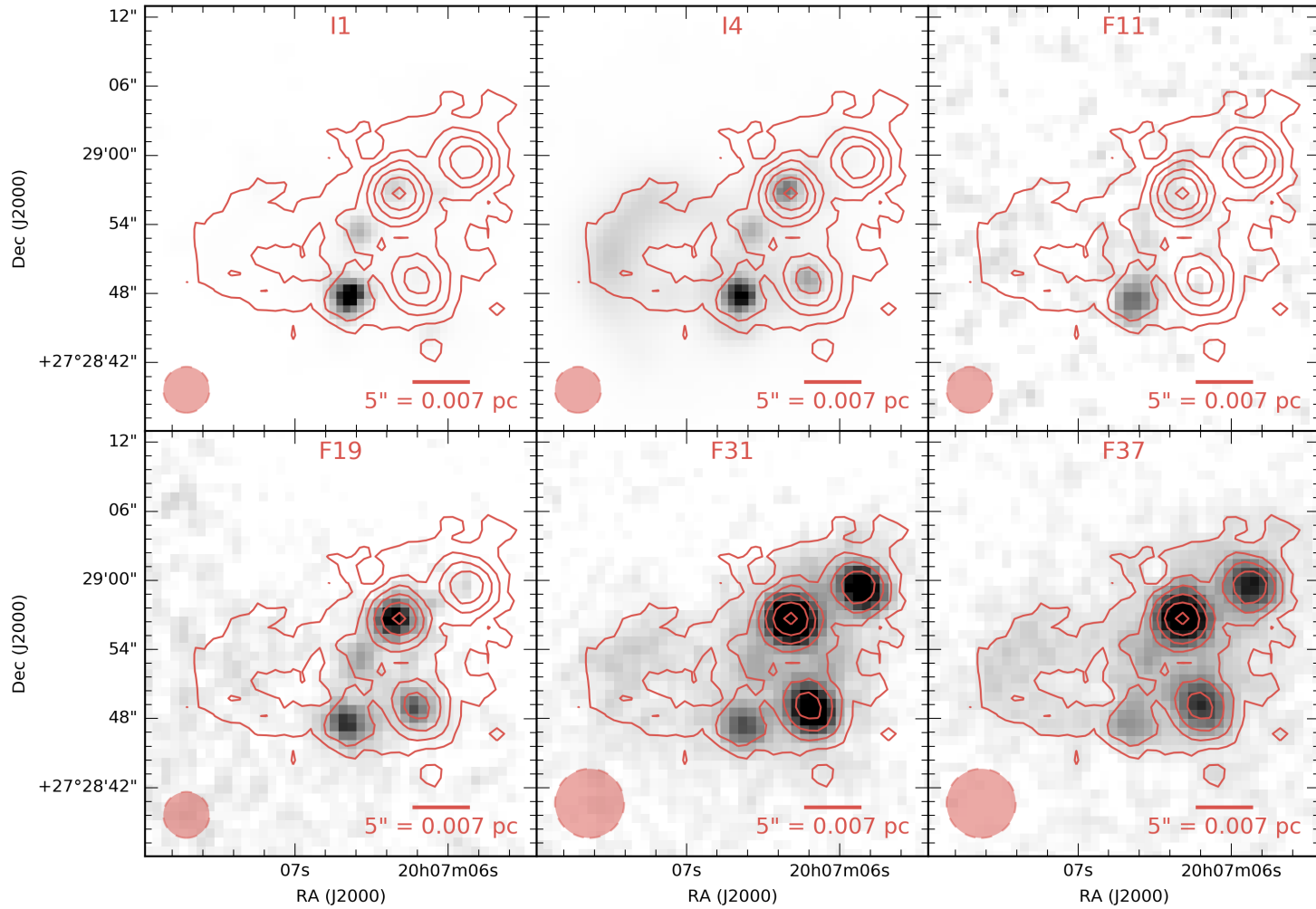


FIGURE II.18: The core of IRAS20050+2720 is seen in the four bands of the *Spitzer* IRAS instrument, as well as with the four FORCAST bands. The increased resolution of FORCAST compared to previous instruments allows to match the long-wavelength emission with its short wavelength counterpart. The stretch in each image is adjusted for optimal readability. The red contours correspond to the FORCAST 37  $\mu$ m emission at 0.03, 0.07, 0.13, 0.2, 0.3 and 0.4 Jy.

The 5 sources in the densest part of the cluster are all highly extincted based on the slopes of the emission in the 2MASS bands and the depth of the 10  $\mu\text{m}$  silicate absorption feature (see Fig. II.19). IRAS20050.1 has a flat spectrum out to 37  $\mu\text{m}$ , unlike the four other sources which are rising. IRAS20050.4 is the most steeply rising source, and is barely detected in the IRAC bands, suggesting that it is the most embedded source, which is corroborated by the fact that it is coincident with the strongest millimeter continuum source in the region.

In testing the various scenarios of star formation, it is useful to obtain a measure of how much mass is available for the YSOs to grow after their original collapse. For this, clustered regions such as this one are an ideal laboratory since the YSOs usually appear to share an envelope. In this cluster, the typical separation between the sources are 6''-8'', which correspond to projected distances of 3000-5600 au. This strongly indicates that the envelopes of individual YSOs are interacting with each other.

However, appropriately measuring the flux from each individual source in these clustered regions is challenging, since the sources are so close together. With an aperture of 2.4'' (3 pixel radius), we managed to put non-overlapping apertures for all the 5 sources in IRAS 20050+2720. but since the aperture correction was derived considering a "total flux" aperture to be  $\sim$ 12 pixel radius, we are accounting for the same flux multiple times, even if the apertures are not overlapping. If we estimate the 37  $\mu\text{m}$  flux from the eastern extended emission to be totalling  $\sim$  6 Jy, we obtain about 22% of excess 37  $\mu\text{m}$  flux when comparing the sum of the point sources and the total emission from the cluster (see Table II.21). At 31  $\mu\text{m}$ , the flux excess is only about 10%. At 19  $\mu\text{m}$  and below, the extended emission is within the noise uncertainty of the map.

This excess flux can only partially be explained by the tails of the PSF extending

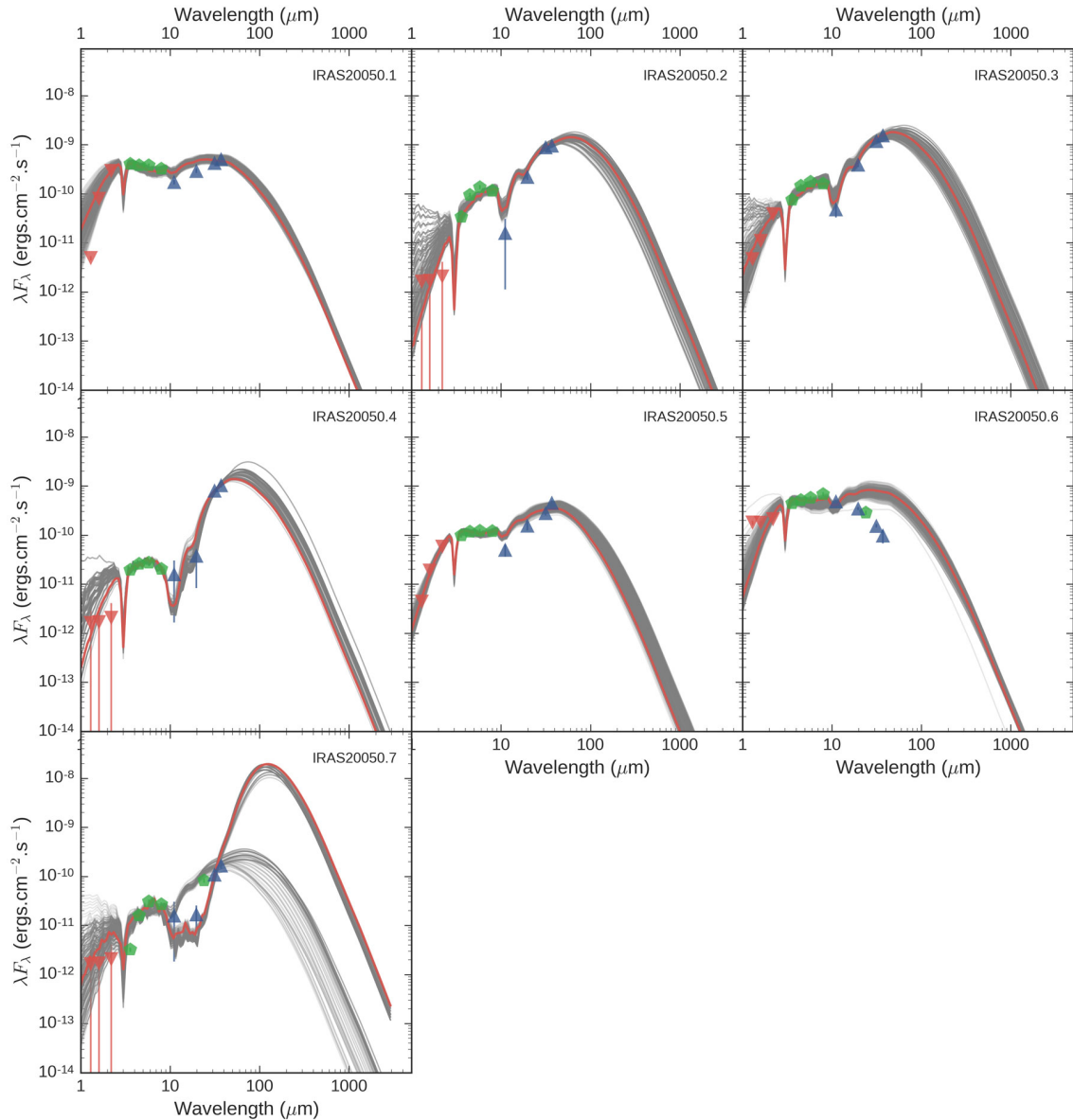


FIGURE II.19: SEDs of the 7 sources in the two fields.

well below the aperture size (see Fig. II.2), with 10-15% of the total energy still existing in the annulus outward of 8 pixels ( $6''$ ) from the aperture center. However, the contribution of a source to any given other source is only a fraction of this since it would only correspond to the amount of flux within a 3-pixel aperture. We conclude that the PSF shape is not responsible for the observed excess flux at both wavelengths.

One possible explanation would be that diffuse thermal emission occurs across the entire region. This could be caused by heating internal to the cluster (powered by the outflow, for example, like the eastern extended emission) or by a population of stochastically heated very small grains, which are not in LTE. The high outflow activity in this region could carve out multiple cavities which facilitate heating from the individual stars to extended over to larger distances within the envelopes and the shared mass reservoir. At  $37\text{ }\mu\text{m}$ , the level of diffuse emission required to account for the excess flux is about  $0.05\text{ Jy pixel}^{-1}$ , which is the same as the average diffuse emission in the eastern region. Such an explanation would also help account for the high amount of external extinction that is needed to fit most of the SEDs in this region.

This tends to favor a scenario where protostars are fragmenting from a cloud and continue accreting material within that original envelope. The envelopes of neighboring YSOs interact, and possibly can exchange material as some YSOs become more massive (competitive accretion).

The fitted parameters for the 7 identified sources are shown in Table II.23. Note that since no long-wavelength data is available, the envelope masses are not very well constrained. Sources 6 and 7 are far away from the main core which was discussed previously, and do not appear to be associated with the first 5 sources. The range of fitted parameters reveals some important diagnostics of these sources:

TABLE II.21: Clustered sources in the densest region of IRAS 20050+2720.

SOFIA name	F11 Jy	F19 Jy	F31 Jy	F37 Jy
IRAS20050.1	0.64	1.93	4.50	6.32
IRAS20050.2	0.06	1.45	9.31	11.96
IRAS20050.3	0.18	2.58	12.53	19.34
IRAS20050.4	0.06	0.25	8.54	12.85
IRAS20050.5	0.19	1.03	2.97	5.65
Sum of point sources in cluster	1.13	7.24	37.84	56.11
Total cluster emission	1.79	7.07	37.36	49.33
Ratio	1.58	0.98	0.99	0.88

TABLE II.23: Fitted parameters of sources in IRAS 20050+2720.

SOFIA Name	Coordinates J2000	$\alpha$	R	$M_{\text{env}}$ $M_{\odot}$	$L_{\text{mod}}$ $L_{\odot}$	$i$ °	$A_V$	s
IRAS20050.1	20h07m06.6s +27d28m48.0s	0.071	0.741	$0.004 \pm 0.001$	$108.8 \pm 22.1$	58	8	0.70
IRAS20050.2	20h07m06.2s +27d28m49.1s	1.649	0.772	$0.256 \pm 0.159$	$39.9 \pm 9.5$	19	14	0.70
IRAS20050.3	20h07m06.3s +27d28m56.6s	1.135	0.732	$0.114 \pm 0.051$	$48.5 \pm 9.8$	19	14	1.15
IRAS20050.4	20h07m05.9s +27d28m59.2s	1.712	0.266	$0.577 \pm 0.413$	$57.0 \pm 17.4$	38	3	1.00
IRAS20050.5	20h07m06.6s +27d28m53.1s	0.537	0.782	$0.010 \pm 0.004$	$43.7 \pm 7.2$	47	13	1.30
IRAS20050.6	20h07m02.2s +27d30m26.0s	-0.338	2.222	$0.004 \pm 0.002$	$134.4 \pm 28.2$	33	13	0.70
IRAS20050.7	20h07m07.9s +27d27m15.8s	1.294	1.415	$0.022 \pm 0.238$	$374.4 \pm 225.6$	19	14	1.30

- sources 1 and 5 appear to be at a later stage of their evolution, with a lower spectral index and much lower envelope mass;
- sources 2, 3 and 4 are more embedded, with steeply rising SOFIA fluxes. They are consistent with having sub-solar mass envelopes;
- source 6 fits less well and appears to have a very low envelope mass, as the SOFIA fluxes are steeply decreasing. Note that the 24  $\mu\text{m}$  MIPS data points are plotted, but not used in the fitting;
- source 7 appears to have two very different kinds of SEDs fitting the data points, as exhibited by the large error on the mass determination. More than all sources in this

region, this one would greatly benefit from having long-wavelength data points.

Our findings echo the work by Beltrán et al. (2008) who suggest that there are multiple generations of star formation coexisting in the same cluster. Source 2, 3 and 4 are newest generation of objects while 1 and 5 are already more evolved - but all 5 sources are still sharing that primordial envelope. This has implications on our understanding of clustered star formation and the natural life cycle of young stars. In this new paradigm, a first generation of low-mass stars would complete its main accretion phase before intermediate-mass stars can form.

## II.8.2 NGC 2071

### II.8.2.1 Context

The NGC 2071 star-forming region is one of several active areas of star formation in the northern part of L1630 giant molecular cloud which is located at a distance of 422 pc (Dishoeck et al., 2011). NGC 2071 itself is a reflection nebula. The NGC 2071 infrared cluster, located about 4' north of the reflection nebula, is a region of intermediate mass star formation (Strom et al., 1976; Persson et al., 1981; Butner et al., 1990). Maps of the cloud in CO and its isotopomers (Buckle et al., 2010) show a large scale clump with  $\sim 1000 M_{\odot}$  associated with the cluster. Dust continuum emission at  $\lambda=0.85$  and 1.3 mm peaks on center of the cluster extending 1' in diameter containing  $30 M_{\odot}$  of gas and dust (Johnstone et al., 2001; Mitchell et al., 2001; Launhardt et al., 1996). Emission from CS in the J=2-1 through J=7-6 indicate that the gas in this region is centrally condensed with a density of  $sim1 \times 10^6 \text{ cm}^{-3}$  (Zhou et al., 1990).

There are a number of near infrared surveys of the young cluster (e.g., Strom et al., 1976; Lada et al., 1991; Megeath et al., 2012; Spezzi et al., 2015). Spezzi et al. (2015)

identify 52 YSOs associated with the NGC 2071 cluster, with the majority Class II sources. Flaherty et al. (2008) estimate an age of  $\sim 2$  Myr for the cluster, consistent with the large fraction of Class II sources (Evans et al., 2009). The brightest far infrared emission from the cluster is associated with the IRS1 region (Harvey et al., 1979; Butner et al., 1990), which has an estimated total luminosity of  $520 L_{\odot}$ . The immediate region of IRS 1 is, in fact, home to a number of YSOs that are infrared, X-ray, and radio sources (Skinner et al., 2009; Carrasco-González et al., 2012; van Kempen et al., 2012). The radio (Carrasco-González et al., 2012) and H<sub>2</sub> emission line imaging indicate that IRS 1, IRS 2, IRS 3, and, perhaps, VLA 1 are YSOs with outflows. The larger scale molecular outflow associated with this region is well studied in a number of molecules (Bally, 1982; Chernin et al., 1993; Stojimirović et al., 2008).

Figure ?? shows the Spitzer 3.1  $\mu\text{m}$  image of the IRS 1 region on the left (image from Spitzer Archive: Megeath et al., 2012) and the Herschel 70  $\mu\text{m}$  image on the right (image from Herschel Archive: Gould Belt Project, P.I. André). The plus marks in both panels indicate the position of the brighter YSOs: IRS 1, IRS 2, IRS 3, IRS 4, and VLA 1. The inner red circle with a diameter of  $26''$  indicates the extend of the saturated region in the Spitzer MIPS 24  $\mu\text{m}$  image; the outer red circle, diameter  $60''$ , encompasses the region with strong imaging artifacts in the MIPS 24  $\mu\text{m}$  image. The right panel shows Herschel 70  $\mu\text{m}$  image which does not resolve the emission from IRS 1, IRS 2, IRS 3, and VLA 1. The centroid of the 24  $\mu\text{m}$  and 70  $\mu\text{m}$  emission is between IRS 1 and VLA 1 indicating that several of the sources are contributing to the total observed emission. Interferometric observations show that the millimeter wavelength dust emission is dominated by envelopes associated with IRS 1 and IRS 3, with estimated masses of  $8.2$  and  $12.3 M_{\odot}$  material, respectively (van Kempen et al., 2012). The millimeter emission also reveals the presence

of disks with radii  $\leq 100$  au associated with IRS 1 and IRS 3 (van Kempen et al., 2012).

The luminosities and masses of the individual source, IRS 1, IRS 2, IRS 3, and VLA 1, are not known. The Spectral Energy Distributions (SEDs) shortward of  $10 \mu\text{m}$  support their identification as embedded YSOS (Skinner et al., 2009). Skinner et al. (2009) gives a clear discussion of the possibilities for IRS 1 and concludes that it is likely a mid-to late B star. van Kempen et al., 2012 find luminosities of 10, 3.4, and  $\leq 27 L_\odot$  for IRS 1, 2, and 3, respectively, and stellar masses of  $\leq 1 M_\odot$  for each, based on SED fitting. These masses and luminosities are not consistent with estimate of the total luminosity of the region of  $520 L_\odot$  (Butner et al., 1990). The far infrared images from Herschel reveal that IRS 1 alone does not totally dominate, as seen in Fig. II.1; IRS 1, VLA 1, and IRS 3 likely make substantial contributions to the emission with lesser emission from IRS 2 and IRS 4.

### **II.8.2.2 Observations and discussion**

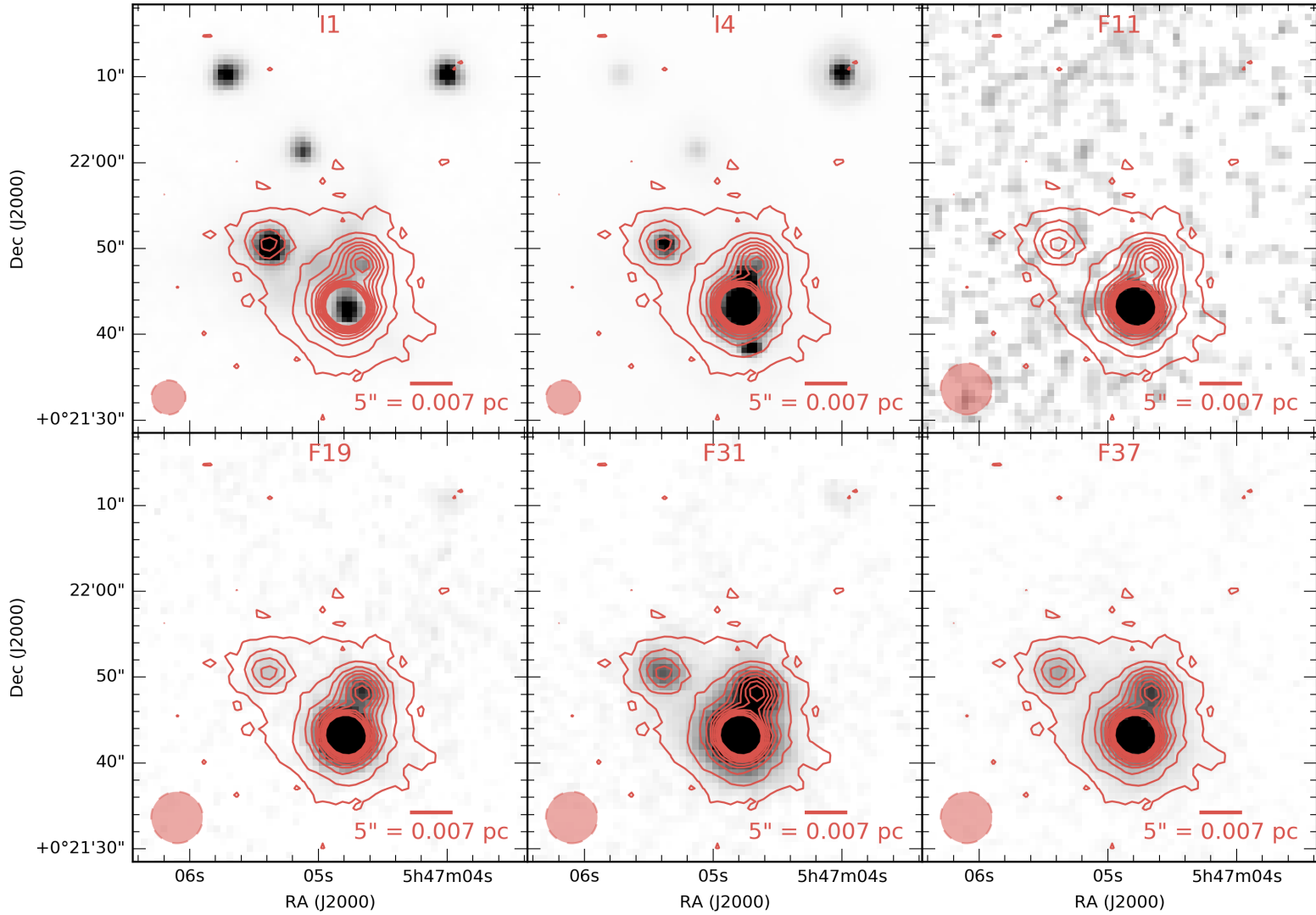


FIGURE II.20: The core of NGC2071 is seen in two bands of the *Spitzer* IRAC instrument ("I1" and "I4"), as well as with the four FORCAST bands. The increased resolution of FORCAST compared to previous instruments allows to match the long-wavelength emission with its short wavelength counterpart. The stretch in each image is adjusted for optimal readability.

The red contours correspond to the FORCAST 37  $\mu\text{m}$  emission, between 0.1 and 2.4 Jy by increment of 0.25 Jy.

TABLE II.25: Sources in the densest region of NGC2071.

SOFIA name	F11	F19	F31	F37
	Jy	Jy	Jy	Jy
NGC2071.1	10.07	72.041	167.93	234.93
NGC2071.2	0.38	11.207	56.70	89.55
NGC2071.3	0.19	3.027	19.97	37.56
Sum of point sources in cluster	10.65	86.28	244.61	362.03
Total cluster emission	13.523	94.16	280.14	362.99
Ratio	1.27	1.09	1.15	1.00

TABLE II.27: Fitted parameters of sources in NGC2071.

SOFIA Name	Coordinates J2000	$\alpha$	R	$M_{\text{env}}$	$L_{\text{mod}}$	$L_{\text{bol}}$	i	$A_V$	s
				$M_{\odot}$	$L_{\odot}$	$L_{\odot}$	$^{\circ}$	mag	
NGC2071.1	05h47m04.8s +00d21m43.1s	2.31	2.78	$22.17 \pm 2.418$	$49.4 \pm 4.5$	297.2	0.0	14	1.3
NGC2071.2	05h47m04.7s +00d21m48.2s	2.22	1.82	$6.57 \pm 1.712$	$331.2 \pm 35.8$	199.8	18.7	14	1.3
NGC2071.3	05h47m05.4s +00d21m50.3s	1.01	2.29	$4.38 \pm 1.125$	$374.4 \pm 48.7$	113.7	18.7	0	1.3
NGC2071.4	05h47m04.0s +00d22m10.5s	1.08	3.96	$14.78 \pm 5.234$	$9.2 \pm 2.1$	21.4	0.0	14	1.0
NGC2071.5	05h47m10.7s +00d21m14.0s	0.32	2.03	$0.015 \pm 0.007$	$22.1 \pm 6.2$	12.7	0.0	14	1.3

Show sum of sources compared to cluster total

## II.9 Conclusion and future work

We have used SOFIA FORCAST to image 42 fields in bright, nearby stellar clusters. We derive aperture photometry in 4 bands:  $11.1 \mu\text{m}$ ,  $19.7 \mu\text{m}$ ,  $31.5 \mu\text{m}$ ,  $37.1 \mu\text{m}$ , for a total of 90 sources. In many cases, our photometry is the only mid- to far-IR photometry available for these sources, since archival *Spitzer* observations were either saturated or confused.

In multiple cases, we complete our SOFIA photometry using *Spitzer* IRAC as well as *Herschel* data. When the catalogs cannot be found, we use the same photometry pipeline that we developed for SOFIA on the *Spitzer* and *Herschel* calibrated images.

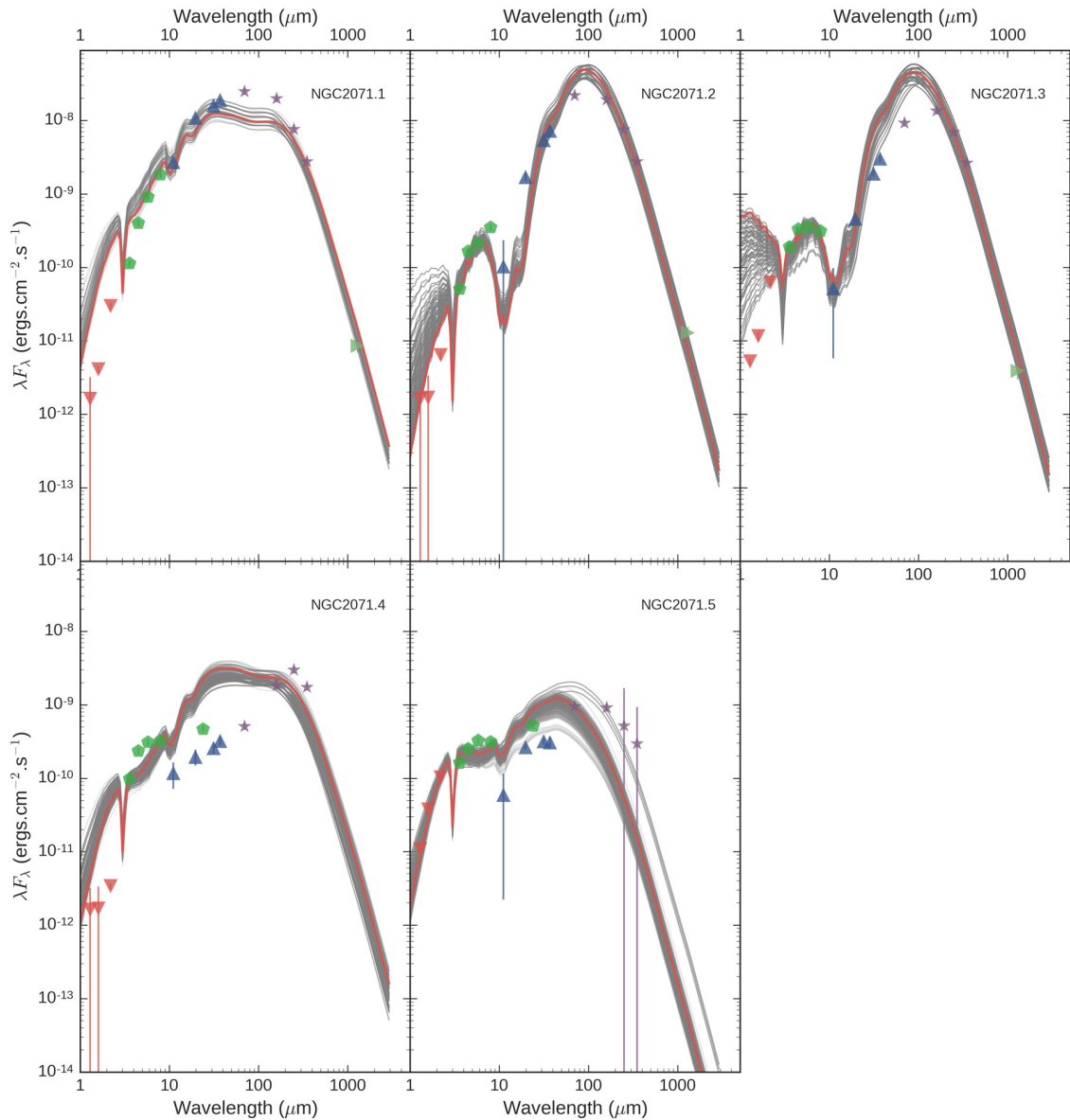


FIGURE II.21: SEDs of the 5 sources in the two fields.

We also proceed to SED fitting of our sources, based on a radiative transfer code called Hyperion. Using a simple grid, we produce estimates for physical parameters of these YSOs, and carefully approximate the error in the parameter estimate.

We take a closer look at two special clusters: IRAS 20050+2720, which contains five close-by YSOs sharing what appears to be an extended envelope, favoring a competitive accretion scenario; and NGC2071 [insert conclusions here]

In our sample there were 15 cases of extended emission at  $37\,\mu\text{m}$ . This spatial extension is not simple to model: with a FORCAST FWHM of  $\sim 3.5''$ , an object with spatial extension has a size on the order of a few thousands of au at 500 pc: we haven't been able to show that the central object can heat dust grains at this distance sufficiently for them to emit thermally at  $37\,\mu\text{m}$ . Hence, another heating mechanism is responsible for this emission: we suggest that the emission could be due to a population of non-LTE, very small dust grains. Answering this question will require further analysis and more study.

# Bibliography

- Allamandola, L J, A G G M Tielens, and J R Barker (1985). “Polycyclic aromatic hydrocarbons and the unidentified infrared emission bands - Auto exhaust along the Milky Way”. In: *Astrophysical Journal* 290, pp. L25–L28.
- Allen, Christine A et al. (2006). “Far infrared through millimeter backshort-under-grid arrays”. In: *Millimeter and Submillimeter Detectors and Instrumentation for Astronomy III*. Edited by Zmuidzinas 6275, 62750B–62750B–8.
- Allen, L et al. (2007). “The Structure and Evolution of Young Stellar Clusters”. In: *Protostars and Planets V*, p. 361.
- Anglada, Guillem et al. (1998). “On the Exciting Sources of the L723 and IRAS 20050+2720 Quadrupolar Molecular Outflows”. In: *Star Formation with the Infrared Space Observatory* 132, p. 303.
- Astropy Collaboration et al. (2013). “Astropy: A community Python package for astronomy”. In: A&A 558, A33, A33. DOI: 10.1051/0004-6361/201322068. arXiv: 1307.6212 [astro-ph.IM].
- Bachiller, R, A Fuente, and M Tafalla (1995). “An extremely high velocity multipolar outflow around IRAS 20050 + 2720”. In: *Astrophysical Journal* 445, pp. L51–L54.
- Bachiller, Rafael (1996). “Bipolar Molecular Outflows from Young Stars and Protostars”. In: *Annual Review of Astronomy and Astrophysics* 34.1, pp. 111–154.

- Bally, J. (1982). “Energetic activity in a star-forming molecular cloud core - A disk constrained bipolar outflow in NGC 2071”. In: *ApJ* 261, pp. 558–568. DOI: [10.1086/160366](https://doi.org/10.1086/160366).
- Beltrán, M T et al. (2008). “On the nature of outflows in intermediate-mass protostars: a case study of IRAS 20050+2720”. In: *Astronomy and Astrophysics* 481.1, pp. 93–105.
- Benford, Dominic J (2008). “Transition Edge Sensor Bolometers for CMB Polarimetry”. In: *Workshop on Technology Development for a CMB Probe of Inflation*.
- Bevington, Philip Raymond and D Keith Robinson (2003). *Data Reduction and Error Analysis for the Physical Sciences*. McGraw-Hill.
- Blind, N et al. (2011). “Optimized fringe sensors for the VLTI next generation instruments”. In: *Astronomy and Astrophysics* 530, p. 121.
- Bonnell, I A et al. (1997). “Accretion and the stellar mass spectrum in small clusters”. In: *Monthly Notices of the Royal Astronomical Society* 285, p. 201.
- Bonnell, Ian A and Matthew R Bate (2002). “Accretion in stellar clusters and the collisional formation of massive stars”. In: *Monthly Notice of the Royal Astronomical Society* 336.2, pp. 659–669.
- (2006). “Star formation through gravitational collapse and competitive accretion”. In: *Monthly Notices of the Royal Astronomical Society* 370.1, pp. 488–494.
- Bracco, A et al. (2011). “Herschel-ATLAS: statistical properties of Galactic cirrus in the GAMA-9 Hour Science Demonstration Phase Field”. In: *Monthly Notices of the Royal Astronomical Society* 412.2, pp. 1151–1161.
- Buckle, J. V. et al. (2010). “The JCMT Legacy Survey of the Gould Belt: a first look at Orion B with HARP”. In: *MNRAS* 401, pp. 204–222. DOI: [10.1111/j.1365-2966.2009.15619.x](https://doi.org/10.1111/j.1365-2966.2009.15619.x). arXiv: [0908.4162](https://arxiv.org/abs/0908.4162).

- Butner, H. M. et al. (1990). “High-resolution, far-infrared observations of NGC 2071”. In: *ApJ* 364, pp. 164–172. DOI: [10.1086/169398](https://doi.org/10.1086/169398).
- Cardelli, Jason A, Geoffrey C Clayton, and John S Mathis (1989). “The relationship between infrared, optical, and ultraviolet extinction”. In: *Astrophysical Journal* 345, pp. 245–256.
- Carrasco-González, C. et al. (2012). “Multiplicity, Disks, and Jets in the NGC 2071 Star-forming Region”. In: *ApJ* 746, 71, p. 71. DOI: [10.1088/0004-637X/746/1/71](https://doi.org/10.1088/0004-637X/746/1/71). arXiv: [1111.5469](https://arxiv.org/abs/1111.5469).
- Cayley, Arthur (1963). *The Collected Mathematical Papers of Arthur Cayley*.
- Chen, H et al. (1997). “IRAS 20050+2720: An Embedded Young Cluster Associated with a Multipolar Outflow”. In: *The Astrophysical Journal* 475.1, pp. 163–172.
- Chernin, L. and C. Masson (1993). “Observations of SO and SiO in the outflow from NGC 2071”. In: *ApJ* 403, pp. L21–L24. DOI: [10.1086/186712](https://doi.org/10.1086/186712).
- Chini, R et al. (2001). “Mm/Submm images of Herbig-Haro energy sources and candidate protostars”. In: *Astronomy and Astrophysics* 369.1, pp. 155–169.
- Clauset, Aaron, Cosma Rohilla Shalizi, and M E J Newman (2007). “Power-law distributions in empirical data”. In: *arXiv.org* 4, pp. 661–703. arXiv: [0706.1062v2 \[physics.data-an\]](https://arxiv.org/abs/0706.1062v2).
- Crassidis, John L and John L Junkins (2011). *Optimal Estimation of Dynamic Systems, Second Edition*. CRC Press.
- Davis, Sumner P, Mark C Abrams, and James W Brault (2001). “Fourier transform spectrometry”. In: *Fourier transform spectrometry by Sumner P. Davis et al. San Diego*.
- De Buizer, James M et al. (2012). “First Science Observations with SOFIA/FORCAST: 6-37 μm Imaging of Orion BN/KL”. In: *The Astrophysical Journal Letters* 749.2, p. L23.

- Di Francesco, J et al. (2007). “An Observational Perspective of Low-Mass Dense Cores I: Internal Physical and Chemical Properties”. In: *Protostars and Planets V*, pp. 17–32.
- Dishoeck, E F van et al. (2011). “Water in Star-forming Regions with the Herschel Space Observatory (WISH). I. Overview of Key Program and First Results”. In: *Publications of the Astronomical Society of Pacific* 123.9, pp. 138–170.
- Dunham, Michael M et al. (2010). “Evolutionary Signatures in the Formation of Low-Mass Protostars. II. Toward Reconciling Models and Observations”. In: *The Astrophysical Journal* 710.1, pp. 470–502.
- El Badaoui, Noad et al. (2014). “Towards a solid-state ring laser gyroscope”. In: *Comptes Rendus Physique* 15.10, pp. 841–850.
- Elias, Nicholas M et al. (2007). “The Mathematics of Double-Fourier Interferometers”. In: *The Astrophysical Journal* 657.2, pp. 1178–1200.
- Enoch, Melissa L et al. (2009). “Properties of the Youngest Protostars in Perseus, Serpens, and Ophiuchus”. In: *The Astrophysical Journal* 692.2, pp. 973–997.
- Evans II, N. J. et al. (2009). “The Spitzer c2d Legacy Results: Star-Formation Rates and Efficiencies; Evolution and Lifetimes”. In: ApJS 181, 321, pp. 321–350. DOI: 10.1088/0067-0049/181/2/321. arXiv: 0811.1059.
- Evans, Neal J et al. (2009). “The Spitzer c2d Legacy Results: Star-Formation Rates and Efficiencies; Evolution and Lifetimes”. In: *The Astrophysical Journal Supplement* 181.2, pp. 321–350.
- Ferrière, Katia M (2001). “The interstellar environment of our galaxy”. In: *Reviews of Modern Physics* 73.4, pp. 1031–1066.

- Fischer, William J et al. (2012). “Multiwavelength Observations of V2775 Ori, an Outbursting Protostar in L 1641: Exploring the Edge of the FU Orionis Regime”. In: *The Astrophysical Journal* 756.1, p. 99.
- Fixsen, D J and Eli Dwek (2002). “The Zodiacal Emission Spectrum as Determined by COBE and Its Implications”. In: *The Astrophysical Journal* 578.2, pp. 1009–1014.
- Fixsen, D J and J C Mather (2002). “The Spectral Results of the Far-Infrared Absolute Spectrophotometer Instrument on COBE”. In: *The Astrophysical Journal* 581.2, pp. 817–822.
- Fixsen, D J et al. (1996a). “A Balloon-borne Millimeter-Wave Telescope for Cosmic Microwave Background Anisotropy Measurements”. In: *Astrophysical Journal* v.470 470, p. 63.
- Fixsen, D J et al. (1996b). “The Cosmic Microwave Background Spectrum from the Full COBE FIRAS Data Set”. In: *Astrophysical Journal* v.473 473.2, pp. 576–587.
- Fixsen, D J et al. (1998). “The Spectrum of the Extragalactic Far-Infrared Background from the COBE FIRAS Observations”. In: *The Astrophysical Journal* 508.1, pp. 123–128.
- Flaherty, K. M. and J. Muzerolle (2008). “Evidence for Early Circumstellar Disk Evolution in NGC 2068/71”. In: AJ 135, pp. 966–983. DOI: 10.1088/0004-6256/135/3/966. arXiv: 0712.1601.
- Fontani, F, R Cesaroni, and R S Furuya (2010). “Class I and Class II methanol masers in high-mass star-forming regions”. In: *Astronomy and Astrophysics* 517, A56.
- Forman, Michael L, W Howard Steel, and George A Vanasse (1966). “Correction of Asymmetric Interferograms Obtained in Fourier Spectroscopy”. In: *Journal of the Optical Society of America* 56, p. 59.

- Furlan, E et al. (2016). “The Herschel Orion Protostar Survey: Spectral Energy Distributions and Fits Using a Grid of Protostellar Models”. In: *The Astrophysical Journal Supplement Series* 224.1, p. 5.
- Gillett, F C, W J Forrest, and K M Merrill (1973). “8 - 13-micron spectra of NGC 7027, BD +30 3639, and NGC 6572.” In: *Astrophysical Journal* 183, pp. 87–93.
- Grainger, William F et al. (2012). “Demonstration of spectral and spatial interferometry at THz frequencies”. In: *Applied Optics* 51.12, pp. 2202–2211.
- Griffiths, Peter R and James A De Haseth (2007). *Fourier Transform Infrared Spectrometry*. John Wiley & Sons.
- Günther, H M et al. (2012). “IRAS 20050+2720: Anatomy of a Young Stellar Cluster”. In: *The Astronomical Journal* 144.4, p. 101.
- Gutermuth, R A et al. (2009). “A Spitzer Survey of Young Stellar Clusters Within One Kiloparsec of the Sun: Cluster Core Extraction and Basic Structural Analysis”. In: *The Astrophysical Journal Supplement* 184.1, pp. 18–83.
- Gutermuth, R A et al. (2011). “A Correlation between Surface Densities of Young Stellar Objects and Gas in Eight Nearby Molecular Clouds”. In: *The Astrophysical Journal* 739.2, p. 84.
- Gutermuth, Robert A et al. (2005). “The Initial Configuration of Young Stellar Clusters: A K-Band Number Counts Analysis of the Surface Density of Stars”. In: *The Astrophysical Journal* 632.1, pp. 397–420.
- Harman, Richard R (2005). *Wilkinson Microwave Anisotropy Probe (WMAP) Attitude Estimation Filter Comparison*.
- Harries, J E (1980). “Atmospheric radiometry at submillimeter wavelengths”. In: *Applied Optics* 19.18, p. 3075.

- Harvey, P. M. et al. (1979). “Infrared observations of NGC 2071/IRS/ and AFGL 490 - Two low-luminosity young stars”. In: *ApJ* 229, pp. 990–993. DOI: [10.1086/157033](https://doi.org/10.1086/157033).
- Harvey, Paul M et al. (2012). “First Science Results from SOFIA/FORCAST: Super-resolution Imaging of the S140 Cluster at 37  $\mu$ m”. In: *The Astrophysical Journal Letters* 749.2, p. L20.
- Harwit, Martin, David Leisawitz, and Stephen Rinehart (2006). “A far-infrared/submillimeter kilometer-baseline interferometer in space”. In: *New Astronomy Reviews* 50.1-3, pp. 228–234.
- Helmich, Frank P and R J Ivison (2009). “FIRI—A far-infrared interferometer”. In: *Experimental Astronomy* 23.1, pp. 245–276.
- Herter, T L et al. (2012). “First Science Observations with SOFIA/FORCAST: The FORCAST Mid-infrared Camera”. In: *The Astrophysical Journal Letters* 749.2, p. L18.
- Herter, T L et al. (2013). “Data Reduction and Early Science Calibration for FORCAST, A Mid-Infrared Camera for SOFIA”. In: *Publications of the Astronomical Society of the Pacific* 125.933, pp. 1393–1404.
- Johnstone, D. et al. (2001). “Large Area Mapping at 850 Microns. III. Analysis of the Clump Distribution in the Orion B Molecular Cloud”. In: *ApJ* 559, pp. 307–317. DOI: [10.1086/322323](https://doi.org/10.1086/322323).
- Kalman, R E (1960). “A New Approach to Linear Filtering and Prediction Problems”. In: *Journal of Basic Engineering* 82.1, pp. 35–45.
- Kato, Eri et al. (2010). “Far-Infrared Interferometric Telescope Experiment : I. Interferometer Optics”. In: *Transactions of Space Technology Japan* 7.ists26, pp. 47–53.

- Kempen, T A van et al. (2009). “The nature of the Class I population in Ophiuchus as revealed through gas and dust mapping”. In: *Astronomy and Astrophysics* 498.1, pp. 167–194.
- Kempen, T A van et al. (2012). “The Small-scale Physical Structure and Fragmentation Difference of Two Embedded Intermediate-mass Protostars in Orion”. In: *The Astrophysical Journal* 751.2, p. 137.
- Kennicutt, R. C. and N. J. Evans (2012). “Star Formation in the Milky Way and Nearby Galaxies”. In: *ARA&A* 50, pp. 531–608. doi: [10.1146/annurev-astro-081811-125610](https://doi.org/10.1146/annurev-astro-081811-125610). arXiv: [1204.3552](https://arxiv.org/abs/1204.3552).
- Kennicutt, Robert C and Neal J Evans (2012). “Star Formation in the Milky Way and Nearby Galaxies”. In: *Annual Review of Astronomy and Astrophysics* 50.1, pp. 531–608.
- Kessler, M F et al. (1996). “The Infrared Space Observatory (ISO) mission.” In: *Astronomy and Astrophysics* 315, pp. L27–L31.
- Kim, Sang-Hee, P G Martin, and Paul D Hendry (1994). “The size distribution of interstellar dust particles as determined from extinction”. In: *Astrophysical Journal* 422, pp. 164–175.
- Korte, Piet A J de et al. (2003). “Time-division superconducting quantum interference device multiplexer for transition-edge sensors”. In: *Review of Scientific Instruments* 687.8, pp. 3807–3815.
- Lada, Charles J and Elizabeth A Lada (2003). “Embedded Clusters in Molecular Clouds”. In: *Annual Review of Astronomy & Astrophysics* 41.1, pp. 57–115.
- Lada, E. A. et al. (1991). “A 2.2 micron survey in the L1630 molecular cloud”. In: *ApJ* 371, pp. 171–182. doi: [10.1086/169881](https://doi.org/10.1086/169881).

- Larson, R B (1994). "The Evolution of Molecular Clouds". In: *The Structure and Content of Molecular Clouds* 439. Chapter 2, pp. 13–28.
- Launhardt, R. et al. (1996). "Dust emission from star-forming regions. IV. Dense cores in the Orion B molecular cloud." In: A&A 312, pp. 569–584.
- Lawson, Peter R (2000). "Principles of Long Baseline Stellar Interferometry". In: *Principles of Long Baseline Stellar Interferometry. Course notes from the 1999 Michelson Summer School*.
- Lefferts, E J, F L Markley, and M D Shuster (1982). "Kalman Filtering for Spacecraft Attitude Estimation". In: *Journal of Guidance* 5.5, pp. 417–429.
- Leisawitz, David et al. (2007). "The space infrared interferometric telescope (SPIRIT): High-resolution imaging and spectroscopy in the far-infrared". In: *Advances in Space Research* 40.5, pp. 689–703.
- Leisawitz, David et al. (2012). "Developing wide-field spatio-spectral interferometry for far-infrared space applications". In: *Optical and Infrared Interferometry III. Proceedings of the SPIE*. Ed. by Françoise Delplancke, Jayadev K Rajagopal, and Fabien Malbet. NASA Goddard Space Flight Ctr. (United States). SPIE, 84450A.
- Li, Aigen and B T Draine (2001). "Infrared Emission from Interstellar Dust. II. The Diffuse Interstellar Medium". In: *The Astrophysical Journal* 554.2, pp. 778–802.
- Mariotti, J-M and S T Ridgway (1988). "Double Fourier spatio-spectral interferometry - Combining high spectral and high spatial resolution in the near infrared". In: *Astronomy and Astrophysics (ISSN 0004-6361)* 195, p. 350.
- Markley, F Landis and John L Crassidis (2014). *Fundamentals of Spacecraft Attitude Determination and Control*. New York, NY: Springer.

- Mathis, J S, W Rumpl, and K H Nordsieck (1977). “The size distribution of interstellar grains”. In: *Astrophysical Journal* 217, pp. 425–433.
- Mathis, John S (1990). “Interstellar dust and extinction”. In: *IN: Annual review of astronomy and astrophysics. Vol. 28 (A91-28201 10-90)*. Palo Alto 28.1, pp. 37–70.
- Matsumoto, T, S Matsuura, and M Noda (1994). “2.4 micrometer sky brightness at balloon altitude”. In: *Astronomical Society of the Pacific* 106, p. 1217.
- Maybeck, Peter S (1982). *Stochastic Models, Estimation, and Control*. Academic Press.
- McKee, Christopher F and Eve C Ostriker (2007). “Theory of Star Formation”. In: *Annual Review of Astronomy and Astrophysics* 45.1, pp. 565–687.
- McKee, Christopher F and Jonathan C Tan (2003). “The Formation of Massive Stars from Turbulent Cores”. In: *The Astrophysical Journal* 585.2, pp. 850–871.
- Megeath, S T et al. (2012). “The Spitzer Space Telescope Survey of the Orion A and B Molecular Clouds. I. A Census of Dusty Young Stellar Objects and a Study of Their Mid-infrared Variability”. In: *The Astronomical Journal* 144.6, p. 192.
- Megeath, S. T. et al. (2012). “The Spitzer Space Telescope Survey of the Orion A and B Molecular Clouds. I. A Census of Dusty Young Stellar Objects and a Study of Their Mid-infrared Variability”. In: AJ 144, 192, p. 192. DOI: 10.1088/0004-6256/144/6/192.  
arXiv: 1209.3826.
- Mendillo, Christopher B et al. (2012). “Flight demonstration of a milliarcsecond pointing system for direct exoplanet imaging”. In: *Applied Optics* 51.29, p. 7069.
- Meynart, Roland (1992). “Sampling jitter in Fourier-transform spectrometers - Spectral broadening and noise effects”. In: *Applied Optics (ISSN 0003-6935)* 31.30, p. 6383.
- Michelson, Albert A and Edward W Morley (1887). “On the Relative Motion of the Earth and of the Luminiferous Ether”. In: *Sidereal Messenger* 6, pp. 306–310.

- Mighell, Kenneth J (2005). “Stellar photometry and astrometry with discrete point spread functions”. In: *Monthly Notices of the Royal Astronomical Society* 361.3, pp. 861–878.
- Mitchell, G. F. et al. (2001). “A Submillimeter Dust and Gas Study of the Orion B Molecular Cloud”. In: *ApJ* 556, pp. 215–229. DOI: [10.1086/321574](https://doi.org/10.1086/321574).
- Molinari, S et al. (1996). “A search for precursors of ultracompact HII regions in a sample of luminous IRAS sources. I. Association with ammonia cores.” In: *Astronomy and Astrophysics* 308, pp. 573–587.
- Murakami, H et al. (2007). “The Infrared Astronomical Mission AKARI”. In: *Publications of the Astronomical Society of Japan* 59.sp2, 369–S376.
- Myers, P C and E F Ladd (1993). “Bolometric temperatures of young stellar objects”. In: *Astrophysical Journal* 413, pp. L47–L50.
- Myers, Philip C (2011). “Star Formation in Dense Clusters”. In: *The Astrophysical Journal* 743.1, p. 98.
- Neugebauer, G et al. (1984). “The Infrared Astronomical Satellite (IRAS) mission”. In: *Astrophysical Journal* 278, pp. L1–L6.
- Offner, Stella S R and Christopher F McKee (2011). “The Protostellar Luminosity Function”. In: *The Astrophysical Journal* 736.1, p. 53.
- Ossenkopf, V and Th Henning (1994). “Dust opacities for protostellar cores”. In: *Astronomy and Astrophysics (ISSN 0004-6361)* 291, pp. 943–959.
- Oxley, Paul et al. (2004). “The EBEX experiment”. In: *Infrared Spaceborne Remote Sensing XII. Edited by Strojnik* 5543, pp. 320–331.
- Palla, F et al. (1991). “Water masers associated with dense molecular clouds and ultracompact H II regions”. In: *Astronomy and Astrophysics (ISSN 0004-6361)* 246, pp. 249–263.

- Peltier, JCA (1834). *Investigation of the heat developed by electric currents in homogeneous materials and at the junction of two different conductors.* Ann. Chim. Phys.
- Persson, S. E. et al. (1981). "High Velocity h<sub>2</sub> Line Emission in the NGC2071 Region". In: ApJ 251, p. L85. DOI: 10.1086/183699.
- Pilbratt, G L et al. (2010). "Herschel Space Observatory. An ESA facility for far-infrared and submillimetre astronomy". In: *Astronomy and Astrophysics* 518, p. L1.
- Porras, Alicia et al. (2003). "A Catalog of Young Stellar Groups and Clusters within 1 Kiloparsec of the Sun". In: *The Astronomical Journal* 126.4, pp. 1916–1924.
- Press, William H et al. (1992). "Numerical recipes in C. The art of scientific computing". In: *Cambridge: University Press*.
- Richards, M A (2003). "Coherent integration loss due to white gaussian phase noise". In: *IEEE Signal Processing Letters* 10.7, pp. 208–210.
- Rinehart, S A et al. (2014). "The Balloon Experimental Twin Telescope for Infrared Interferometry (BETTII): An Experiment for High Angular Resolution in the Far-Infrared". In: *Publications of the Astronomical Society of the Pacific* 126, pp. 660–673.
- Rizzo, Maxime J et al. (2012). "Tracking near-infrared fringes on BETTII: a balloon-borne, 8m-baseline interferometer". In: *Optical and Infrared Interferometry III. Proceedings of the SPIE* 8445, 84451T.
- Rizzo, Maxime J et al. (2014). "Building an interferometer at the edge of space: pointing and phase control system for BETTII". In: *Proceedings of the SPIE*. Ed. by Jacobus M Oschmann et al. Univ. of Maryland, College Park (United States). SPIE, 91433H–91433H–12.

- Rizzo, Maxime J et al. (2015). “Far-Infrared Double-Fourier Interferometers and their Spectral Sensitivity”. In: *Publications of the Astronomical Society of Pacific* 127.9, pp. 1045–1060.
- Robitaille, T P (2011). “HYPERION: an open-source parallelized three-dimensional dust continuum radiative transfer code”. In: *Astronomy and Astrophysics* 536, A79.
- Robitaille, Thomas P et al. (2006). “Interpreting Spectral Energy Distributions from Young Stellar Objects. I. A Grid of 200,000 YSO Model SEDs”. In: *The Astrophysical Journal Supplement Series* 167.2, pp. 256–285.
- Robitaille, Thomas P et al. (2007). “Interpreting Spectral Energy Distributions from Young Stellar Objects. II. Fitting Observed SEDs Using a Large Grid of Precomputed Models”. In: *The Astrophysical Journal Supplement Series* 169.2, pp. 328–352.
- Schmidt, J and H Niemann (2001). “Using Quaternions for Parametrizing 3-D Rotations in Unconstrained Nonlinear Optimization.” In: *VMV*.
- Sellgren, K (1994). “Tiny Grains, Large Molecules, and the Infrared Cirrus”. In: *The First Symposium on the Infrared Cirrus and Diffuse Interstellar Clouds. ASP Conference Series* 58, pp. 243–.
- Shimizu, T Taro et al. (2016). “Herschel far-infrared photometry of the Swift Burst Alert Telescope active galactic nuclei sample of the local universe - II. SPIRE observations”. In: *Monthly Notices of the Royal Astronomical Society* 456.3, pp. 3335–3353.
- Shirley, Yancy L et al. (2000). “Tracing the Mass during Low-Mass Star Formation. I. Submillimeter Continuum Observations”. In: *The Astrophysical Journal Supplement Series* 131.1, pp. 249–271.
- Shu, F H (1977). “Self-similar collapse of isothermal spheres and star formation”. In: *Astrophysical Journal* 214, pp. 488–497.

- Shuster, Malcolm D (1993). “Survey of attitude representations”. In: *Journal of the Astronautical Sciences (ISSN 0021-9142)* 41, pp. 439–517.
- Skinner, S. L. et al. (2009). “Chandra and Spitzer Imaging of the Infrared Cluster in NGC 2071”. In: ApJ 701, pp. 710–724. DOI: 10.1088/0004-637X/701/1/710. arXiv: 0906.2428 [astro-ph.SR].
- Spezzi, L. et al. (2015). “The VISTA Orion mini-survey: star formation in the Lynds 1630 North cloud”. In: *ArXiv e-prints*. arXiv: 1505.04631 [astro-ph.SR].
- Sromovsky, Lawrence A (2003). “Radiometric Errors in Complex Fourier Transform Spectrometry”. In: *Applied Optics OT* 42.10, p. 1779.
- Staguhn, Johannes et al. (2014a). “Design and Expected Performance of GISMO-2, a Two Color Millimeter Camera for the IRAM 30 m Telescope”. In: *Journal of Low Temperature Physics* 176.5, pp. 829–834.
- Staguhn, Johannes G et al. (2014b). “The GISMO Two-millimeter Deep Field in GOODS-N”. In: *The Astrophysical Journal* 790.1, p. 77.
- Stecher, T P and B Donn (1965). “On Graphite and Interstellar Extinction”. In: *Astrophysical Journal* 142, pp. 1681–.
- Stojimirović, I., R. L. Snell, and G. Narayanan (2008). “Multiple Parsec-Scale Outflows in the NGC 2071 Cluster”. In: ApJ 679, pp. 557–569. DOI: 10.1086/586688.
- Strom, K. M., S. E. Strom, and F. J. Vrba (1976). “Infrared surveys of dark-cloud complexes. I. The Lynds 1630 dark cloud.” In: AJ 81, pp. 308–313. DOI: 10.1086/111888.
- Tan, J C et al. (2014). “Massive Star Formation”. In: *Protostars and Planets VI*, pp. 149–172.
- Terebey, S, F H Shu, and P Cassen (1984). “The collapse of the cores of slowly rotating isothermal clouds”. In: *Astrophysical Journal* 286, pp. 529–551.

- Thompson, A Richard, James M Moran, and Jr George W Swenson (2008). *Interferometry and Synthesis in Radio Astronomy*. John Wiley & Sons.
- Trawny, N and S I Roumeliotis (2005). “Indirect Kalman filter for 3D attitude estimation”. In:
- In:
- Ulrich, R K (1976). “An infall model for the T Tauri phenomenon”. In: *Astrophysical Journal* 210, pp. 377–391.
- van Kempen, T. A. et al. (2012). “The Small-scale Physical Structure and Fragmentation Difference of Two Embedded Intermediate-mass Protostars in Orion”. In: ApJ 751, 137, p. 137. DOI: 10.1088/0004-637X/751/2/137. arXiv: 1203.3718.
- Weingartner, Joseph C and B T Draine (2001). “Dust Grain-Size Distributions and Extinction in the Milky Way, Large Magellanic Cloud, and Small Magellanic Cloud”. In: *The Astrophysical Journal* 548.1, pp. 296–309.
- Werner, M W et al. (2004). “The Spitzer Space Telescope Mission”. In: *The Astrophysical Journal Supplement Series* 154.1, pp. 1–9.
- Wertz, James R (2012). *Spacecraft Attitude Determination and Control*. Ed. by James R Wertz. Vol. 73. Astrophysics and Space Science Library. Dordrecht: Springer Science & Business Media.
- Whitney, B A et al. (2013). “Three-dimensional Radiation Transfer in Young Stellar Objects”. In: *The Astrophysical Journal Supplement* 207.2, p. 30.
- Whitney, Barbara A et al. (2003a). “2-D Radiative Transfer in Protostellar Envelopes: I. Effects of Geometry on Class I Sources”. In: *arXiv.org* 2, pp. 1049–1063. arXiv: astro-ph/0303479v1 [astro-ph].

- Whitney, Barbara A et al. (2003b). “Two-dimensional Radiative Transfer in Protostellar Envelopes. II. An Evolutionary Sequence”. In: *The Astrophysical Journal* 598.2, pp. 1079–1099.
- Wilking, B A et al. (1989). “A millimeter-wave spectral-line and continuum survey of cold IRAS sources”. In: *Astrophysical Journal* 345, pp. 257–264.
- Williams, J P, L Blitz, and C F McKee (2000). “The Structure and Evolution of Molecular Clouds: from Clumps to Cores to the IMF”. In: *Protostars and Planets IV (Book - Tucson: University of Arizona Press; eds Mannings,* pp. 97–.
- Wright, Edward L et al. (2010). “The Wide-field Infrared Survey Explorer (WISE): Mission Description and Initial On-orbit Performance”. In: *The Astronomical Journal* 140.6, pp. 1868–1881.
- Yusef-Zadeh, F, M Morris, and R L White (1984). “Bipolar reflection nebulae - Monte Carlo simulations”. In: *Astrophysical Journal* 278, pp. 186–194.
- Zernike, F (1938). “The concept of degree of coherence and its application to optical problems”. In: *Physica* 5.8, pp. 785–795.
- Zhou, S., N. J. Evans II, and L. G. Mundy (1990). “An NH<sub>3</sub> ring around the infrared sources in NGC 2071”. In: ApJ 355, pp. 159–165. DOI: 10.1086/168749.